Search for K isomers in ^{252,254}No and ^{260}Sg and investigation of their nuclear structure

Barbara Sulignano
Born in Naples, Italy

MAINZ, 2007

Abstract

Study of K isomerism in the transfermium region around the deformed shells at N=152, Z=102, and N=162, Z=108 provides important information on the structure of heavy nuclei. Recent calculations suggest that the K-isomerism can enhance the stability of such nuclei against alpha emission and spontaneous fission. Nuclei showing K isomerism have neutron and proton orbitals with large spin projections on the symmetry axis which is due to multi quasiparticle states with aligned spins K. Quasi-particle states are formed by breaking pairs of nucleons and raising one or two nucleons in orbitals near the Fermi surface above the gap, forming high K (multi)quasi-particle states mainly at low excitation energies. Experimental examples are the recently studied two quasi-particle K isomers in ^{250,256}Fm, ^{254}No, and ^{270}Ds. Nuclei in this region, are produced with cross sections ranging from several nb up to μb, which are high enough for a detailed decay study. In this work, K isomerism in Sg and No isotopes was studied at the velocity filter SHIP of GSI, Darmstadt. The data were obtained by using a new data acquisition system which was developed and installed during this work. ^{252,254}No and ^{260}Sg were produced in fusion evaporation reactions of ^{48}Ca and ^{54}Cr projectiles with ^{206,208}Pb targets at beam energies close to the Coulomb barrier. A new K isomer was discovered in ^{252}No at excitation energy of 1.25 MeV, which decays to the ground state rotational band via gamma emission. It has a half-life of about 100 ms. The population of the isomeric state was about 20% of the ground state population. Detailed investigations were performed on ^{254}No in which two isomeric states (275 ms and 198 μs) were already discovered by R.-D. Herzberg, but due to the higher number of observed gamma decays more detailed information about the decay path of the isomers was obtained in the present work. In ^{260}Sg, we observed no statistically significant component with a half life different from that of the ground state. A comparison between experimental results and theoretical calculations of the single particle energies shows a fair agreement. The structure of the here studied nuclei is

in particular important as single particle levels are involved which are relevant for the next shell closure expected to form the region of the shell stabilized superheavy elements at proton numbers 114, 120, or 126 and neutron number 184. K isomers, in particular, could be an ideal tool for the synthesis and study of these isotopes due to enhanced spontaneous fission life times which could result in higher alpha to spontaneous fission branching ratios and longer half lifes.

Zusammenfassung

Das Studium von K-Isomeren in Transfermiumelementen im Bereich N=152, Z=102 und N=162, Z=108 liefert wichtige Informationen über die Kernstruktur schwerer Elemente. Neuere Rechnungen zeigen, dass K-Isomerie die Stabilität eines Kerns gegenüber α-Emission oder Spontanspaltung erhöhen kann. Voraussetzung für das Auftreten von K-Isomerie ist das Aufbrechen von Nukleonpaaren nahe der Fermifläche und das Anheben eines oder mehrerer Nukleonen auf höhere Energieniveaus, wobei Quasiteilchenzustände gebildet werden. Wenn dabei Neutron- und/oder Protonorbitale mit großen Spinprojektionen K auf die Symmetrieachse des Kerns entstehen, können sich K-Isomere ausbilden. Beispiele für Kerne, in denen K-Isomere beobachtet wurden, sind ^{250,256}Fm, ^{254}No und ^{270}Ds. Die Produktionsquerschnitte für diese Kerne sind nb bis b und damit ausreichend hoch für eine detaillierte Zerfallsspektroskopie. In dieser Arbeit wurde K-Isomerie in No und Sg Isotopen am Geschwindigkeitsfilter SHIP der GSI Darmstadt untersucht. Dafür stand auch ein neues Datenaufnahmesystem zur Verfgung, welches während dieser Arbeit entwickelt und installiert wurde. ^{252,254}No und ^{260}Sg wurden in Fusions-Verdampfungsreaktionen mit ^{48}Ca, ^{54}Cr Strahlen und ^{206,208}Pb Targets bei Energien an der Coulombbarriere erzeugt. In ^{252}No wurde ein neues K-Isomer bei einer Anregungsenergie von 1.25 MeV entdeckt, welches mit einer Halbwertszeit von 100 ms über α-Emission ins Grundzustandsrotationsband zerfällt. Im Isotop ^{254}Fm konnte die Existenz von zwei K-Isomeren mit Halbwertszeiten von 275 ms und 198 s bestätigt werden, die bereits aus Experimenten von R.-D. Herzberg bekannt war. Auf Grund der fünfmal höheren Statistik konnte überdies in der vorliegenden Arbeit das Zerfallsschema von ^{254}No erweitert werden. In ^{260}Sg konnte keine statistisch relevante Komponente identifiziert werden, die dem Zerfall eines Isomers zugeordnet werden könnte. K-Isomerie könnte für die Produktion und Untersuchung superschwerer Kerne eine wichtige Rolle spielen. Auf Grund der erhöhten Lebensdauer fr Spontanspaltung können ein gröeres Verzweigungsverhältnis von α-Emission zu

Spaltung und längere Halbwertszeiten erwartet werden. Für die Protonenzahlen 114, 120 oder 126 und die Neutronenzahl 184 wird ein Bereich schalenstabilisierter Kerne erwartet. Einteilchenzustnde, welche für diese Schalenabschlüsse relevant sind, sind auch in den Isotopen beteiligt, die in dieser Arbeit untersucht wurden.

Contents

Introduction

Detailed investigation of the decay of deformed nuclei in the transfermium region around N=152, Z=102 and N=162, Z=108, where enhanced stability is observed, is an important source for information on the structure of heavy nuclei.

Nuclei in this region are produced with cross-sections ranging from several nb to some μb, high enough for a detailed decay study, allowing an interesting benchmark for theoretical predictions. Moreover, recent calculations [1] suggest that high spin isomerism can enhance the stability of such nuclei against α-decay and spontaneous fission. The reason is the presence of deformed shell gaps at Z=102 and 108 and pronounced deformed shells at N= 152 and 162. Below and above these gaps there is a region of very high single particle level density with high angular momentum. Quasi particle states are formed by breaking pairs of nucleons and raising one or two quasi particles, in orbitals near the Fermi surface, above the gap forming high K multi-quasiparticle states at low excitation energies. Due to the high degree of 'K forbiddenness' (the selection rule for an electromagnetic transition requires that the multipolarity of the decay radiation l is at least as large as the change in the K-value: $l > \Delta$K), internal transitions into states of low K values are strongly hindered. Therefore, decays from high K states to low lying K states can have half-lives in the range from ns up to years. Moreover, a parity opposite to that of the ground state can further reduce the transition rate from an excited state to the ground state or to a member of the ground state band. Such excited high K states are referred to as "K-isomers". Experimentally, the first K isomers close to N=152 and Z=102 were discovered 33 years ago by Ghiorso et al. [2] in ^{250}Fm and ^{254}No, with half-lives of 1.8 s and 0.28 s, respectively. The decay of ^{254}No was recently investigated by R.-D. Herzberg et al. [3] through gamma measurements at the RITU separator at the accelerator laboratory of the University of Jyväskylä, where also a second isomer with a half-life of 184 μs was found. The first K isomer in the region N=162, Z=108 was found in the isotope ^{270}Ds in 2000 at the velocity filter SHIP.

In the frame of this thesis, a new K isomer was discovered in ^{252}No and the isomeric states in ^{254}No were reinvestigated with higher statistics. Further, search experiments for K isomerism in ^{260}Sg and its daughter nucleus ^{256}Rf were performed.

This thesis work is divided in four parts.

The summery of nuclear models is made in the second chapter. It provides the physical background for the interpretation of experimental results described in the later chapters.

Detailed information about the technique used and the method of analysis applied to produce and study the transfermium elements are given in the third part.

In chapter 4 and 5 experimental results and theoretical interpretations of the investigated nuclei is presented.

At the end a balance of the knowledge on spectroscopic properties (isomeric states, nuclear levels, etc.) of elements in the transfermium region known up to now is supplied.

Chapter 1

Physical Background

1.1 Nuclear structure

1.1.1 Liquid drop and shell model

The oldest model used to predict the shape and energy of the atomic nucleus is the liquid drop model (LDM). Alternative to the picture of a nucleus composed of individual protons and neutrons, the LDM treats the nucleus as a quantum fluid with low compressibility. The equilibrium state resembles a sphere. Changes in the energy of the nucleus deform the spherical shape. Deformations result in the extension and/or compression of one or more axes while the volume is considered to be constant. This model is unable to explain a number of nuclear phenomena, among others the existence of magic numbers. To overcome this problem the nuclear shell model was developed.

The first step was to "borrow" the model of the atomic theory. In the atomic shell model, the shells are filled with electrons in order of increasing energy respecting the Pauli principle. The result is an inert core of filled shells and some number of valence electrons. Finally the atomic properties are then determined by these valence electrons. In analogy, the nuclear shell model was developed in the late 1940s. It is based on the idea to consider the motion of the unpaired nucleons in a mean central potential V(r) generated by the other nucleons in the nucleus. But it was only in 1949 that Maria Goeppert-Mayer [4], following a suggestion of Fermi, added a spin-orbit term $(\vec{l} \cdot \vec{s})$ to the Woods-Saxon potential

$$V = V(r) + V_{ls}(r)(\vec{l} \cdot \vec{s}) \tag{1.1}$$

This enabled them to explain the existence of magic numbers and other nuclear phenomena. In contrast to the spin-orbit coupling in the electron shell which is of electromagnetic nature and hence weak, the spin-orbit in the nucleus is large. The effect of strong spin-orbit coupling is to depress certain high-spin levels from one shell to a lower shell and hence to give different occupation numbers for the closed shells. The spin-orbit splitting coupling in the nucleus is an inherent part of the strong interaction, i.e. is strong.
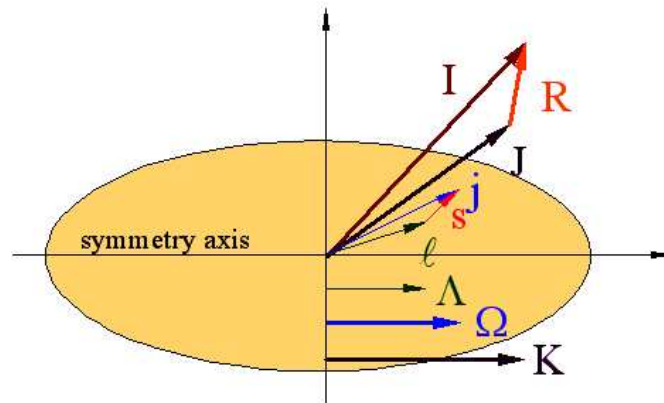
1.1.2 Nilsson model

Figure 1.1: Diagram of a nucleus with prolate quadrupole distortion and a single nucleon orbiting in an equatorial plane. $j = l + s$ is the total angular momentum of the unpaired nucleon, Λ is the projection of the angular momentum l on the symmetry axis, Ω is the projection of j on the symmetry axis, and K is the projection of total intrinsic angular momentum I onto the symmetry axis. $\vec{R}$ is the collective rotational angular momentum.

The original shell model used a spherical potential. It was, thus, not able to describe nuclei with permanent deformation. In 1955 S.G. Nilsson introduced a modified shell model describing ellipsoidally deformed nuclei. Nilsson used a deformed harmonic oscillator potential, V_{osc} [5], in order to reproduce the correct shell structure. He put $V_{ls}=$ const$=$ C. In order to approximate the oscillator potential to the Woods-Saxon potential he added a correction term Dl^2. The resulting potential is

$$V = \frac{1}{2}M(\omega_\perp^2 (x^2 + y^2) + \omega_\parallel^2 z^2) - C\vec{l}\cdot\vec{s} - Dl^2 \qquad (1.2)$$

where z is the symmetry axis. $\omega_\perp$ and $\omega_\parallel$ differ only in the case that the potential is deformed. Introducing the deformation parameter ϵ we can define:

$$\omega_\perp = \omega_0(1 + \frac{1}{3}\epsilon) \tag{1.3}$$

and

$$\omega_\parallel = \omega_0(1 - \frac{2}{3}\epsilon) \tag{1.4}$$

In the case of positive deformation, $\omega_\perp$ is larger then $\omega_\parallel$; the nucleus is long and narrow in a prolate shape. On the contrary, for negative deformation, the nucleus is flat or oblate.

Using this anisotropic three dimensional harmonic oscillator potential, Nilsson found out that each single particle state in these nuclei is splitting.

For non spherical nuclei the total angular momentum of the single particle state, $j = l + s$, is not a good quantum number but its projection Ω on the symmetry axis z, is (see Fig. 1.1).

Each single particle state in the deformed nucleus is characterized by the asymptotic quantum numbers $\Omega^\pi[N, n_z, \Lambda]$:

- N is the principal oscillator quantum number

- $\pi = (-1)^N$ is the parity of the state

- n_z is the oscillator quantum number along the nuclear symmetry axis

- Λ and Σ are the projections of the orbital angular momentum l and the spin s, respectively, on the symmetry axis. $\Omega = \Lambda \pm \Sigma = \Lambda \pm 1/2$.

The energy of the single particle states Ω^π as function of the quadrupole deformation $\beta_2 = 1.06 * \epsilon$ of the nucleus is represented in the Nilsson diagram, see Fig. 1.2 a). For each orbit with angular momentum j, there are 2j+1 values of Ω. Low Ω states favor prolate shapes while high Ω states favor oblate shapes. Each $\pm\Omega$ state is two-fold degenerate. As an example, Fig. 1.2 b shows the Nilsson diagram for protons or neutrons, Z or N > 126.
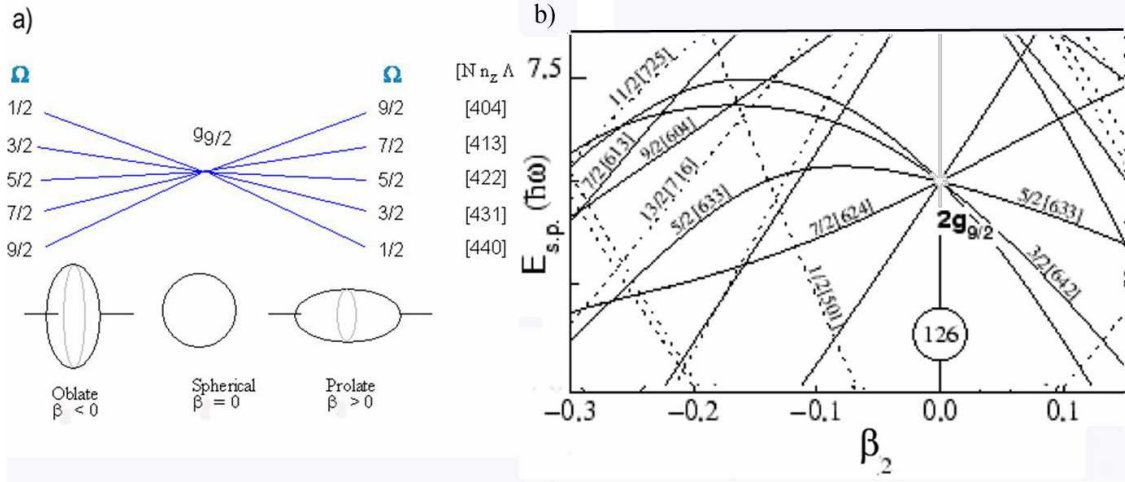
Figure 1.2: Splitting of energy levels for different Ω values with deformation. Low Ω states favor prolate shapes while high Ω states favor oblate shapes. The state $g_{9/2}$ is 10-fold degenerate in a spherical potential because all 2j+1 projections of the angular momentum lie at the same energy. This state splits into 5 doubly degenerate states $\Omega = \pm 1/2, \pm 3/2, \pm 5/2, \pm 7/2, \pm 9/2$ in a spheroidal nucleus (because the states Ω and $-\Omega$ are degenerate). b) Single particle energy levels as a function of deformation (β_2 parameter).

1.1.3   Strutinsky model

The Nilsson model, although being able to reproduce several properties of the nucleus, failed to predict the existence of stable deformation in the nuclear ground state and other properties such as the second minimum in the fission barrier of actinide nuclei. To overcame this, Strutinsky [6] applied, the concept of both the liquid-drop model and the shell model, to accurately reproduce observed experimental nuclear ground state energies. The basis of the method is that the total energy is split into two terms; the first is a smoothly varying energy derived from the liquid drop model, and the second a rapidly varying part that is calculated from the fluctuations in the shell model energy,

$$E_{tot} = E_{ldm} + E_{shell}(protons) + E_{shell}(neutrons) \tag{1.5}$$

The shell energy, E_{shell}, can be defined as the difference between the actual discrete level density, g, and a "smeared" level density $\tilde{g}$ defined as followed :

$$g(e) = \sum \delta(e - e_i) \tag{1.6}$$

and

$$\tilde{g}(e) = \frac{1}{\gamma\sqrt{\pi}} \sum f_{corr}\left(\frac{e - e_i}{\gamma}\right) exp\left(\left(-\frac{(e - e_i)^2}{\gamma^2}\right)\right) \tag{1.7}$$

Where γ is an energy of the order of the shell spacing $\hbar\omega_0$, and f_{corr} is a correction function which keeps the long-range variation over energies much larger than $\hbar\omega_0$ unchanged. The shell energy can be calculated using

$$E_{shell} = 2\sum e_i - 2\int e\tilde{g}(e)de \tag{1.8}$$

the factor 2 arises to take in consideration the double degeneracy of the deformed levels.

1.1.4 Collective states

Since the transfermium nuclei do not have spherical shape, they exhibit also a rotational levels in addition to the single particle states. Furthermore an addition of energy can cause them, as it is also known for spherical nuclei, to oscillate about their equilibrium states.

1.1.5 Rotational states

A nucleus rotating about an axis has a collective angular momentum R in addition to the single particle angular momentum j. Its total angular momentum is then $I = j + R$ (Fig. 1.1).
For even even nuclei in their ground state, the nucleons are paired and $j = 0, \Omega = 0$. The energy levels of the ground state rotational band have the form

$$E_I = \frac{\hbar^2}{2\Im}I(I + 1) \tag{1.9}$$

$\Im$ is the moment of inertia and I has the values $0, 2, 4, 6, 8....$
An example of a rotational spectrum in the case of a perfect rotor for an even even nucleus is shown in Fig. 1.3 for ^{252}No.
For odd A nuclei or in excited states of even even nuclei with $\Omega \neq 0$, the energies of the levels are

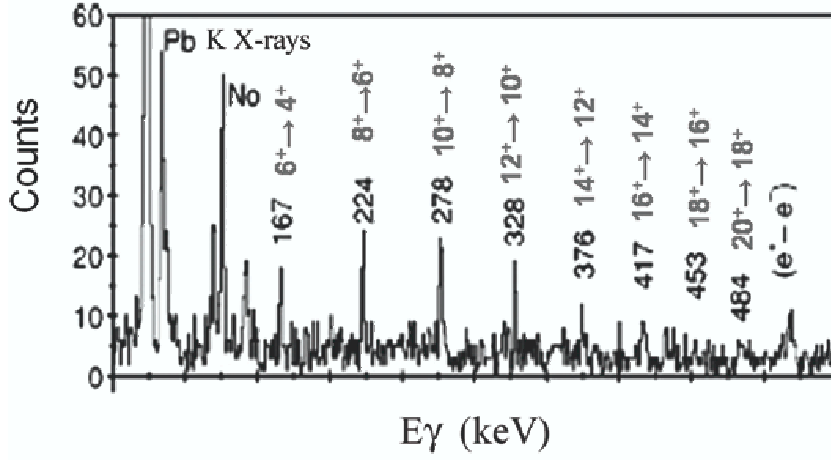$$E_{I,K} = \frac{\hbar^2}{2\Im}[I(I + 1) - K^2] \tag{1.10}$$

Figure 1.3: Structure of a rotational band in the case of the even even nucleus ^{252}No [7].

K is the projection of the total angular momentum I onto the symmetry axis. The base of each rotational band has

$$I_0 = K = \Omega \tag{1.11}$$

and the rotational sequence is

$$I = I_0, I_0 + 1, I_0 + 2, ... \tag{1.12}$$

$\hbar^2/2\Im$ is ~7 keV for even even nuclei, 6 keV for odd A nuclei and 5.7 keV for odd nuclei.

We should emphasize that the nuclear moment of inertia is not identical to the moment of inertia of a rigid body. The explanation is found in the conception of the nucleus as a rigid core plus a collectively rotating fluid of valence nucleons.

1.1.6   Vibrational levels

The vibrations of a nucleus are caused by periodic deformations of the nuclear surface. In the case of harmonic oscillations, the energy eigenvalues of the vibrational states are

$$E_n = E_0 + n\hbar\omega \tag{1.13}$$

where ω is the eigen frequency of the oscillator, n is 0,1,2,... and E_0 is the zero point energy of the oscillations.
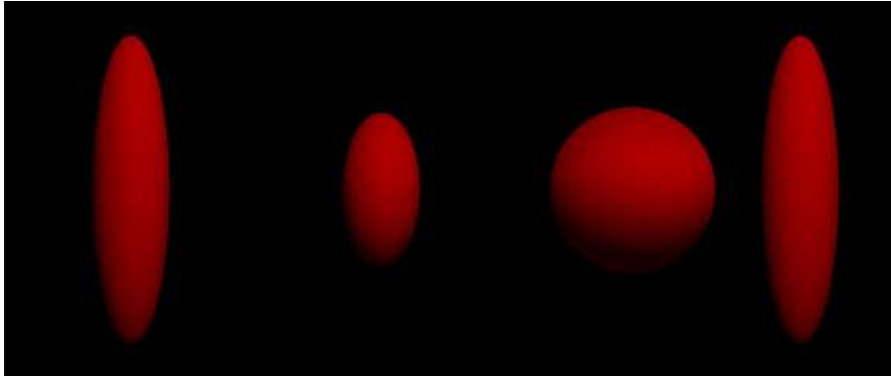
Figure 1.4: Beta vibrations are quadrupole vibrations with radially symmetric deformations. The nucleus has a constant volume that oscillates between axial and transverse positions. [8]
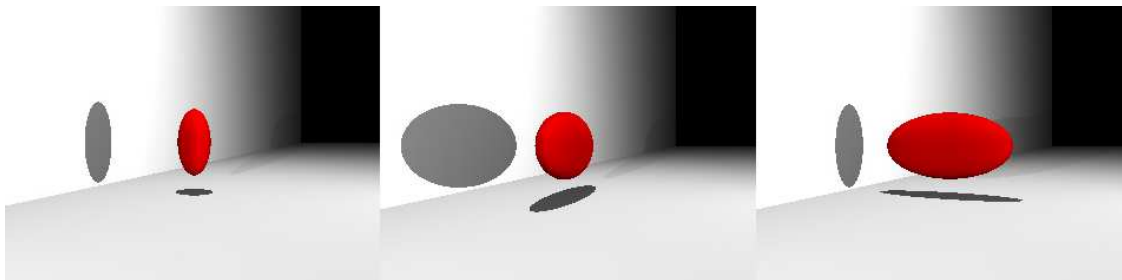
Figure 1.5: Gamma vibrations are quadrupole vibrations without radial symmetry. The nucleus is symmetric in the x-, y- and z-planes, but the lateral cross-sections of the nucleus are ellipses. This is shown by the shadows. The nucleus is triaxial. [8]

The vibrational motions of nuclei are essentially quadrupole and octupole. The two types of quadrupole vibrations in the nucleus are β and γ vibrations.

In the case of β vibrations, the length of the major axis expands and contracts periodically with the cigar-shaped nucleus becoming thinner or fatter, see Fig. 1.4. The energy of the phonon excitation is typically 1 MeV and the frequency is $10^{20}/s$. The life time of such an excited state is about $10^{-12}s$ [9].

Gamma vibrations are deformations without radial symmetry. Both, the volume and the height of the nucleus remain constant. The nucleus is symmetric in the x-,y-,z-planes, but the lateral cross sections of the nucleus are ellipses, see Fig. 1.5.

The octupole vibrations are multipole vibrations, see Fig. 1.6, which lead to an

Figure 1.6: An example of multipole vibrations are octupole vibrations. [8]

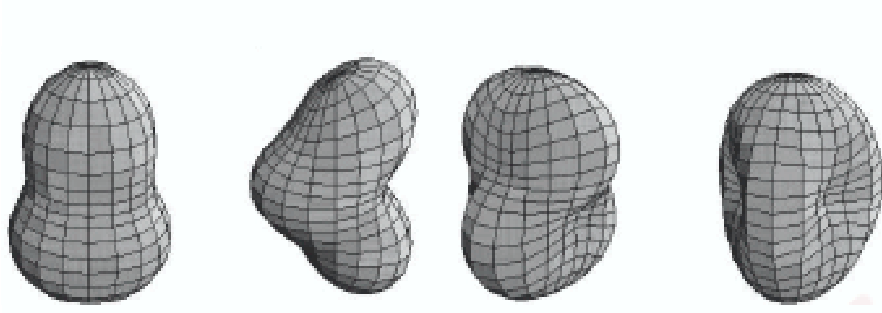exotic nuclear pear shape. The quantum numbers (K,I, π) are (1,1,-). The allowed values of I are 1^-, 3^-, 5^-...

Rotational bands can be built on each vibrational state. The energy levels (in the Rotational Vibrational Model) of rotational bands built on a β or γ vibration are

$$E = E_0 + \frac{\hbar^2}{2\Im}I(I+1) \tag{1.14}$$

E_0 is the energy of the base level. For β bands the allowed values for I are 0,2,4...for an even even nucleus. The quantum numbers (K,I,π) are (0,0,+). The constant $\frac{\hbar^2}{2\Im}$ has the same value as the base of the ground state rotational band. These states decay to the ground state by pure electric monopole radiationless internal conversion at a rate comparable to the decay by E_2 radiation to the first excited state.

In the case of γ vibrations the quantum numbers (K,I,π) are (2,2,+) for the base state. The allowed values of I are 2,3,4. This 2^+ state decays by E_2 radiation to the $0^+, 2^+$ or 4^+ states of the ground state band.

An empirical method to distinguish if a nucleus is a vibrator or rotor is given by the ratio of 4^+ and 2^+ energy levels. In the vibrational case, this ratio is equal to 2.0 ($E \propto n$) while in the rotational case it is equal to 3.33 ($E \propto I(I+1)$).

1.1.7 Pairing effects

Another important property is the pairing force. This force drives two identical nucleons to form a pair with total angular momentum zero.

The paring force is moreover responsible to modify the occupation probabilities of the nucleon orbitals and changes the level spacing relative to those of the single particle model which does not consider pairing.

In even-even nuclei, the lowest single particle excited state corresponds to breaking a nucleon pair and moving a nucleon to a higher state and thus leaving a *hole* in the original state. These pairs are named *quasi-particle*. Their energy above the ground state according to the BCS theory [10] is:

$$\epsilon_k' = [(\epsilon_k - \lambda)^2 + \Delta^2]^{1/2} \tag{1.15}$$

where ϵ_k is the energy of the single particle state, ϵ_k' is the quasi-particle energy, λ is the Fermi energy and Δ is the gap parameter proportional to the strength of the pairing interaction. For an even even nucleus, the excitation energy of the first intrinsic state above the ground state is 2Δ as one goes from one quasiparticles to two quasiparticles. Odd even nuclei in their ground state, contain already one quasiparticle with the energy Δ.

1.2 Alpha decay

All isotopes of elements beyond bismuth are unstable to α particle emission, to β-decay or spontaneous fission (SF).

The spontaneous emission of an α particle can be represented by the following relation:

$$X_N \rightarrow {}^{A-4}_{Z-2}X'_{N-2} + \alpha \tag{1.16}$$

Alpha decays rates are extremely sensitive to the atomic number of the emitting nucleus ("Coulomb barrier"), the Q-value (or energy release) of the process, the change of angular momentum (Δl), and parity changes ($\Delta \pi$). For a given nucleus, the daughter state predominantly populated, is essentially determined by the "balance" between Δl, $\Delta \pi$ and Q. Since ground state spin and parity are 0^+ in even-even nuclei, in these nuclei ground state to ground state transitions dominate. In odd mass nuclei or odd-odd nuclei the situation is more complicated, since hindrance

due to (large) Δl or change in parity may cancel the advantage of a favorable Q value. Thus, in these nuclei often excited states in daughter nuclei, which may be located several hundred keV above the ground state, are populated predominantly.

From the conservation of energy, the final total energy in the α decay process is

$$m_X c^2 = m_{X'} c^2 + E_{X'} + m_\alpha c^2 + E_\alpha \tag{1.17}$$

m_X, $m_{X'}$, m_α are the masses of the daughter nucleus, mother nucleus, and the α particle. $E_{X'}$ and E_α are the kinetic energies of the daughter nucleus and the α particle. This formula can be written also as

$$Q = (m_X - m_{X'} - m_\alpha)c^2 = E_{X'} + E_\alpha \tag{1.18}$$

The Q value is the net energy released in the decay.

Following the conservation of linear momentum, the Q value is shared between the α particle and the recoil energy of the daughter nucleus due to $p_\alpha = p_{X'} \Rightarrow (m_X - m_\alpha)v_{X'} = m_\alpha v_\alpha$.

Finally, we can write the kinetic energy of the alpha particle as function of the Q value:

$$E_\alpha = \frac{Q}{1 + m_\alpha/m_{X'}} \tag{1.19}$$

In the frame of the quantum mechanical theory, the α particle is assumed to be preformed inside the mother nucleus and to move in a volume determined by the daughter nucleus. The particle inside the potential has a non zero probability to pass the barrier by tunnelling. The closer the energy of the particle is to the top of the barrier, the more likely the particle will go out. Also, the more energetic the particle is, the more frequently the particle will attack the barrier and the more likely it will escape. This probability λ for α decay is :

$$log(\lambda) = A + \frac{B}{\sqrt{T_\alpha}} \tag{1.20}$$

where A is constant and B is Z dependent. The relation between the half-life and the decay probability is $\lambda = ln2/T_{1/2}$. This formula is known as the Geiger-Nuttall law of the α decay [64].

The hindrance factor for an α transition is defined as the ratio

Δ l	1	2	3	4
Name	Dipole	Quadrupole	Octupole	Hexadecapole
No parity change	M1	E2	M3	E4
Parity change	E1	M2	E3	M4
Selection Rule Δj	$0,\pm1$	$0,\pm1,\pm2$	$0,\pm1,\pm2,\pm3$	$0,\pm1,\pm2,\pm3,\pm4$

Table 1.1: Selection rules for electromagnetic transition for the lowest multipoles.

$$HF = \frac{T_\alpha^{exp}}{T_\alpha^{theo}} = \frac{T_{1/2}/(b_\alpha \times i_\alpha)}{T_\alpha^{theo}} \tag{1.21}$$

where $T_{1/2}$ and b_α are the half-life and the α-branching ratio of the isotope of interest and i_α is the intensity of the transition relative to all α transitions. Theoretical half-lives T_α^{theo} may be calculated either the formalism proposed by Rasmussen et al. [12] or, as done here, using the semi-empirical formula proposed by Poenaru et al. [13] with the parameter modification proposed by Rurarz et al. [14].

An α decay can occur only if the total angular momentum and parity are conserved. The *selection rules* [43] are:

$$|j_i - j_f| \leq l \leq j_i + j_f \tag{1.22}$$

where j_i and j_f are the total angular momenta of the initial and final state and l is the orbital angular momentum of the emitted alpha. Only even values of l are allowed if the parity of the initial and final nuclear states is the same and only odd values of l are allowed if there is a parity change.

1.3 Electromagnetic transition rates

Internal transitions may proceed by the emission of a photon (γ ray) or internal conversion (transfer of the energy to an orbital electron). The transition occurs following the selection rules listed in tab.1.1.

If the sum $j_i + j_f + l$ is an odd number, the transition is called a *magnetic* 2^l pole transition otherwise it is referred to as an *electric* 2^l pole transition. The electric field is due to oscillating charges, while magnetic fields are due to oscillating currents.

The probability λ of a gamma ray emission between two single particle states has been calculated by Weisskopf:

$$\lambda_{electric} = 10^{21} \frac{4.4(l+1)}{l[(2l+1)!!]^2} (\frac{3}{l+3})^2 (\frac{E_\gamma}{197})^{2l+1} R^{2l} s^{-1} \tag{1.23}$$

$$\lambda_{magnetic} = 10^{21} \frac{1.9(l+1)}{l[(2l+1)!!]^2} (\frac{3}{l+3})^2 (\frac{E_\gamma}{197})^{2l+1} R^{2l-2} s^{-1} \tag{1.24}$$

l is the angular momentum carried away by the photon, E_γ is the transition energy and R is the nuclear radius in fm.

From the Weisskopf equation one can deduce for a transition involving a given l and E_γ that the ratio of the lifetimes for magnetic and electric transitions are $t_{mag}/t_{elec} = 2.3R^2$. This means that an electric transition is faster then a magnetic transition of the same multipolarity. From the Weisskopf estimation one further can deduce that γ ray transitions are hindered by large spin change and low energies. It should be noted that the Weisskopf estimate hold strictly only for single particle transitions and not for collective transitions. Collective transitions, e.g. stretched E2 transitions along the Yrast line can be 100 times faster.

1.4   Internal conversion

The internal conversion is a competing process to γ ray emission. The electromagnetic field of the nucleus transfers energy to the atomic electron and if it is greater then the electron binding energy B it is ejected from the atom.

The kinetic energy of the emitted electron is

$$E(e^-) = E_i - E_f - B \tag{1.25}$$

Electron transitions into holes in the $1s_{1/2}$ atomic orbit produce the K lines, electrons in the $2s_{1/2}$, $2p_{1/2}$, and $2p_{3/2}$ atomic orbits produce the L lines (L_I, L_{II}, L_{III}), electrons in the 3s, p, and d states produce the M lines.

The total decay probability for a nuclear transition is given by

$$\lambda = \lambda_\gamma + \lambda_e = \lambda_\gamma[1 + \alpha] \tag{1.26}$$

where α is the total internal conversion coefficient

$$\alpha = \frac{\lambda_e}{\lambda_\gamma} \tag{1.27}$$

It represents the ratio of the emitted conversion electrons and the number of emitted γ rays and it is the sum of the partial coefficients of the individual atomic shells

$$\alpha = \alpha_K + \alpha_L + \alpha_M... \tag{1.28}$$

Conversion coefficient ratios such as α_K/α_L, α_{LI}/α_{LII}, or $\alpha_{LII}/\alpha_{LIII}$ are sensitive to the type of transition, e.g., E1, M1, E2, or M2.

1.5 Isomers

Nuclei in metastable states are called isomers. Excitation energies of isomeric states may reach up to several MeV. There is no strict definition for a minimum half life of an isomer.The isomeric states, are states with strongly inhibited electromagnetic decay modes. They occur when there is a secondary energy minimum for some values of shape elongation, spin or spin projection on the symmetry axis. These lead to the three main configurations schematically presented in Fig. 1.7.

Shape isomers occur when there is a second energy minimum at a larger elongation of the nucleus (the first minimum corresponds to the ground state, see the Fig. 1.7). Shape isomers can decay by γ ray emission or by fission if the fission barrier is low enough (fission isomers).
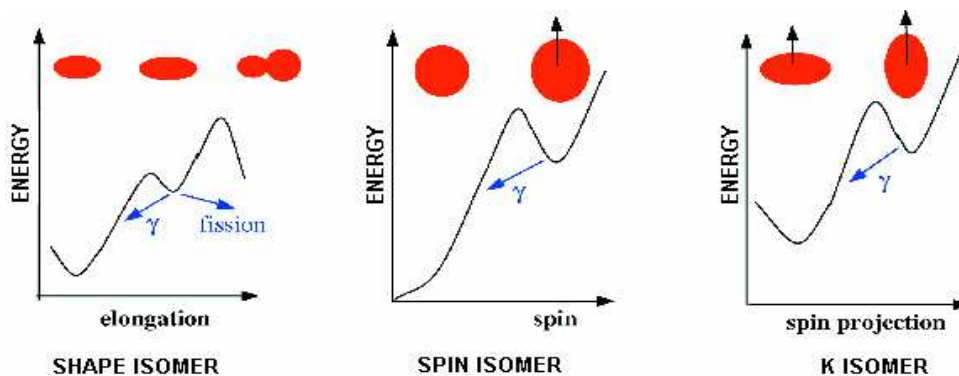

Figure 1.7: Schematic representation of different isomeric configurations.

Spin isomers or *Spin traps* occur when the decay to a lower energy state requires a large change in spin and therefore the emission of radiation with high multipolarity is required. The relatively low probability of these transitions (see formula 1.23,1.24) leads to the longer lifetimes and produces, hence, these isomeric states (see Fig. 1.7).

K-traps are a kind of spin trap. Their existence depends not only on the change of the magnitude of the nuclear spin vector, but also on its orientation, see Fig. 1.7. The quantum number K represents the projection of the total angular momentum onto the symmetry axis of the deformed nucleus. The selection rules require that the multipolarity of the decay radiation is $l > \Delta K$. However, these K forbidden transitions are rather hindered than forbidden [16].

The probability of the decay is expressed by

$$\nu = \Delta K - l$$

This represents the degree of forbiddenness of a given transition. Empirically, each degree of K-forbiddenness increases the lifetime of the state by a factor of 20. This is expressed as the hindrance per degree of K-forbiddenness (or the reduced hindrance) defined as,

$$f_\nu = \frac{T_{1/2}^\gamma}{T_{1/2}^W} = F_w^{1/\nu} \tag{1.29}$$

where $T_{1/2}^\gamma$ is the partial γ-ray half-life and $T_{1/2}^W$ is the Weisskopf single-particle estimate. This allows transitions of different energies and K-forbiddenness to be compared. For low-lying high-K states, ΔK can easily be as high as 8, as in the classical example of the $K^\pi = 16^+$ isomer in ^{178}Hf, which decays to a $K^\pi = 9^-$ ($|\Delta K|$=7) band and has a half-life of 31 years [65].

1.6   G factor

One experimental distinction between proton and neutron single particle states comes from the measurement of the magnetic dipole moment μ_N. It is generated by the orbital motion of the protons and by the intrinsic spins of the nucleons plus a component due to the interaction with other nucleons. In the single particle model, the magnetic moment has a contribution from the collective motion of the protons in the core plus the contribution from a valence or excited nucleon of angular momentum j. The core contribution to the magnetic moment is estimated assuming

the protons evenly distributed throughout the nucleus, which rotates with the core angular momentum R.

$$\mu = g_R R \mu_N \tag{1.30}$$

g_R is the rotational g-factor describing the collective rotation; it is approximately equal to Z/A. This expression applies to even even nuclei with no intrinsic excitation (K=0). For $K \neq 0$, the magnetic dipole moment can be described by the factor g_K. The total angular momentum I=R+j and the total magnetic dipole moment is:

$$\mu = [g_R I + [g_K - g_R] \frac{K^2}{I+1}] \mu_N \tag{1.31}$$

For example the reduced matrix element of the magnetic dipole moment operator results for the reduced M1 transition:

$$B(M1; I \rightarrow I - 1) = \frac{3}{4\pi} [g_K - g_R]^2 \mu_N^2 K^2 |\langle IK10|I-1K\rangle|^2 \tag{1.32}$$

While the reduced matrix element of the electric quadrupole operator gives the expression

$$B(E2; I \rightarrow I - 2) = \frac{5}{16\pi} Q_0^2 |\langle IK20|I-2K\rangle|^2 (eb)^2 \tag{1.33}$$

Q_0 is the intrinsic quadrupole moment. It provides a measure of the charge distribution of the nucleus. For nuclei, having spherically symmetric charge distributions, Q_0 is zero, negative for oblate nuclei and positive for prolate nuclei.

In deformed nuclei, three deformation parameters often are used: $\delta = \Delta R/R$, where $\Delta R = b - a$ (the half axes of the ellipsoid), ϵ defines a rotational ellipsoid, β defines a rotational quadrupoloid

$$Q_0 = \sqrt{16\pi/5} Z e R_0^2 \beta^2 \tag{1.34}$$

These expression can be combined and the values substituted for the Clebsch-Gordon coefficient:

$$\frac{B(M1; I \rightarrow I - 1)}{B(E2; I \rightarrow I - 2)} = \frac{8}{5} \frac{[g_K - g_R]^2 K^2}{Q_0^2} \frac{(2I-1)(I-1)}{(I-1+K)(I-1-K)} \tag{1.35}$$

in units of $[\mu_N^2/e^2 b^2]$ where the g_K factor is related to the 2-quasiparticle configuration.

Chapter 2

Experimental Set Up

2.1 Ion source, accelerator and beams

The most successful method for the synthesis of transfermium elements is fusion evaporation reactions in combination with efficient recoil separation techniques and identification of nuclei by mother-daughter correlations. To exploit it, stable and intense beams are needed.
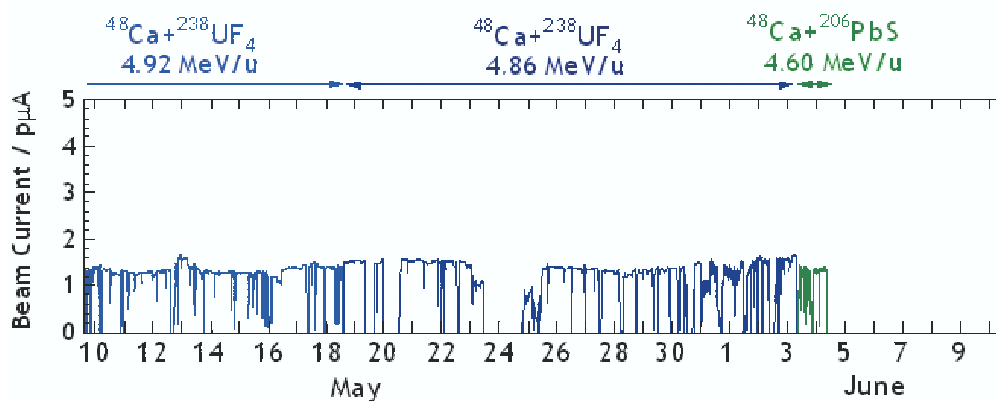

Figure 2.1: Example of beam stability at high average current during irradiation of $^{238}UF_4$ and ^{206}PbS with ^{48}Ca within one month measurement in 2005.

At GSI the beam is delivered by the 120 m long Universal Linear Accelerator (UNILAC). The high charge state injector HLI of UNILAC includes a 14 GHz ECR (Electron Cyclotron Resonance) [17] ion source. The consumption of material in the ECR source is very low. For instance, in the case of ^{48}Ca, which was used to synthesize some of the nuclei studied in this work it was 0.6 mg/h.

19

The ions from the ECR source are injected in a 55 m long Alvarez accelerator (operation frequency 108 MHz) which delivers specific energies (3.6, 4.7, 5.9, 7.1, 8.5, 9.6, 10.5 and 11.4 A MeV). For a fine tuning of the energies and to accelerate particles to energies $E > 11.4$ A MeV, 15 single gap resonators are used. The facility is able to deliver beams of any kind of ions up to Uranium.

The time structure of the beam is determined by a 5 ms wide pulse followed by a 15 ms wide beam pause (25 % duty cycle). In our experiments, the beam intensity for ^{54}Cr or ^{48}Ca was typically ~ 1 pμA on target (1 pμA is $6.24 * 10^{12}$ particle/s). An example for the stability of the beam current is shown in Fig. 2.1.

2.2 Targets

Fixed targets cannot stand the high beam currents used in the synthesis of super-heavy elements. Therefore, a rotating wheel is employed. Eight foils each of 112x24 mm^2 are mounted on a wheel of 310 mm diameter that rotates synchronously to the beam macrostructure at 1125 rpm, see Fig. 2.2 left.

In our experiments for the production of No and Sg, targets of PbS were used. This material has a high melting point (1118 ^{0}C) and good resistivity during the irradiation.

The targets are produced by evaporation of a PbS layer of typically 450 μg/cm^2 (where 410 μg/cm^2 are the Pb content) onto a 40μg/cm^2 heated carbon backing. Finally, a thin carbon layer of 10 μg/cm^2 is evaporated onto the Pb. Details about the target preparation are given by Lommel et al. [18].

The temperature of the targets is monitored by an infrared camera converting the temperature profile of the target to a color picture of isothermal areas (see Fig. 2.2 right).

The target thickness is controlled on line by registration of elastically scattered projectiles and scattering of 20 keV electrons [19].

To improve radiative cooling, the wheel is placed in the middle between two blackened metal plates which are about 4 cm apart and are cooled to ≈ 245 K.

Moreover, a thin carbon foil is mounted downstream behind the targets. The decay of short lived isomers may change the charge state of the ions after leaving the target by conversion and/or Auger electron emission. The carbon foil is therefore used to "equilibrate" the charge state after such processes. It is suited to equilibrate charge states for lifetimes ≤ 10ns.
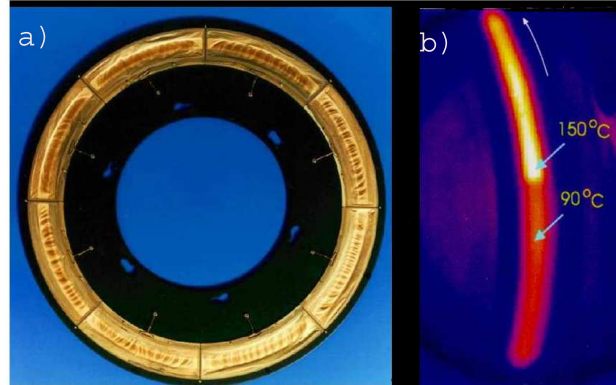
Figure 2.2: a) Rotational target used at SHIP. b) Temperature distribution across the target during the irradiation of the beam - infrared picture.

The charge state of the ion passing through a foil can be estimated by an empirical formula of [20]. The formula for the average equilibrium charge state $\bar{q}$ of an ion after passing a foil is estimated on the base of several experiments:

$$\frac{\bar{q}}{Z_1} = [1 - e^{(-1.25+0.32X^2-0.11X^3)}][1 - 0.0019(Z_2 - 6)\sqrt{X} + 10^{-5}(Z_2 - 6)^2 X] \quad (2.1)$$

where Z_1 and Z_2 are the ion and foil atomic numbers and X is the reduced ion velocity defined as

$$X = v/[3.6x10^8(cm/s)Z_1^{0.45}] \quad (2.2)$$

This formula is valid for $Z_1 \geq 8$ and $4 \leq Z_2 \leq 79$ and $E < 6{\times}A$ MeV with an accuracy of $\Delta\bar{q}/Z_1 < 0.04$. In our case, using carbon foils ($Z_2{=}6$), the formula is reduced to:

$$\bar{q}/Z_1 = [1 - exp(-1.25 + 0.32X^2 - 0.11X^3)] \quad (2.3)$$

2.3 Separator

To have a rapid and efficient separation of the evaporation residues (ER) from the primary beam, the recoil separator technique is used.

The velocity filter is able to separate evaporation residues (ER) from the projectiles on the basis of their velocity differences. From the conservation of momentum in nuclear fusion reactions we obtain:

$$p_p = p_{CN} \tag{2.4}$$

where p_p and p_{CN} are the momenta of projectile and compound nucleus.

$$m_p v_p = (m_p + m_t)v_{CN} \tag{2.5}$$

$$v_{CN} = \frac{m_p}{m_p + m_t}v_p \quad and \quad E_{CN} = \frac{m_p}{m_p + m_t}E_p \tag{2.6}$$

where

$$v_{CN} < v_p \quad and \quad E_{CN} < E_p \tag{2.7}$$

In principle the ER could be separated from the primary beam by a simple deflection magnet according to :

$$qvB = mv^2/\rho \quad for \quad \vec{v} \perp \vec{B} \tag{2.8}$$

However, the electric charges of the ER and the projectiles have a broad distribution after leaving the target. Therefore to have an effective collection of the ER a combined electric and magnetic field is used.

Since the forces acting on an ion in an electric or magnetic field are given by

$$F_{el} = qE \ where \quad \vec{v} \perp \vec{E} \quad and \quad F_{mag} = qvB \ where \ \vec{v} \perp \vec{B} \tag{2.9}$$

we obtain in a combined field

$$F_{tot} = F_{el} + F_{mag} \tag{2.10}$$

and thus

$$F_{tot} = q(E + vB) \tag{2.11}$$

if the relation $E = -v_0 B$ is fulfilled we obtain independent of q:

$$F_{tot} = 0 \quad for \quad v = v_0 \tag{2.12}$$

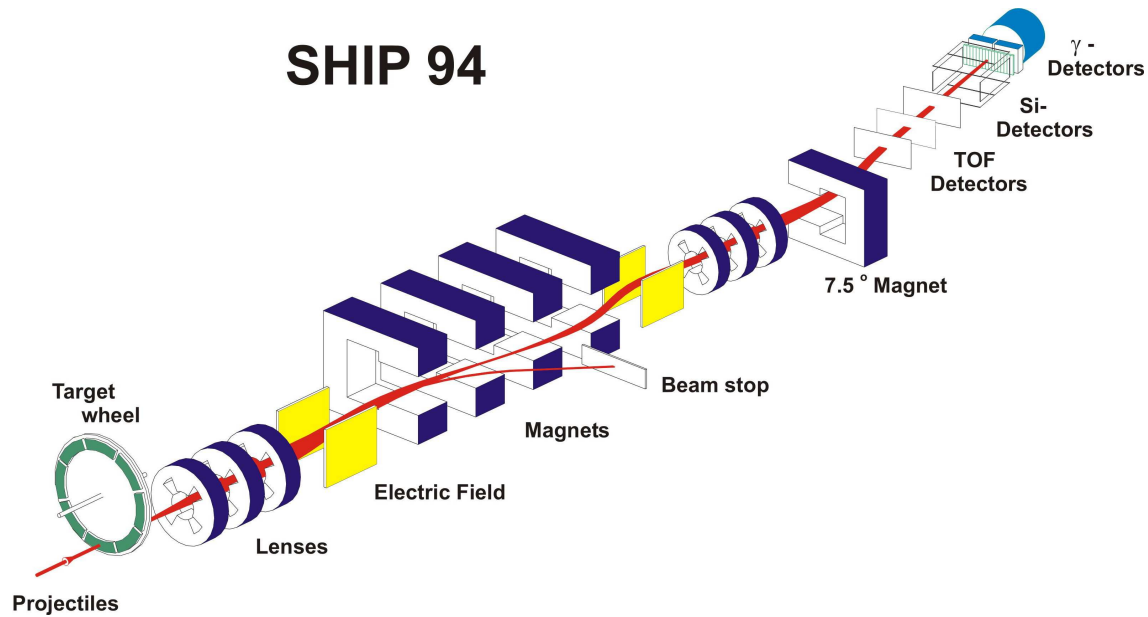$$F_{tot} \neq 0 \quad for \quad v \neq v_0 \tag{2.13}$$

Figure 2.3: The Separator for Heavy ion Reaction Products (SHIP) [21] is 11 m long. The filter is formed by two electric and four magnetic dipole fields plus two quadrupole triplets and a 7.5° deflection magnet.

This principle is the basis for the velocity filter SHIP.

SHIP has been designed as a two stage velocity filter with spatially separated electric and magnetic fields in the following arrangement: *quadrupole triplet, HV condenser, four dipole magnets, HV condenser, quadrupole triplet* (Fig. 2.3).

A 7.5 ° dipole magnet was added for background suppression. The main contribution to the background comes from scattered projectiles and target like nuclei which reach the stop detector, see Fig. 2.8. The projectiles have mostly larger radi of curvature then the ER, therefore they are less deflected in the electric and magnetic fields in such a way that they don't arrive at the focal plane detector. Instead, when the projectiles have low charge state, the rigidity of the ions is high and they would reach the detector system. This kind of background was reduced by installing a 7.5° deflection magnet (see Fig. 2.3).

The flight time of the reaction products considered here through SHIP is $\simeq 2\mu$s.

2.4   Transmission of the velocity filter

The transmission of the velocity filter for ER is strongly depending on the beam-target combination (see Fig. 2.4). The transmission can be defined as the ratio of ER implanted in the silicon detector and those produced in the reaction. The highest transmission we obtain for evaporation residues from symmetric beam-target combinations. If the projectile mass is much smaller than the target mass, the transmission drops considerably. In this case, the longitudinal momentum transfer to the evaporation residue is smaller then in the symmetric case. This leads to a larger straggling in the target material which results in a broader opening angle distribution of the reaction products.

Extensive simulation work was performed by Mazzocco et al. [22] to optimize the SHIP settings. The purpose was to obtain a better transmission of the selected evaporation nuclei and to provide a high background suppression. For this reason, a Monte-Carlo code (MOCADI) was extended to fusion evaporation reactions. To calculate the transmission through SHIP, reaction kinematics and ion optics have been combined into the MOCADI code. The results are compared with experimental results in Fig. 2.4.

2.5   Detectors

The detector system of SHIP is shown in Fig. 2.5. It is composed of three time-of-flight detectors (TOF), seven identical 16-strip silicon wafers and a clover type four crystal germanium detector.

2.5.1   Silicon detectors

To study the decay properties of heavy nuclei, silicon semiconductor detectors are employed. These nuclei decay mostly by α emission, electron capture or fission, with half-lives ranging from microseconds to days. The evaporation residues are implanted in the silicon stop detector and the energy of the particles and their decay products are measured. The active area of a strip detector used here is 35x80 mm^2. Each strip is position sensitive in the vertical direction with a resolution of 150 μm between the implanted ER and succeeding decay products. The optimum energy resolution reached was 14 keV obtained for α particles from ^{241}Am. The detector
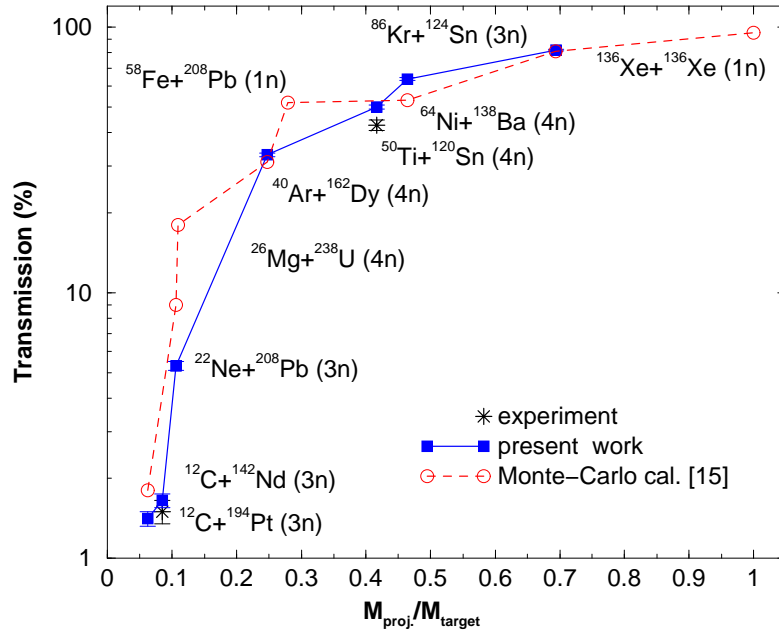
Figure 2.4: Transmission of the velocity filter SHIP. Squares represent the results of the simulations of M.Mazzocco et al. [22], the stars are experimental values and circles refer to previous calculations done by A.Popeko [15].

efficiency, i.e. the probability for an α particle to be stopped in the detector, is related to the implantation depth d of implanted nuclei and the range R of the emitted α particles and is given for $d \leq R$ by the equation $e_d = 1/2(d + R)/R$. Typical values for nuclei produced here are d $\approx$(5-10) μm and R $\approx$ (40-60)μm, and hence $e_d \approx 0.6$. Six further wafers are mounted in the backward hemisphere of the stop detector and form the box detector, see Fig. 2.5. They measure escaping α particles or fission products emitted in a solid angle of 80 % of 2π. In the backward detectors neighbouring strips are connected galvanically so that 28 energy sensitive segments are formed. The direction of an escaping α particle or fission fragment can be retraced roughly. The energy resolution obtained by summing the energy loss signal from the stop detector and the residual energy from the backward detector is minimum 40 keV for α particles.

All silicon detectors are cooled with alcohol to 253 K. The long time stability of the energy calibration was excellent. It shifts, i.e., less than 5 keV during an experiment of 12 weeks.

In front of the silicon detectors, there are ladders to put calibration sources or
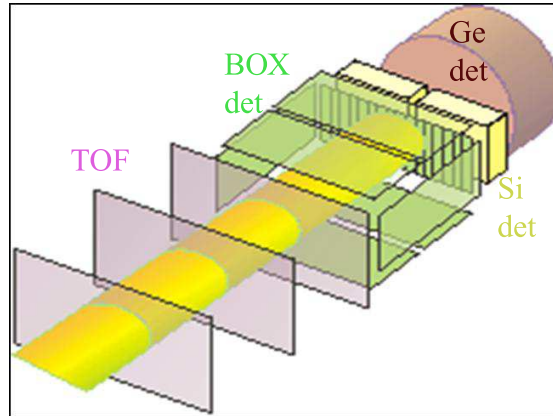
Figure 2.5: Sketch of the detector array. Three Time of flight detectors, the stop detector surrounded by the 6 further silicon detectors and Clover germanium detector.

degrader foils in the beam line without breaking the vacuum. The foils can be used to absorb a part of the low energetic background or/and to reduce the implantation energy.

2.5.2   Germanium detector

A clover type germanium detector is used to measure X rays and γ rays from implanted nuclei and decay products. Two types of clover detectors were used in the different experiments.

- VEGA detector. This is a Germanium 4 fold segmented superclover detector. Each crystal has a diameter of 70 mm and is 140 mm long.

- SHIP-Clover detector. This is a Clover with 4 crystals. Each crystal is ≈ 70 mm long and ≈ 54 mm of diameter.

To estimate the relative efficiencies for both Ge-detectors, γ lines from ^{133}Ba and ^{152}Eu in the range of 80-390 keV and 100-1410 keV were used. The absolute $\alpha - \gamma$ coincidence efficiency was estimated from the ratio $\sum N(\alpha - \gamma)/\sum N(\alpha)$. For the Vega type Clover detector using the transitions $\alpha(8421keV)$-$\gamma(209.8keV)$ of ^{247}Md and $\alpha(7539keV)$ -$\gamma(295.1keV)$ of ^{251}Md. ^{251}Md was produced via the reaction ^{209}Bi(^{48}Ca, 2n) ^{255}Lr which decays through α emission to ^{251}Md, while ^{247}Md was produced via the reaction ^{209}Bi(^{40}Ar,2n)^{247}Md. Both gamma transitions are considered as E1 [23] and on this basis corrections of the counting rate for internal
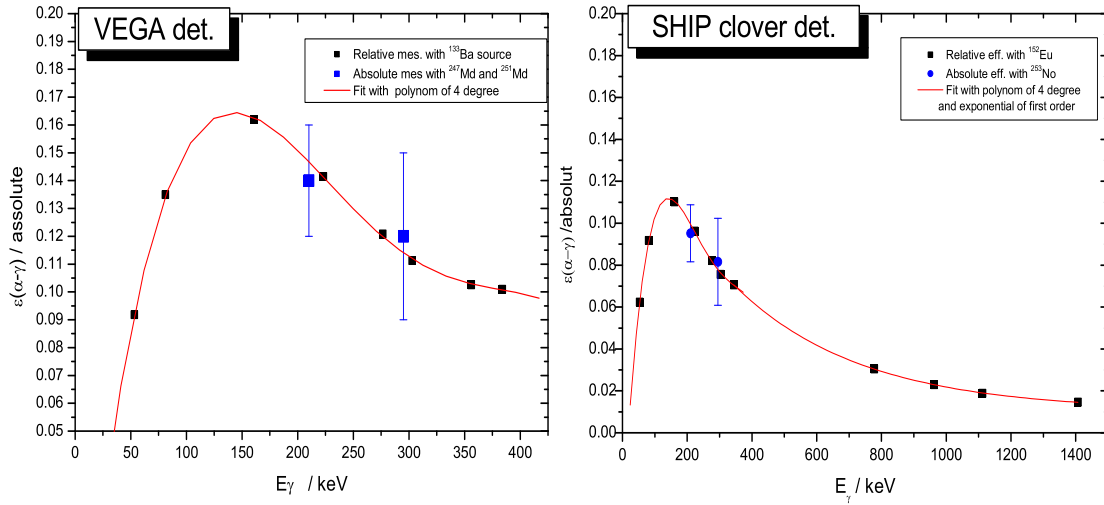
Figure 2.6: Efficiency of the Super Clover Detector (VEGA) and the SHIP clover detector. In the left graphic, the relative efficiency was obtained using a ^{133}Ba source. The absolute efficiency was determined from the decays of ^{247}Md and ^{251}Md. The relative efficiency is fitted with a Polynome of 4th degree. In the right plot, the relative efficiency was obtained using a ^{152}Eu source and a ^{133}Ba sources. The absolute efficiency was determined using α decay of ^{253}No in prompt coincidence with γs of ^{249}Fm. The relative efficiency is fitted with a combination of polynomial and exponential curves.

conversion were made according to [24]. For the second detector, the absolute efficiency was estimated from the transition $\alpha(8004 keV)$ -$\gamma(279.1 keV)$ of ^{253}No into an excited state of ^{249}Fm. ^{253}No was produced in the reaction ^{48}Ca(^{207}Pb,2n) ^{253}No. Also this gamma transition was considered as E1 [23]. The absolute $\alpha-\gamma$ coincidence efficiencies obtained in this way are shown in Fig. 2.6 for both detectors.

2.5.3   TOF detectors

In front of the silicon detectors there are three secondary electron foil detectors mounted 150 mm apart from each other [25]. The foils are made of carbon of 30 $\mu g/cm^2$ thickness. The time resolution of the foil detectors is ~ 700 ps. A schematic drawing of a single TOF detector is presented in Fig. 2.7 a. Between the foils an electric potential of 4 kV is applied in order to accelerate electrons emitted from the first foil when a heavy ion passes through. Perpendicularly, a magnetic field is applied in order to bend the electrons onto a microchannel plate (MCP) for further

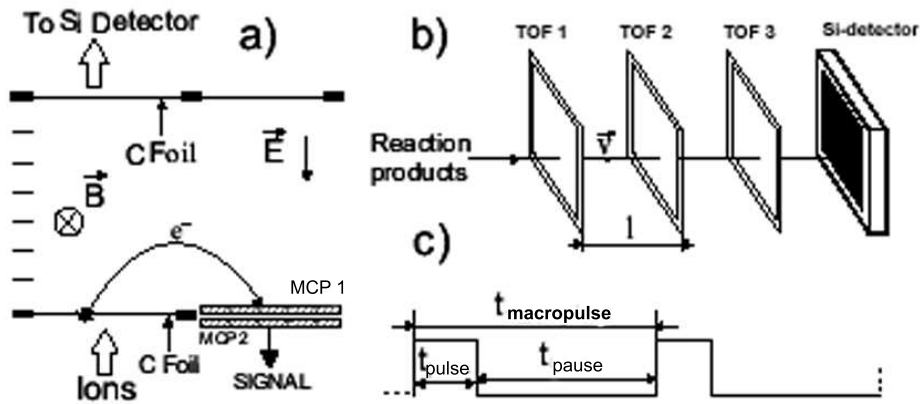amplification. The foils are selfsupporting and their transmission is 100 %.

Figure 2.7: Sketch of Time of Flight detector and working principle, [25]. b) Position of TOF detector configuration in front of Si detector. c) Beam macrostructure.

From the measured time of flight t and the energy E according to $E = \frac{m}{2}v^2 = \frac{m \cdot s^2}{2} \cdot \frac{1}{t^2}$, it is possible to identify different mass regions. In the ideal case, different masses form different parabolas in the energy versus TOF spectrum, but in practice energy resolution, time resolution, and the pulse height defect (due to recombination of electron-hole pairs in the detector) have to be considered. Nevertheless, it is
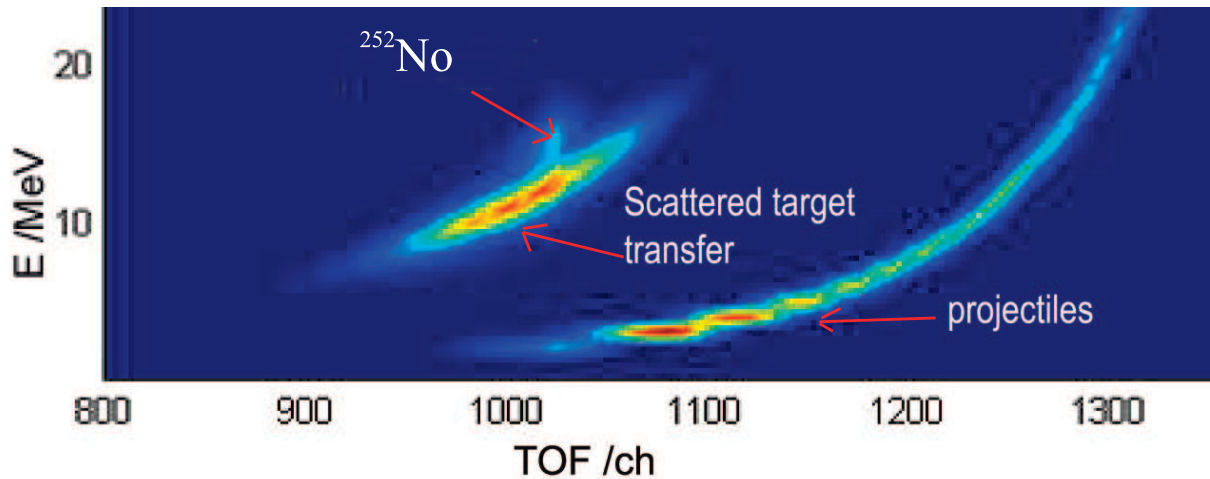

Figure 2.8: Plot of TOF (inverse time scale) versus energy (MeV) from the reaction ^{48}Ca on ^{206}Pb. The branches represent, with increasing energy, scattered projectiles, scattered target nuclei and ^{252}No evaporation residues.

possible to obtain a rough mass assignment for the implanted nuclei. For example

in the case of $^{286}112$,the mean atomic mass number determined was A $= 286\pm10$ [26]. Fig. 2.8 shows a plot of energy versus TOF (inverse time scale) from the reaction ^{48}Ca on ^{206}Pb. We clearly can distinguish two branches which can be attributed to projectile and target (e.g. transfer products) like nuclei. The small spot at E ~ 15 MeV and TOF ~ 1000 channels belongs to No evaporation residues.

Further, the TOF detector signals are used to distinguish between implanted nuclei and radioactive decays of previously implanted nuclei by requiring anticoincidence between TOF and stop detector.

The efficiency of the TOF detector is 98.8 %. To evaluate it, we use the following formula:

$$\epsilon_{TOF} = 1 - \frac{N_{notdetc}}{N_{allevent}} = 1 - \frac{N(EA) - N(Ep/0.75)}{N(E) - N(E_p/0.75)} \qquad (2.14)$$

where $N(EA)$ is the number of particles passing through the TOF detector, $N(Ep)$ the number of the particles in pause corrected for the pause range (0.75) and N(E) is the total number of α particles.

2.6 Data acquisition

As an example, the electronic scheme of the Si stop and backward box detector is shown in Fig. 2.9. Both ends of each strip are connected to a charge sensitive preamplifier. The total energy of the particle is obtained by summing the signals from both ends. Since the energy of the particle can vary from a few MeV (α particles) to more then 200 MeV (for fusion and fission products) two amplification channels are used (in the figure assigned as H high amplification and L low amplification). The amplification range extends up to 320 MeV for high amplification and up to 16 MeV for the low one.

For every stop detector strip, an energy signal and two position signals are processed. The strips are divided in two groups of eight strips each. One contains the odd number strips and the other one the even number strips. After amplification the signals from the two groups are multiplexed and processed to the ADCs.

The output from the 8-channel multiplexers (mixer) is inhibited by the trigger signal supplied by the pattern trigger (PT), which is used also for the identification of the strip number. In this way, the mixer processes signals from single strip at a time in order to avoid noise and off-set summing from the other seven strips.

For the processing of the ADC signals, we set up a new ADC multiplexer (AMUX) based data acquisition system. The AMUX system (NIM based) was developed by Hoffmann et al. [27]. The AMUX module has the property to readout and control 4 spectroscopy ADCs. Nine AMUX modules are chained on the GTB (GeraeTe Bus). GTB is a differential bus used for list mode data transfer between a control and readout module (SAM) and the AMUX modules. The SAM module serves for event building and communication with the DAQ CPU.

The trigger bus connects all AMUX modules with the control port of the SAM and synchronizes the system of SAM and AMUX modules (see Fig. 2.10). The first firing ADC triggers the coincidence time. All ADC signals that fall into the coincidence interval are accepted. At the end of the coincidence time the pattern registers (each AMUX contains a 16 bit pattern register) are clocked and the conversion time of the ADCs starts. The end of the conversion time triggers an interrupt on the SAM, which starts the readout (see Fig. 2.11). The data are buffered in an event queue with a length of 400 events on the AMUX modules. The readout of the events to the SAM is done asynchronously by sending a readout signal from the SAM to the AMUX modules via the GTB. The SAM is then read out with a VME processor
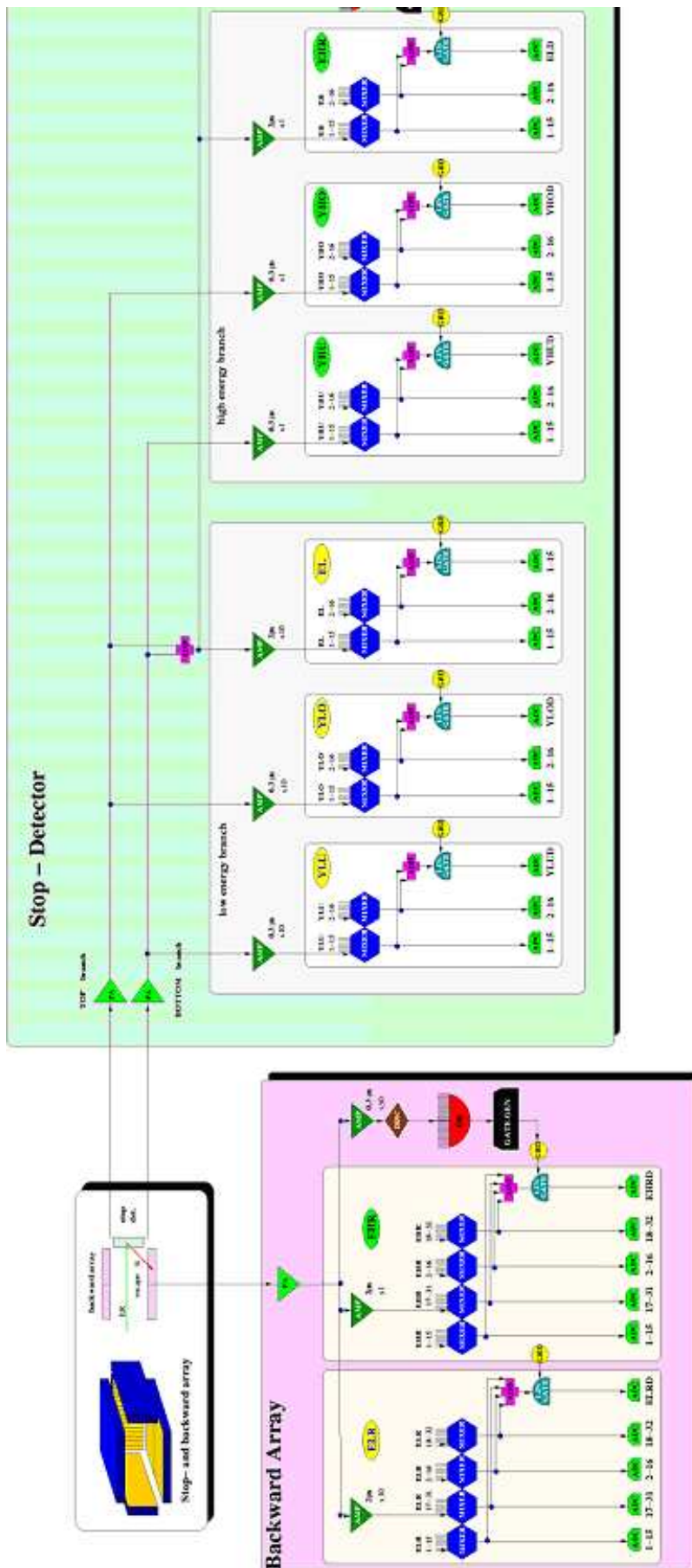
Figure 2.9: Block diagram of the focal plane detector (stop and box detectors) with associated electronics.
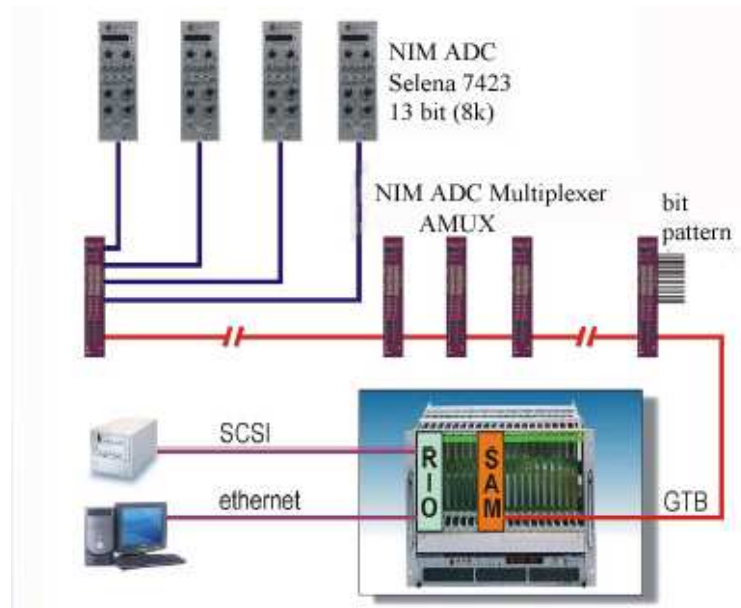
Figure 2.10: Example of the connection of the new data acquisition system. Four ADCs are connected to one AMUX. The AMUX modules are connected to a SAM3 module through GTBM. Each AMUX contains a 16 bit pattern unit. It is possible to connect to one port of the two inputs of a SAM3 up to 15 AMUX modules, so in total 30 AMUX modules and 120 ADCs can be read out by one SAM3. Finally, the events are read out by the DAQ processor which prepares the data for mass storage and online analysis. The new ADC multiplexers have been developed for SHIP by electronics group of GSI [27].

(RIO) running a MBS (Multi Branch System) data acquisition system developed by the GSI electronics group.
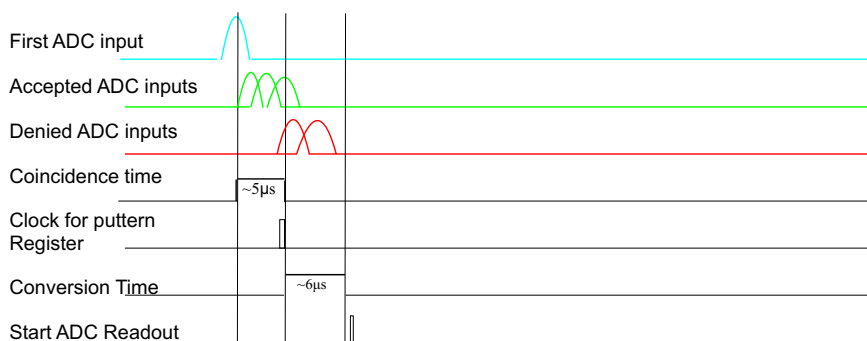

Figure 2.11: Timing diagram for a AMUX readout cycle.
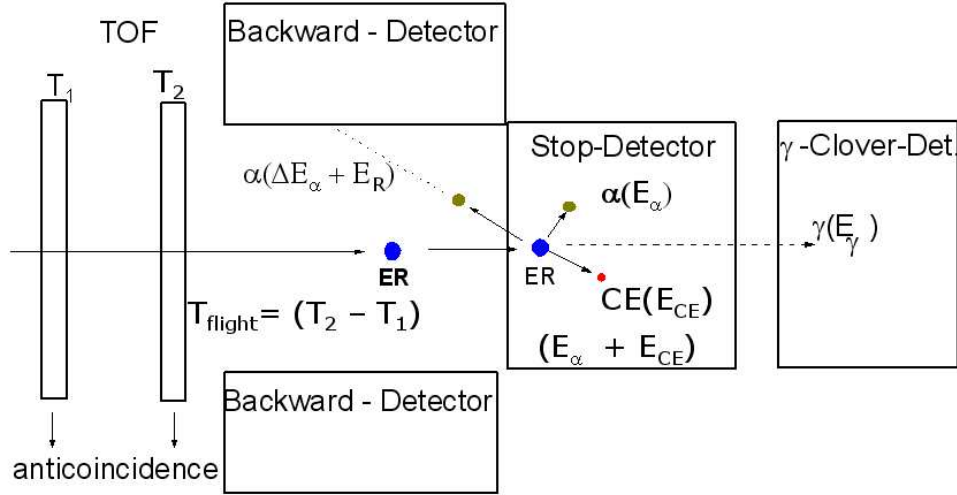
2.7 Focal plane decay spectroscopy

Figure 2.12: Schematic drawing of the detection system.

2.7.1 Gamma-electron coincidences

If an implanted nucleus is an isomeric state, it can decay via α emission, spontaneous fission (sf) or by electromagnetic transitions. This latter case proceeds usually through a series of several levels decaying by both, internal conversion and γ decay in prompt cascade towards the ground state, as it will be shown in the next chapters for ^{252,254}No. The occurrence of internal conversion electrons (CE) is due to highly converted transitions. For example, in even even nuclei with $A > 250$, the typical energy for the $4^+ \rightarrow 2^+$ and $2^+ \rightarrow 0^+$ transitions of the rotational band are ~ 100 keV and ~ 40 keV. Such low energy transitions are strongly converted; e.g. for E2 transitions with the above given energies, the conversion coefficient are $\sim$30 (for 100 keV) and $\sim$1400 (for 40 keV), respectively. A sketch of a de-excitation cascade via γ and CE emission is shown in Fig. 2.13. Internal conversion electrons coming from such a cascade are measured in the stop detector. Electrons with energies up to $\sim$ 300 keV can be fully stopped in the 300 μm thick Silicon detector. Requiring the coincidence between these electrons and the γ events became crucial to clean the γ spectra from unwanted background (γ rays from environment or accelerator).
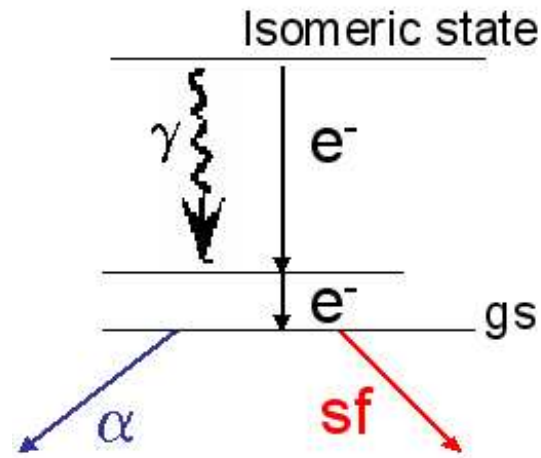
Figure 2.13: Sketch of the de-excitation of an isomeric state into the ground state via γ and/or CE emission.

Further on, requiring the correlation with the subsequent decay (α or sf) of the ground state, after the decay of the isomer, can provide an unambiguous identification of the isomer.

For example, the isomeric state in ^{252}No was identified by delayed coincidences of ER-(CE,γ)-α,sf (^{252}No). The isomer decays via a complicated pattern including several transitions, which are highly converted, to the ground state; then the ground state decays after a mean time of ~ 2.42 s via α to ^{248}Fm or by sf.

2.7.2   Recoil α or sf correlation

Figure 2.14: Sketch of possible decay modes (α, Sf, or γ) of a nucleus.

If an evaporation residue is implanted into the silicon detector, it can be followed

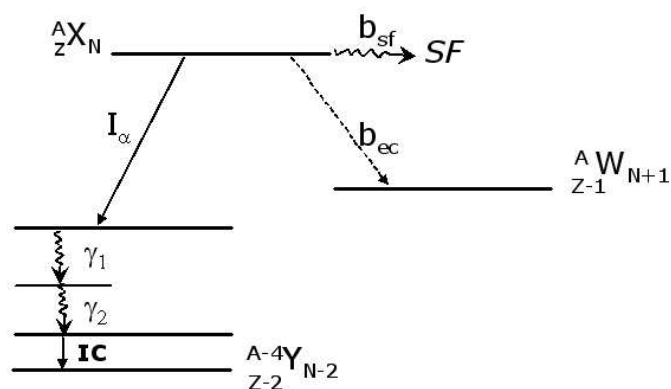by a series of α decays terminated eventually by a sf. The identification of the recoil and its decay chain is based on the requirement that the recoil and its decay products must occur at the same position in the detector (± 0.3 mm due to the detector resolution) within a given time window. The time window is usually determined by the half-lives of the chain members.

If an α decay feeds into an excited state of the daughter nucleus, it can de-excite via γ or CE emission. Since also the CE are recorded in the silicon detector, it can lead to energy summing between α particles and CE. This effect is shown in Fig.2.15 in the case of ^{253}No. The upper spectrum shows α lines from ^{253}No and ^{249}Fm influenced by e^- summing, which causes a shift of the lines towards higher energy (In this specific case essentially from ~ 8.00 MeV to ~ 8.05 MeV. The lower spectrum was taken by putting a 8 μm thick mylar foil in front of the detector, which lowers the implantation depth of the recoils and thus the probability for energy summing, leading to an enhanced intensity of the 8.0 MeV line and a reduced intensity of the 8.05 MeV line.
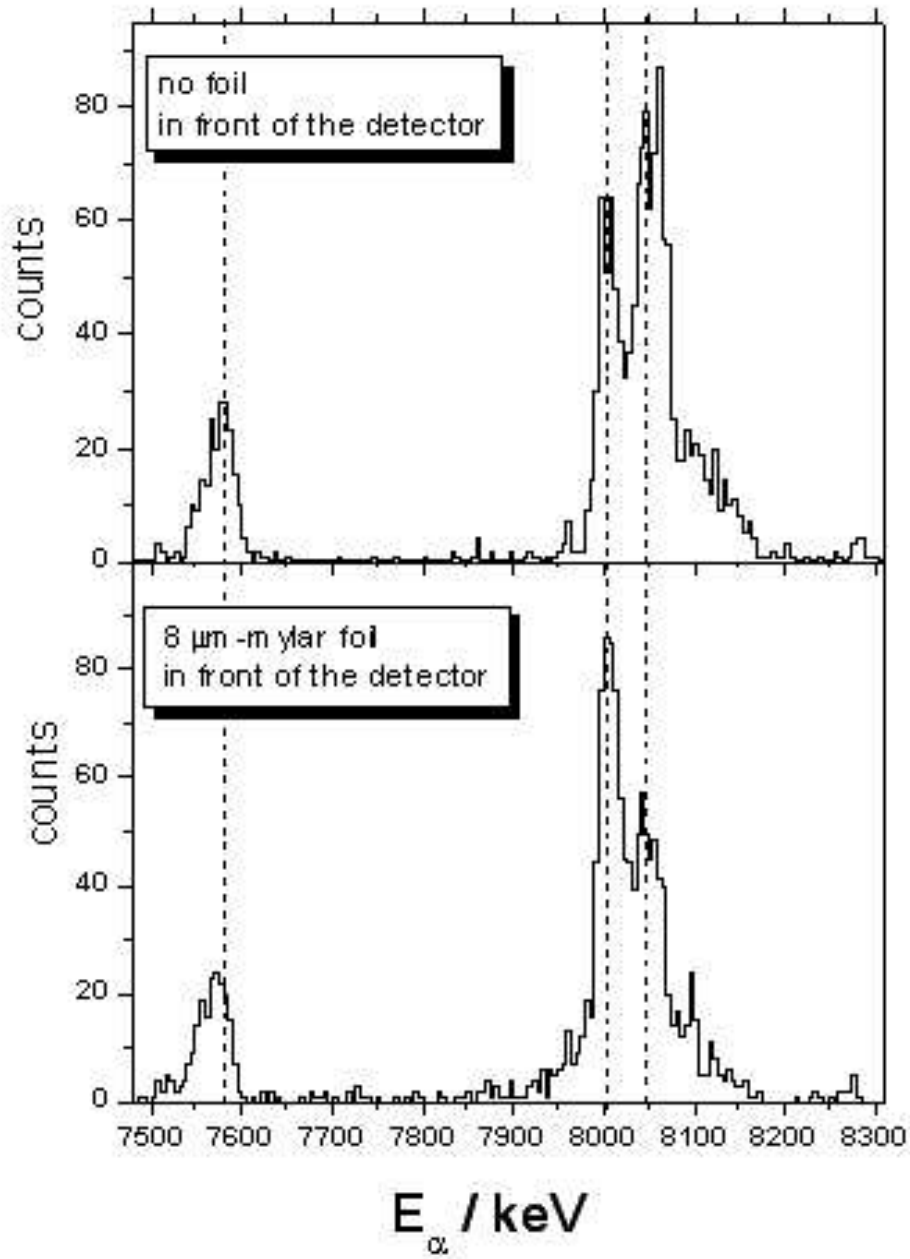
Figure 2.15: Influence of energy summing of conversion electrons with alpha particles on the shape of alpha spectra in the case of ^{253}No.

Chapter 3

Experimental Results: ^{260}Sg

3.1 Excitation function

Among the possible candidate nuclei for K isomers, the nucleus ^{260}Sg is of specific interest. According to calculations [1], two K isomers should exist at relatively low excitation energies ($E^* < 1.5$ MeV).
Two experimental runs, aimed to observe the decay of a possible isomeric state, were performed using different projectile - target combinations. In a first step, the optimum production reaction leading to ^{260}Sg was searched for. In the second experiment, we searched for hints of a possible isomeric state in this nucleus.

We investigated two collision systems, ^{54}Cr+^{208}Pb and ^{54}Cr+^{207}Pb, to study the exit channels of the reaction and the production rates of ^{260}Sg. The rates for production of heavy and superheavy nuclei are determined by increasing re-separation of projectile and target like nuclei in the entrance channel due to a dynamical hindrance of fusion at increasing $Z_p \times Z_t$ and the competition between neutron evaporation and fission of the compound nucleus.

First experimental data on ^{260}Sg were obtained in previous experiments at SHIP in irradiations of ^{208}Pb and ^{207}Pb with ^{54}Cr beams [28]. The measured cross-sections reported for the synthesis of ^{260}Sg by one and two neutron evaporation were 22^{+50}_{-18} pb (E_{beam}= 4.90×A MeV) and 280± 50 pb (E_{beam}= 4.92×A MeV) using ^{207}Pb and ^{208}Pb targets, respectively. Enhanced data were obtained in a recent experiment at SHIP by Streicher et al. [29]. The maximum of the excitation function for the 2n channel in the reaction ^{54}Cr+^{208}Pb was found at a beam energy of 4.97×A MeV, corresponding to a cross section of 0.69 ± 0.17 nb.
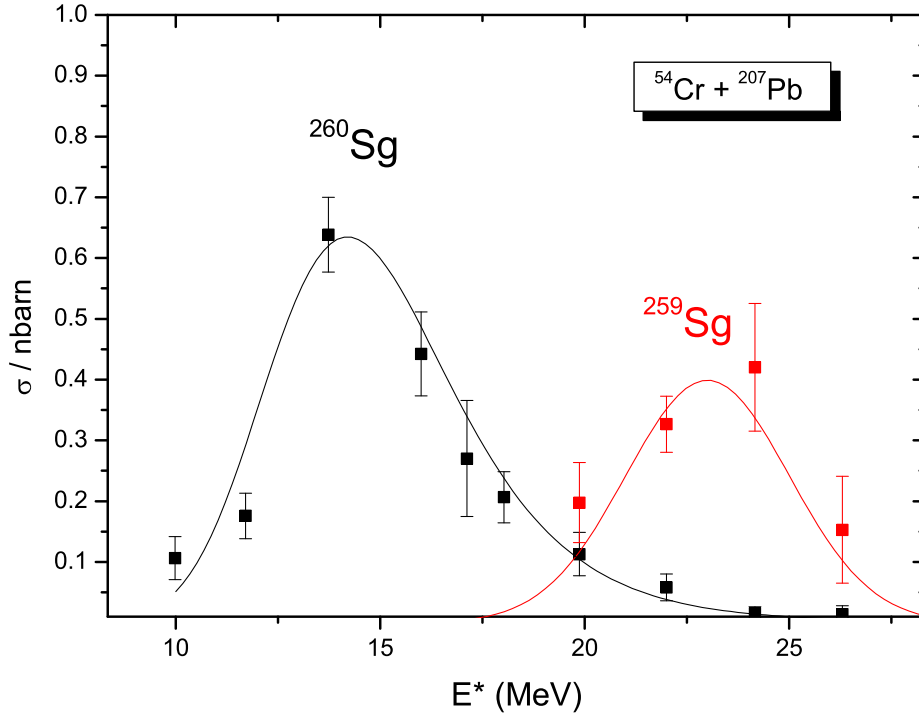
Figure 3.1: Measured cross sections for xn- products from the ^{54}Cr+^{207}Pb reaction as function of the excitation energy of the compound nucleus ^{261}Sg. The error bars respect only the statistical uncertainty. The lines are gaussians fits to the data.

3.1.1 ^{207}Pb(^{54}Cr,xn) $^{261-x}$Sg

We measured the excitation function for this reaction at 10 different beam energies between 4.67×A MeV and 5.05×A MeV (see table 4.2). This corresponds to excitation energies of the compound nucleus ^{261}Sg from $E^\star = 10$ MeV to $E^\star = 26$ MeV. The excitation energies $E^\star$, calculated by using the mass excess data from Myers and Sviatecki [30], refer to the production in the center of the target. The energy loss of the projectiles in the first half of the target, calculated using the SRIM code [31], was $\Delta E \approx 3$ MeV. The target was composed of a PbS layer of 379 $\mu g/cm^2$ evaporated on a carbon layer of 42 $\mu g/cm^2$ and covered with a 10 $\mu g/cm^2$ carbon layer.

The measured excitation functions for the 1n and 2n evaporation channels are

shown in Fig. 3.1. To determine the number of ^{260}Sg nuclei produced, we summed over all observed fission events from ^{260}Sg and its daughter nucleus ^{256}Rf. Since the fission branch b_{sf} of ^{260}Sg is 77% and the alpha branch of ^{256}Rf is $b_\alpha \simeq 3\%$ [32, 29], one can assume that the sum of the observed fission events corresponds to $\sim 99\%$ of the produced ^{260}Sg nuclei.

The cross section was calculated from the number of observed evaporation residues N_{ER} according to

$$\sigma = \frac{N_{ER}}{N_p d \cdot \epsilon N_A / m_t} \tag{3.1}$$

N_p is the number of projectiles, d is the surface mass density in g/cm^2, N_A is the Avogadro number, m_t is the mass of the target nucleus and ϵ is the total detection efficiency.

To obtain the maximum production cross section and the corresponding excitation energy of the compound nucleus a Gaussian was fitted to the experimental points (full lines in Fig. 3.1). In the case of 1n evaporation channel (^{260}Sg), the curve is fitted with an asymmetric gaussian

$$\frac{A}{w \cdot sqrt(\pi/2)} \cdot exp^{(-2\cdot(x-xc)^2/(w^2 - c\cdot x + d\cdot x^2))} \tag{3.2}$$

where A is the area of the curve, xc is the maximum of the curve, and w is the width, c and d are fit parameters. The asymmetry is due to the presence of the Coulomb barrier at $\sim 4.2 \times A$ MeV. Values of $\sigma_{max,1n} = (0.63 \pm 0.08)$ nb at $E^\star = (14.1 \pm 0.2)$ MeV were obtained for the 1n (^{260}Sg) evaporation channel. For the 2n evaporation channel $\sigma_{max,2n} = (0.39 \pm 0.10)$ nb at $E^\star = (23.0 \pm 0.7)$ MeV was obtained.

The width (FWHM) obtained from fits to the measured excitation functions were (4.04 ± 0.33) MeV for the 1n channel and (4.89 ± 1.02) MeV for the 2n channel. The given uncertainties are due to the fitting procedure.

3.1.2 ^{208}Pb(^{54}Cr,2n) ^{260}Sg

The second system studied was ^{54}Cr on ^{208}Pb. Information on this reaction for the 1n and 2n evaporation channel was already provided by Streicher et al. [29]. To check the results we repeated the measurements for the 2n evaporation channel at three different beam energies. The results are shown in table 3.2 and in Fig. 3.2.

Reaction	E_{Lab}/A MeV	E^* [MeV]	cross section [nb]	
			1n(^{260}Sg)	2n (^{259}Sg)
^{54}Cr+^{207}Pb	4.67	9.98	0.11 ± 0.04	
	4.71	11.7	0.17 ± 0.04	
	4.76	13.7	0.64 ± 0.06	
	4.81	16.0	0.44 ± 0.07	
	4.84	17.1	0.27 ± 0.10	
	4.86	18.0	0.20 ± 0.04	
	4.90	19.9	0.11 ± 0.04	0.19 ± 0.06
	4.95	22.0	0.06 ± 0.02	0.32 ± 0.05
	5.00	24.2	0.02 ± 0.01	0.42 ± 0.11
	5.05	26.3	0.01 ± 0.01	0.15 ± 0.09

Table 3.1: Production cross sections at given bombarding and excitation energy for the ^{260}Sg and ^{259}Sg in the reaction ^{54}Cr + ^{207}Pb.

In Fig. 3.2 our results are compared with those from Streicher et al. [29]. For the cross section calculations for the 1n channel, only the numbers of α decays of ^{261}Sg were taken into account, since ^{261}Sg has a fission branch of only (0.6±0.2) % [29] and a EC branch of (1.3±0.3) % [29].

For the production of ^{260}Sg, we found the maximum of the excitation function at 22.6 ± 0.4 MeV with 0.49±0.11 nb. The result was obtained by a gaussian fit (not shown in the figure) to the measured points listed in table 3.2. The result agrees well with the previous measurement of Streicher et al. [29].

Reaction	E_{Lab}/AMeV	E^* [MeV]	cross section [nb]
			2n (^{260}Sg)
^{54}Cr+^{208}Pb	4.93	21.30	0.35(0.09)
	4.98	23.44	0.44(0.08)
	5.00	24.30	0.35(0.09)

Table 3.2: Production cross sections at given bombarding and excitation energies measured for the ^{54}Cr + ^{208}Pb reaction.

In summary, we obtained for ^{260}Sg within the error bars the same production cross section in the reactions ^{207}Pb(^{54}Cr,1n)^{260}Sg and ^{208}Pb(^{54}Cr,2n)^{260}Sg.
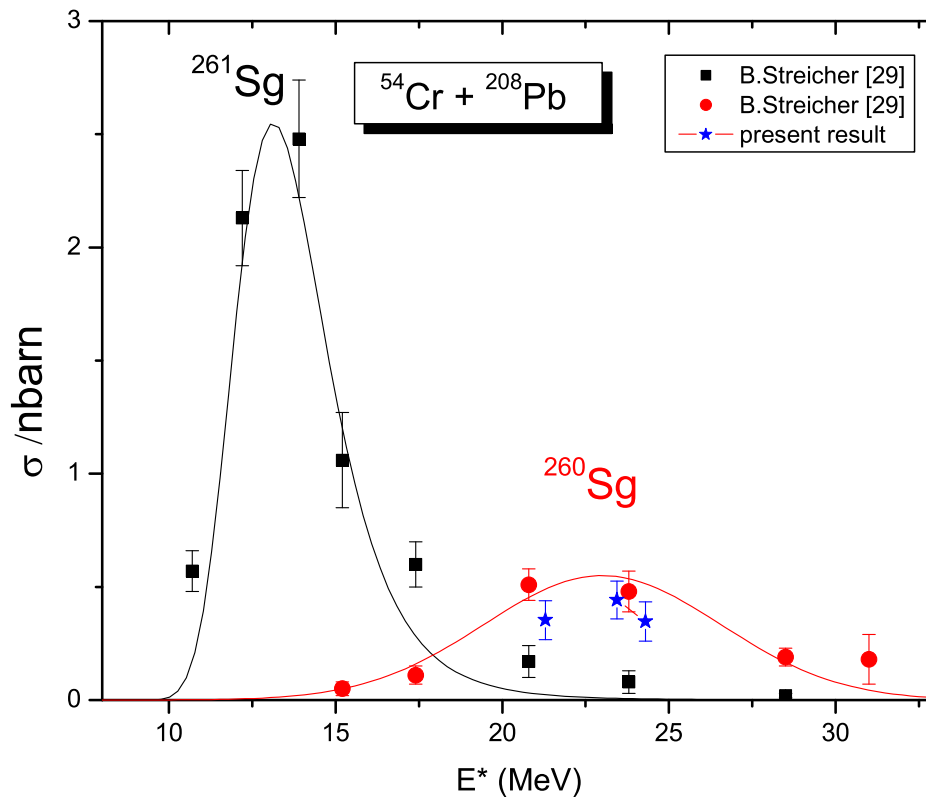
Figure 3.2: Measured cross sections for the 1n and 2n channels for ^{54}Cr+^{208}Pb from the work of Streicher et al. [29] and the 2n channel from ^{54}Cr+^{208}Pb reactions (present work) as a function of the excitation energy. The error bars reflect only the statistical uncertainty.

3.2 Spectroscopy

3.2.1 Results of former experiments

Experimental data on ^{260}Sg obtained in previous SHIP experiments by Münzenberg et al. [28] and Streicher et al. [29] are summarized in table 3.3.

In the following chapter, the results of our new investigation will be presented.

Isotope	E_α (MeV)	$T\alpha_{1/2}/ms$	b_{sf}	No. of decays	Reference
^{260}Sg	9.77	$3.6^{+0.9}_{-0.6}$	50^{+30}_{-20}	9	[28]
	9.72	3.6		2	[28]
	9.758	$3.0^{+0.7}_{-0.5}$	77 ± 9	23	[29]
	9.715	$6.7^{+9.1}_{-2.5}$		4	[29]
	9.675	$2.0^{+2.7}_{-0.7}$		4	[29]
^{256}Rf	8.786	$5.1^{+1.0}_{-0.7}$	97 ± 2	2	[29]

Table 3.3: Summarized spectroscopic data of former experiments obtained for from the reaction ^{54}Cr(^{208}Pb,2n)^{260}Sg.

3.2.2 Decay spectroscopy of ^{260}Sg

Figure 3.3 shows the α spectra accumulated in the energy range from 8 to 10 MeV. Data from ^{54}Cr on ^{207}Pb and ^{54}Cr on ^{208}Pb are added up. Figure 3.3 a) displays
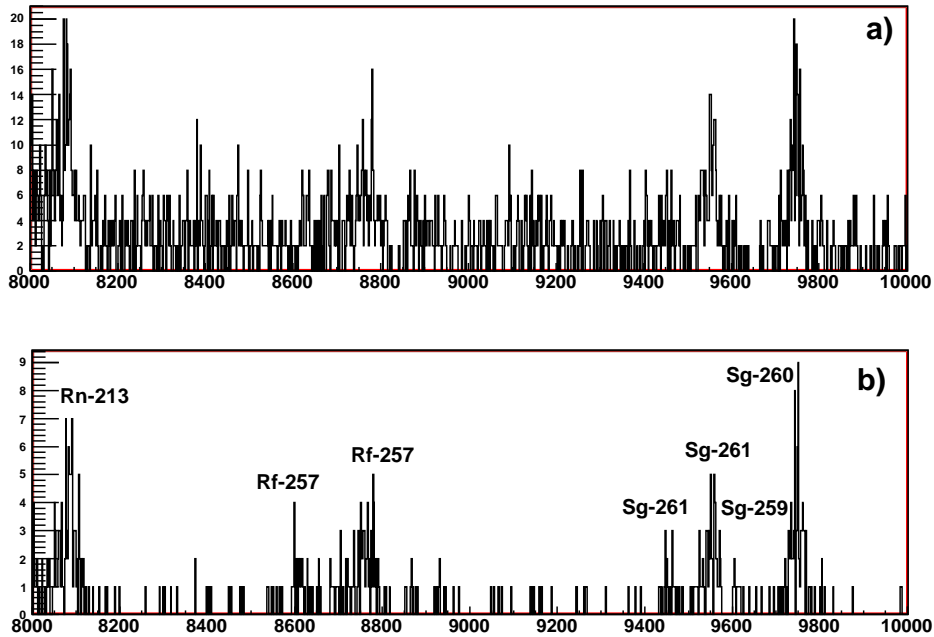

Figure 3.3: Alpha spectra from the reactions ^{54}Cr + ^{208}Pb and ^{54}Cr + ^{207}Pb reactions. a) α spectrum requiring anticoincidence condition with the TOF signal. b) α particles recorded during the beam pause.
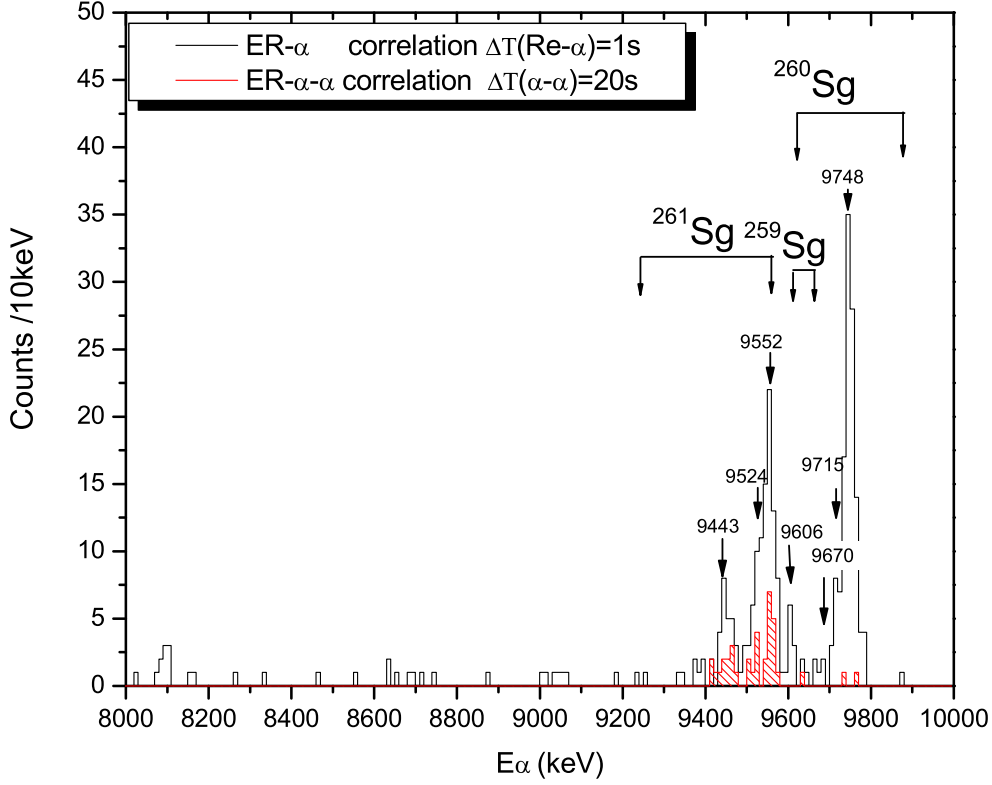
Figure 3.4: Alpha particles in correlation with evaporation residues. The red line represents the α particles requiring ER-α-α correlations within $\Delta T(ER - \alpha)$=1s and $\Delta T(\alpha - \alpha)$=20s.

an α-decay spectrum requiring only the anticoincidence between the time-of-flight detector and the stop detector signals. In Fig. 3.3 b) the alpha decays occurring in the pause between the UNILAC beam bursts are shown. The spectrum shows the α-decay of the fusion evaporation products ^{259}Sg, ^{260}Sg, and ^{261}Sg together with the ^{261}Sg-daughter ^{257}Rf and the transfer product ^{213}Rn. In order to further reduce the background events in the measured α spectra, we applied different correlation conditions which will be explained in the following.

The spectrum in Fig. 3.4 shows α decays following the implantation of a heavy ion. The position difference for correlated events was limited to $\pm$ 1 mm between α

and ER. The maximum time difference between α decay and implanted nucleus was set to 1 s. This time interval was chosen with respect to the half-lives of ^{259,260,261}Sg and to limit the number of random correlations. A total of about 275 α-decays in the energy region E_α= 9-10 MeV, attributed to ^{259,260,261}Sg, was observed.

By requiring delayed $ER - \alpha - \alpha$ coincidences, we obtained the spectrum represented by the red dashed line in Fig. 3.4. Only three counts of ^{260}Sg in delayed coincidence with α-decays of ^{256}Rf are observed which is consistent with the known small α branch of ^{256}Rf [32, 29].
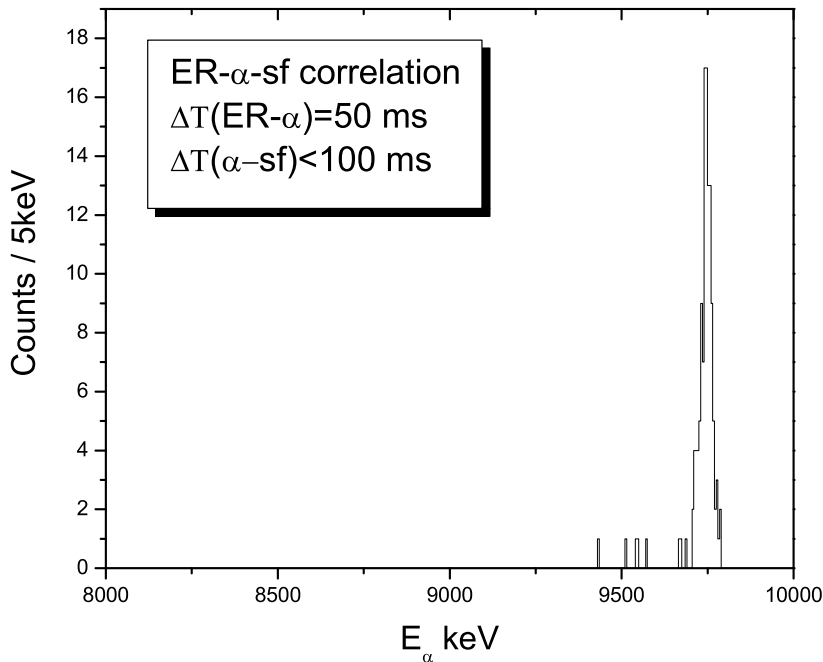
Figure 3.5: Spectrum of α-particles from ER-α-sf correlations in ^{54}Cr + ^{208}Pb and ^{54}Cr + ^{207}Pb. The time windows were $\Delta T(ER - \alpha)$=50 ms and $\Delta T(\alpha - sf)$ <100 ms.

By requiring $ER - \alpha - sf$ correlations, we only observed ^{260}Sg (see Fig. 3.5). In this case, the correlation time between α and ER was $\Delta T(ER - \alpha)$=50 ms, and between α and sf, it was $\Delta T(\alpha - sf)$=100 ms. The energy window for the α particles was set between 8 MeV and 13 MeV to observe possible high-energy alpha transitions of ^{260}Sg. In total, we observed a number of 140 α decays with full energy release the stop detector.

3.2.3 Branching ratios and half lives of ^{260}Sg and ^{256}Rf
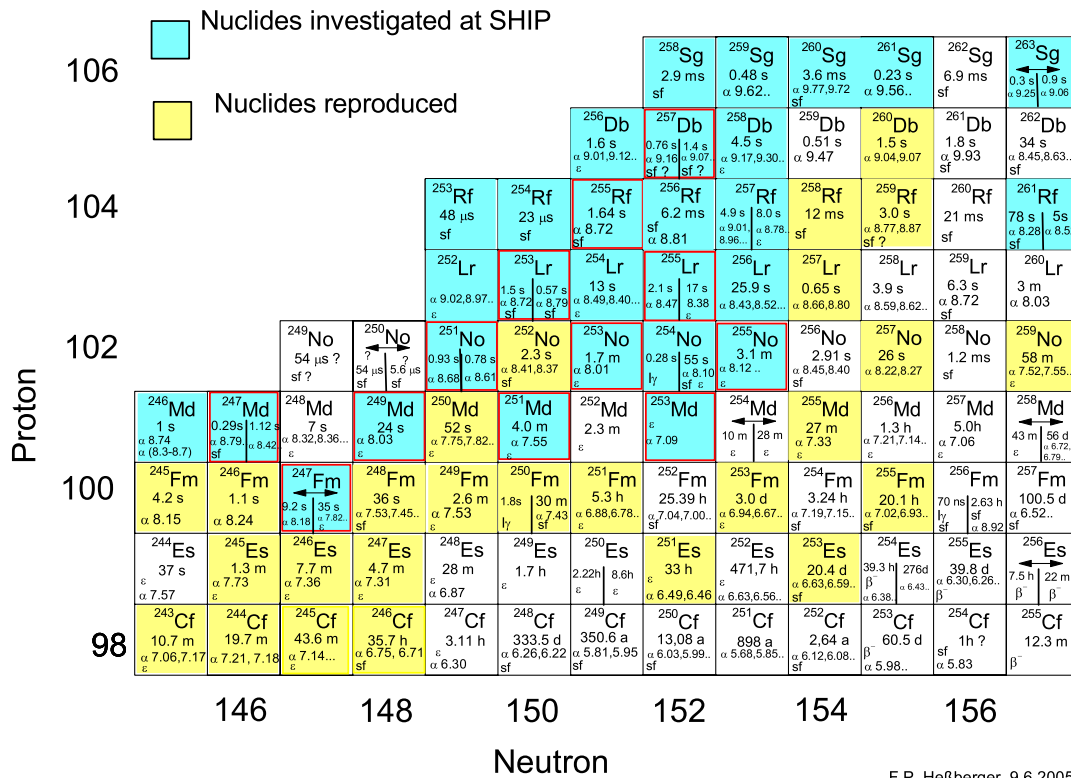
Figure 3.6: Chart of nuclides showing the experimentally investigated isotopes for Z=98-106 and N=145-157.

Figure 3.6 shows an excerpt of the nuclear chart in the region of ^{260}Sg. As can be seen ^{260}Sg decays via α emission to ^{256}Rf and via sf. ^{256}Rf decays mainly by sf while its alpha-branch is small.

To estimate the sf branching ratio of ^{260}Sg we, compared the intensities of ^{260}Sg in ER-α correlations and ER-sf correlations with no preceding α. To discriminate the directly fissioning component of ^{260}Sg from the α preceded fission of ^{256}Rf, only sf events with no preceding α particle were taken into account. A careful search for possible escape α-decays not registered by the detector has been carried out and an upper limit of only 4 % was estimated. Thus, we estimated a fission branch of ^{260}Sg of $71 \pm 3\%$.

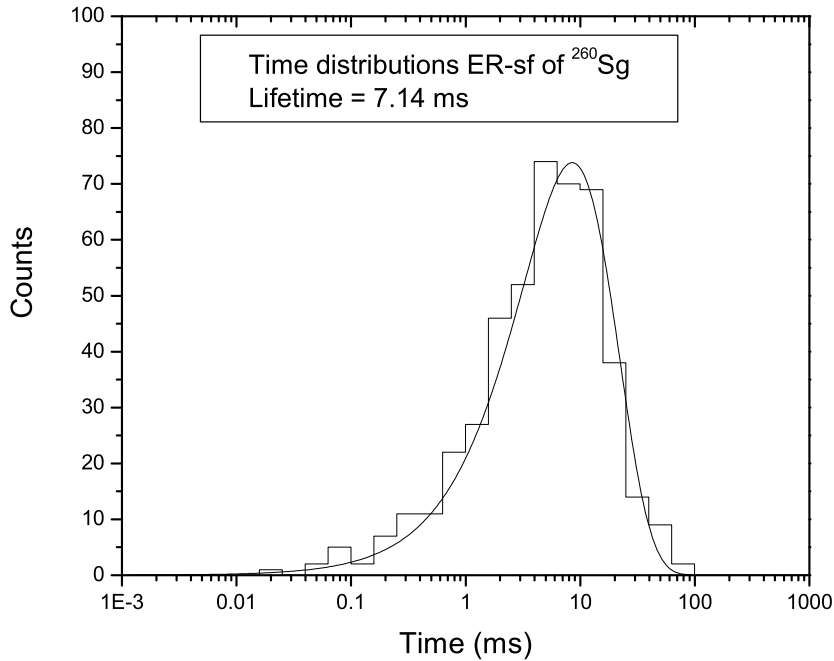Figure 3.7: Time distribution of spontaneous fission events of ^{260}Sg from ER-sf correlations. The curve represents the density distribution of counts in a radioactive decay on a logarithmic time scale.

We obtained the life time for the sf-decay of ^{260}Sg from the time differences between implanted ER and sf events. The corresponding decay curve is shown in Fig. 3.7. It represents the density distribution of sf events on a logarithmic time scale with logarithmically increasing bin size [33]. The peak position determines the life time. This method was applied to discriminate possible contributions from different sources having different lifetimes. The lifetime obtained for sf of ^{260}Sg is 7.14 ± 0.47 ms, corresponding to a half-life of 4.95 ± 0.33 ms.

The ^{256}Rf α-decay branching ratio was deduced by comparing the intensity of the ^{260}Sg peak in ER-$\alpha(^{260}Sg)$-α and ER-$\alpha(^{260}Sg)$-sf correlations. Correction for the α and sf detection efficiencies ($\epsilon_\alpha = 55\%$ and $\epsilon_{sf} = 99\%$) are included in the calculation. The value obtained is $b_\alpha = (1.5 \pm 0.9)$ %.

In the case of sf of ^{256}Rf the lifetime was obtained from the time difference, ΔT, between an α particle of ^{260}Sg with an energy between 9.6-9.8 MeV and a fission event. The total number of sf events of ^{256}Rf is 220. The half-life was determined
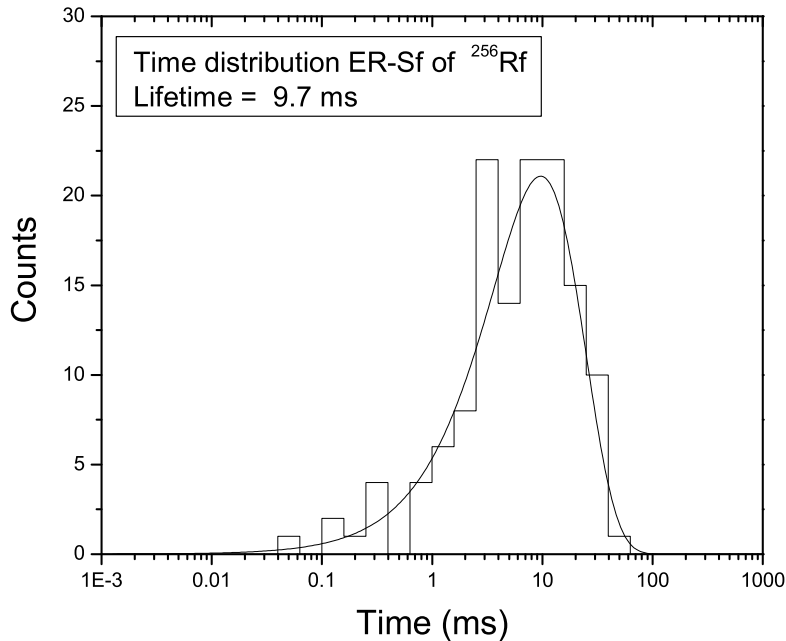
Figure 3.8: Time distribution of spontaneous fission events of ^{256}Rf from ER-α-sf correlations. The curve represents the density distribution of counts in a radioactive decay on a logarithmic time scale.

with the same method as for ^{260}Sg. From the curve in Fig. 3.8, a half-life of 6.7$\pm$0.9 ms (the corresponding lifetime is 9.7$\pm$1.3 ms) was found, which is in good agreement with the result of G. Münzenberg et al. [28] and with the direct measurement of F.P. Heßberger et al. [32].

3.2.4 Deduced level scheme for ^{260}Sg and ^{256}Rf

In Fig. 3.9, we show the alpha spectrum of ^{260}Sg resulting from ER-α correlations in the energy range of 9.4-9.9 MeV. The α line indicates a small shoulder towards lower energies. It can be fitted by two Gaussians resulting in E_α=9.748$\pm$0.001 MeV for the main peak and 9.715$\pm$0.003 MeV for the small side peak. The main peak is attributed to the ground state - ground state transition.

It is known from lighter even-even nuclei that the 2$^+$level of the ground state rotational band is typically located at 40-60 keV above the ground state. The
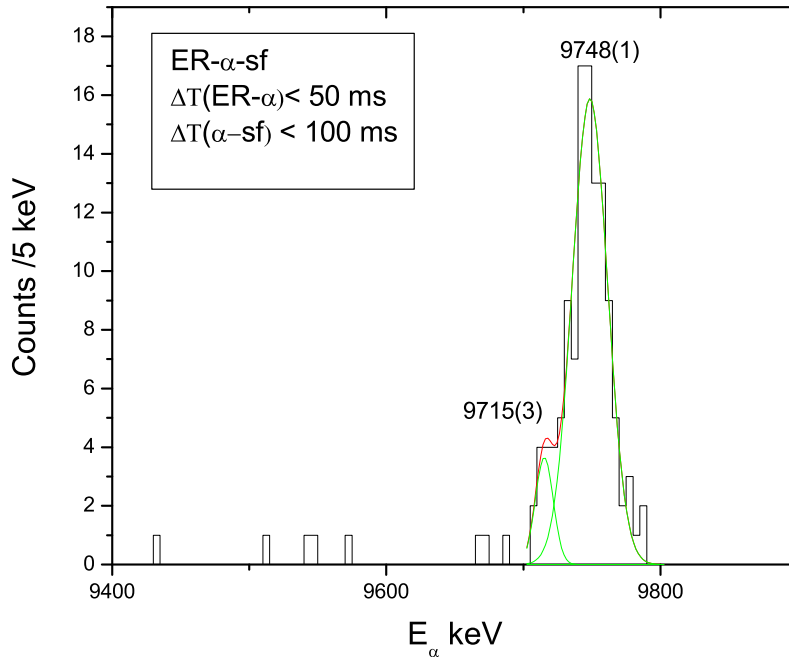
Figure 3.9: Alpha decay spectrum of ^{260}Sg resulting from ER-α-sf correlations.

probability to populate the 2^+ level in the daughter

nucleus is usually about 15-25 % [34].

The estimated energy of the 2^+ state in ^{256}Rf is 43.4 keV [35], where the rotational energy of the I^+ states were calculated according to formula 1.9 using the moment of inertia calculated by Sobiczewski et al. [35]. The calculated level schemes of the rotational bands in ^{260}Sg and ^{256}Rf are shown in Fig. 3.10. The $2^+ \rightarrow 0^+$ transition is highly converted and so the corresponding α line is shifted towards the main line by energy summing between conversion electrons and α particles. Therefore a) the transition into the 2^+ level cannot be observed as a "separated line" and b) the energy difference of the two Gaussians is only 33 keV and thus lower than the expected energy for the 2^+ level. A similar behavior has been observed in SHIP experiments for lighter nuclei, e.g., ^{254}No.

The time distribution of the 9.715 MeV events shows two components with life-times of $0.14^{+0.05}_{-0.03}$ ms and $5.43^{+1.03}_{-0.75}$ ms. The long living component is consistent with the lifetime of the line at 9.748 MeV. The two components can be seen in a two
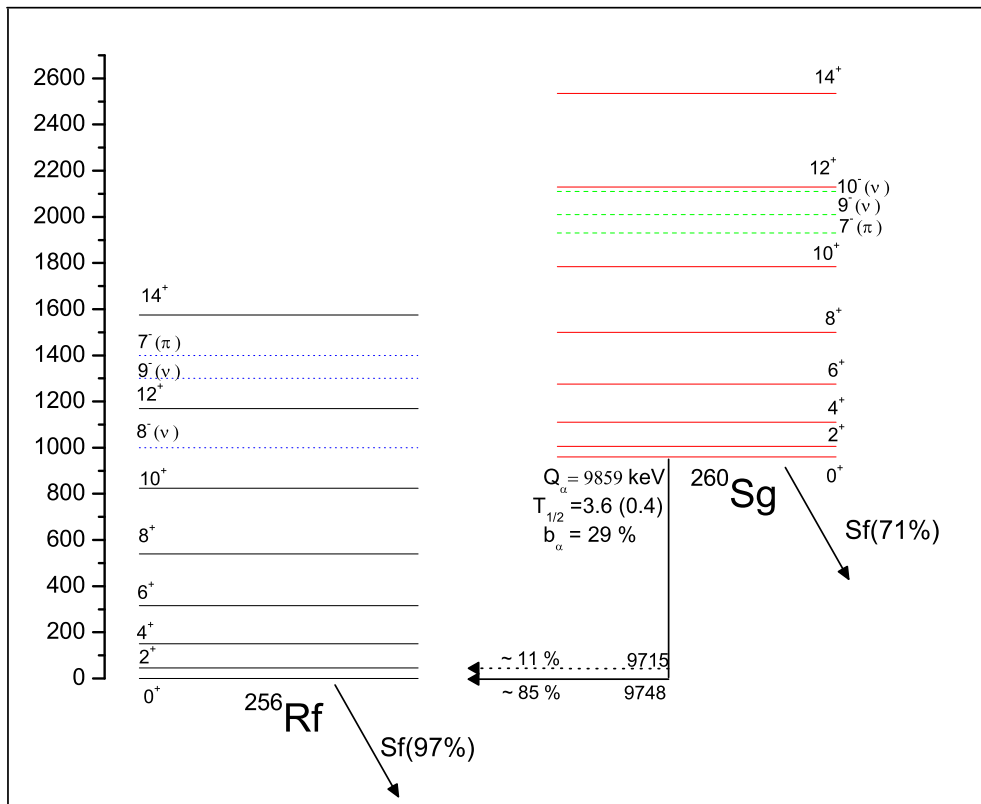
Figure 3.10: Deduced level scheme of ^{260}Sg and ^{256}Rf. The rotational levels are calculated using the WKB method, the half-life and branching ratio of the ground state are experimental results. The dashed line represents the calculated excitation energies for two quasi particle states in ^{260}Sg and ^{256}Rf.

dimensional plot of the logarithm of the decay time (ln ΔT) versus α energy, as shown in Fig. 3.11 a). The total number of events found at 9.715 MeV constitutes 15% of the total decay of ^{260}Sg, with a contribution of $\approx$ 24 % ($\approx$76 %) from the 0.14 ms (5.4 ms) component. As shown in Fig. 3.11 b), the 9.715 MeV distribution has maxima at two different correlation times, corresponding to a fast ($<$ 1 ms) and a slow (1-100 ms) component. We tentatively assign the slow component to the decay of the ^{260}Sg ground state to the 2^+ state of ^{256}Rf with a branching ratio of $11\pm3.5\%$, which is in a good agreement with the calculated value of 12 % [35]. The
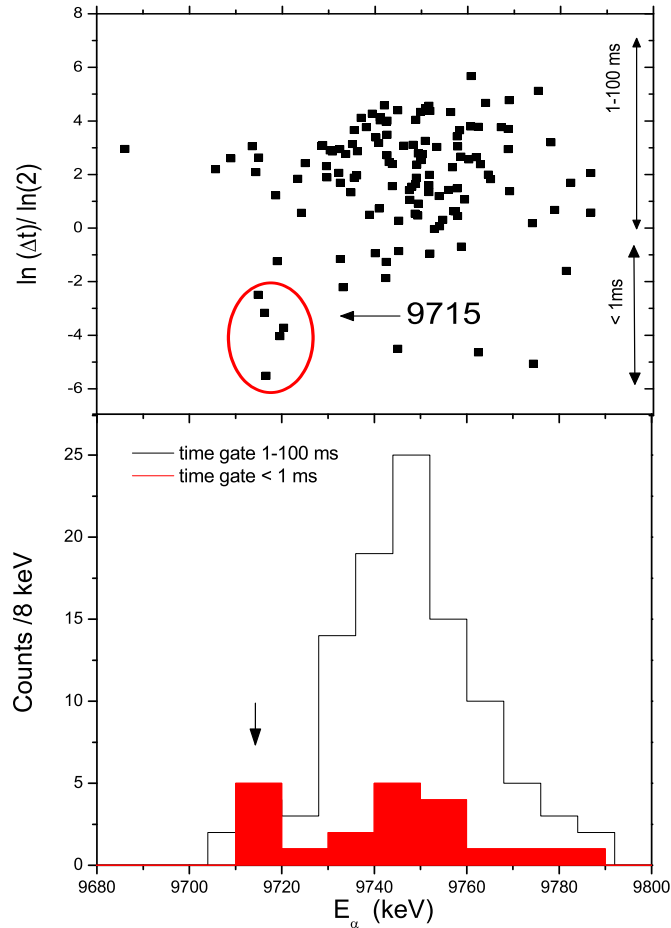
Figure 3.11: a) Plot of $ln(\Delta T)/ln2$ in function of the α particle energy, where ΔT represents the time difference between the alpha particle and an evaporation residue in ms. The shorter lived component of the 9.715 MeV is marked by a circle. b) shows the α spectra obtained with two different time conditions: less then 1 ms (red line) and from 1-100 ms (black line).

fast component probably has a different origin.

In addition, 8 single counts (shown in Fig. 3.9), with time difference between ER and α-decay of 5-11 ms are found in the energy range 9.4-9.7 MeV. We tentatively attribute them to α particles from ^{260}Sg which did not deposit the full energy in the detector. This gives rise to the low energy tail which is a general feature in α-decay

measurements using the implantation method.

3.2.5   Discussion of possible isomerism in ^{260}Sg and ^{256}Rf

In the region of deformed heavy nuclei, K isomers were observed in several nuclei such as ^{270}Ds, ^{266}Hs, ^{250}Fm, ^{254}No, and ^{252}No. In the case of ^{270}Ds, half-lives of 0.1 ms were measured for the ground state and 6.0 ms for the isomeric state with an excitation energy of 1.13 MeV [36]. This isomer decays by alpha particle emission to the corresponding isomer and to the ground state of ^{266}Hs. Based on theoretical calculations [37], the isomer was interpreted as a two quasi-particle neutron configuration. Two possible configurations, $\{\nu\,[613]_{7/2+} \otimes \nu\,[725]_{9/2-}\}_{9-}$ at 1.31 MeV and $\{\nu\,[725]_{11/2-} \otimes \nu\,[615]_{9/2+}\}_{10-}$ at 1.34 MeV, are suggested. On the basis of calculations by Xu et al. [1], isomeric states were expected also to exist in ^{260}Sg.

Figure 3.12: Single particle energies for ^{260}Sg (MeV) for neutrons (right) and protons (left) calculated along axial deformation. Fermi energies are shown as thick dashed lines. Dashed and solid lines are for $\pi = -$ and $\pi = +$ levels, respectively. The upper panels show the Potential energy (PES), to see where the minimum energy is located [38].
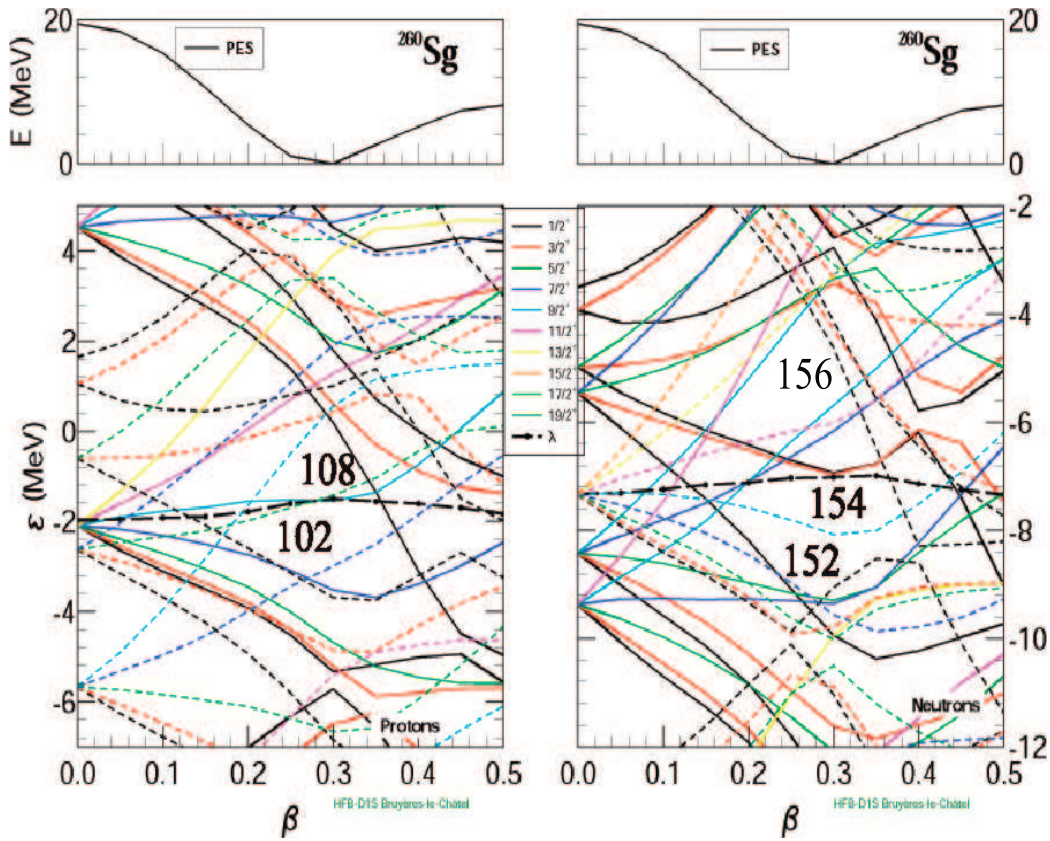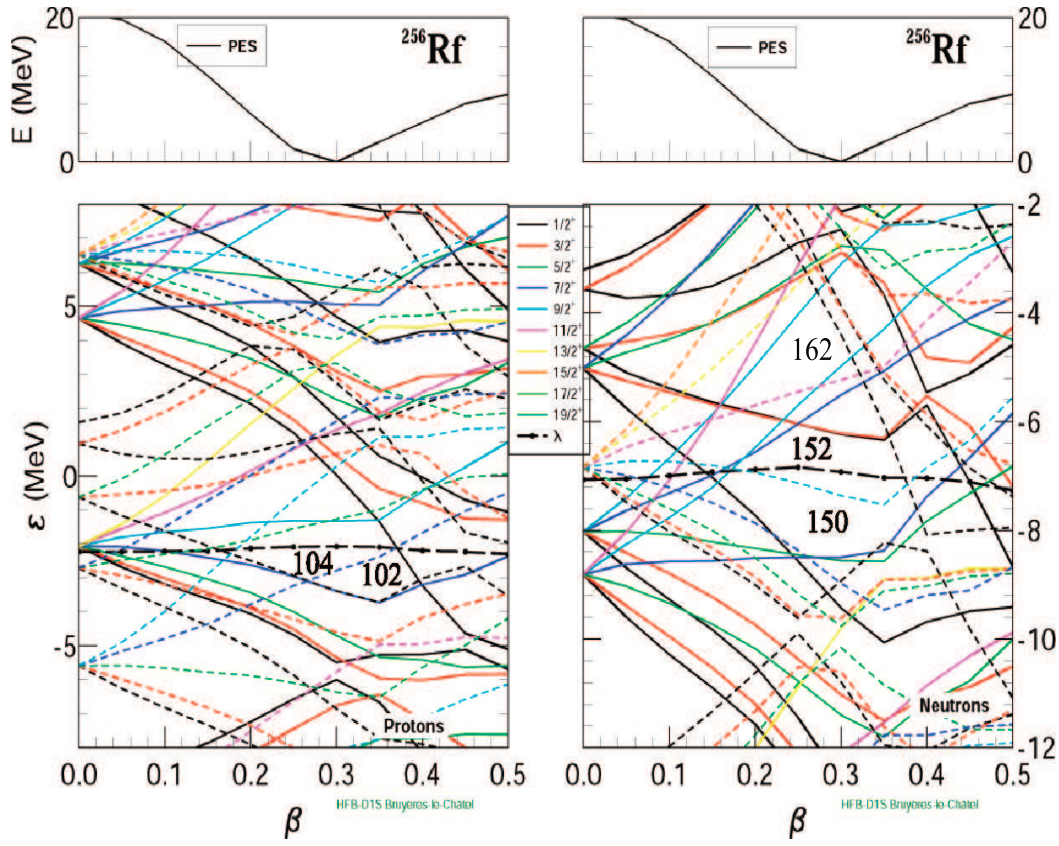
Figure 3.13: Single particle energies for ^{256}Rf (MeV) for neutrons (right) and protons (left) calculated along axial deformation. Fermi energies are shown as thick dashed lines. Dashed and solid lines are for $\pi = -$ and $\pi = +$ levels, respectively. The upper panels show the Potential energy (PES), to see where the minimum energy is located [38].

Single particle energies for ^{260}Sg and for ^{256}Rf were obtained by Delaroche et al. [38] using a Gogny D1S force together with the constrained Hartree Fock Bogoliubov mean field method. The single-particle (neutron and proton) energies deduced from HFB calculations as function of the axial deformation are displayed in Fig. 3.12 and 3.13. The Fermi energies are marked as thick dashed curves for both neutrons and protons. Using this result, two deformed shell gaps appear in the proton system at Z=102 and 108 and two well deformed subshells in the neutron system at N=152/154 and 162. The presence of a deformed gap was experimentally confirmed at N=152 by a minimum in the Q_α-values and enhanced stability for sf at N=152 below Z=104. According to this calculation, for nuclei like ^{256}Rf, where the Fermi level is located within the gap (see Fig. 3.13), K isomers can be formed by raising one or two

particles to levels above the gap. In this case, only high energy K isomers at >1.8 MeV can be formed. Further, in the case of ^{254}No [3], which is the isotone of ^{256}Rf, the observed isomeric state is attributed to a two proton configuration with spin and parity $K^\pi = 8^-$. Thus, we conclude, that also the lowest high spin K isomer in ^{256}Rf should be formed from a two proton configuration due to the gap present at N=152. In ^{260}Sg however, we expect at similar excitation energies both types of K isomers to be formed by proton or neutron quasiparticles with spin and parity of 8^- or 9^- due to the absence of the big shell gap.

In the following, we will discuss the possible decays for ^{260m}Sg. Like in the case of ^{270m}Ds, we could expect an α-decay from ^{260m}Sg to ^{256m}Rf followed by delayed γ-radiations, from the de-excitation of ^{256m}Rf. The α energy of the transition depends on the location of the isomeric states in ^{260}Sg and ^{256}Rf:

- if $E^*(^{256m}Rf) > E^*(^{260m}Sg)$, then $Q_\alpha(^{260m}Sg \rightarrow {}^{256m}Rf) < Q_\alpha(^{260}Rf \rightarrow {}^{256}Rf)$ we would expect an α energy less then 9.7 MeV

- if $E^*(^{256m}Rf) < E^*(^{260m}Sg)$, then $Q_\alpha(^{260m}Sg \rightarrow {}^{256m}Rf) > Q_\alpha(^{260}Rf \rightarrow {}^{256}Rf)$ we would expect an α energy higher then the ground state to ground state transition

In both cases, however, besides ground state decays of ^{260}Sg, we do not observe any statistically significant structure in the spectrum in Fig. 3.9. Taking into account the few background events, we obtain a cross section limit for the α-decay of ^{260m}Sg of 10 pb which corresponds to an α population ratio between isomeric and ground state of < 0.7 %. This value is considerably lower compared to the known nuclei (i.e. ^{250}Fm, ^{254,252}No, ^{270}Ds) in this region, which reveal population ratios between 30-50 %. The only activity that cannot be ascribed to the ground state-ground state decay is the small contribution at 9.715 MeV with a lifetime of 0.14 ms (0.10 ms half-life). Assuming Z=106 as origin, we obtain a theoretical α-half-live of 10 ms, which results in a hindrance factor of 0.01; a hindrance factor below 1 is however unphysical. In other words, if the concentration at low correlation times in Fig. 3.11 is not an artefact it cannot be attributed to the decay of a nucleus with Z=106.

A second possibility would be a γ-decay of ^{260m}Sg to ^{260}Sg followed by an α-decay to ^{256}Rf or by sf. No delayed γ rays were observed from $ER - \gamma - \alpha$ correlations for ^{260}Sg. However, even if an isomeric state would exist, due to the low number of decays of ^{260}Sg and the low detector efficiency at high γ energies, possibly no γ

transitions would have been detected; moreover, low energy transitions are strongly converted and only X rays could be seen.

Additionally, no statistically significant component with a different lifetime from the ^{260}Sg ground state was observed in ER-sf correlations, see Fig. 3.7.

A further reason for the non observability of a K isomer at < 9.7 MeV in ^{260}Sg could be a half-life of the isomeric state smaller than the time of flight through the SHIP separator ($T_{1/2} < 1\mu$s) or dead time of DAQ ($\sim$20 μs). In this case, the isomer would decay before reaching the detector.

Chapter 4

Experimental Results: ^{252}No

4.1 Experimental details

^{252}No was produced in the reaction ^{206}Pb(^{48}Ca,2n)^{252}No in two separate experiments. The first one was performed from 3.6.2005 to 4.6.2005 (part 1) and the second one from 31.3.2006 to 4.4.2006 (part 2). The ^{48}Ca beam was provided by the ECR source. A maximum beam intensity of 1383 pnA on the target was reached. Beam and target parameters are summarized in the table 4.1.

	part1	part2
Beam material	$^{48}Ca^{10+}$	$^{48}Ca^{7+}$
Beam energy	4.598 × A MeV	4.60, 4.55, 4.51 × A MeV
Typical	1.05 pμA	0.89 pμA
Time beam on target	1.3 d	4.2 d
Target material	^{206}PbS	^{206}PbS
Target thickness	$452\mu g/cm^2$	$452\mu g/cm^2$
Total beam dose	$1.3 \cdot 10^{18}$	$2.5 \cdot 10^{18}$

Table 4.1: Beam and target parameters for the synthesis of ^{252}No in two different experiments.
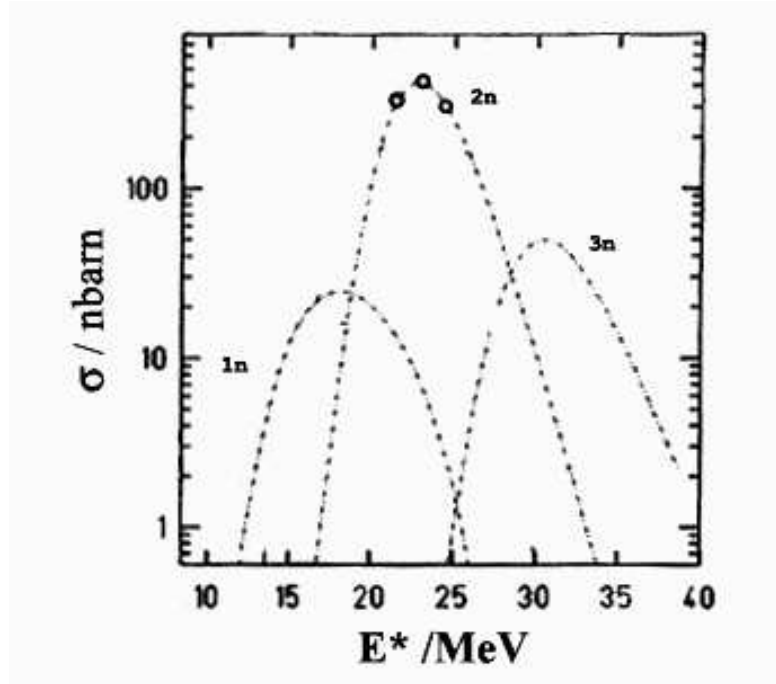
Figure 4.1: Measured cross section for the reaction ^{206}Pb(^{48}Ca, 2n)^{252}No as function of the excitation energy of the compound nucleus (black circles). The dashed lines are calculations with the statistical fusion evaporation code HIVAP [44].

4.2   Excitation function

Production cross section studies for the 2n evaporation channel in the reaction ^{48}Ca $+^{206}$Pb were carried out employing three bombarding energies from 4.51×A MeV to 4.60×A MeV, corresponding to excitation energies of 21.4 MeV, 22.9 MeV and 24.9 MeV. The corresponding cross sections are listed in the table 4.2. In Fig. 4.1 the measured cross sections for the 2n evaporation channel as function of the excitation energy are marked by circles. The HIVAP calculation for the 2n channel is in good agreement with the experimental results. The Bass model barrier B_{int} is 176 MeV in the center of mass frame as calculated according to Bass et al. [39].

Reaction	$E_{lab}/AMeV$	E^* [MeV]	σ (2n) [nb]
^{48}Ca + ^{206}Pb	4.51	21.4	358± 11
	4.55	22.9	426± 2
	4.60	24.9	304± 4

Table 4.2: Production cross sections at given bombarding and excitation energies measured for the reaction ^{48}Ca + ^{206}Pb. The excitation energy is calculated in the center of the target. E_{lab} is the beam energy before the target. The error bars include only statistical uncertainties.

4.3 Isomer spectroscopy of ^{252m}No

4.3.1 Identification of ^{252m}No

In the focal plane of SHIP an isomeric state with a half-life of $T_{1/2}$=100 ms was for the first time identified by delayed coincidences of $ER-(CE,\gamma)-\alpha, sf(^{252}$No). We found that the isomeric state mainly decays to the ground state rotational band via an intermediate band through high energy transitions. The investigation was carried out searching in a first step for γ rays emitted during the lifetime of ^{252}No up to a maximum period of 1 s after implantation, applying the additional condition that the γ rays are in coincidence with conversion electrons. A γ spectrum obtained in this way is shown in Fig. 4.2 a). The same lines are still visible in the spectra b) and c) where we require an α or sf following the γ emission. In total, nine γ lines were assigned to the decay of ^{252m}No.

The experimental γ energies and the number of counts found for each transition are listed in the upper part of table 4.3 together with the K and L X-rays from the isotope ^{252}No. For comparison, also theoretically calculated relative intensities are listed [34]. Since the individual energies in the case of L-X rays are not well separated due to the insufficient energy resolution of the Clover detector at γ energies below $\simeq$ 40 keV, we considered the arithmetic mean weight. From the comparison it can be concluded that the K X-ray energies calculated for this element agree fairly well with the measured ones within ±0.4 keV. As the ratio $I_{K\alpha1}/I_{K\alpha2}$ is constant for given Z, the observed value of 3.50 ±0.87 agrees with the theoretical intensity ratio of 1.5 only within the 2.3 σ interval of the experimentally derived ratio. This could lead to the assumption that these peaks are not only related to X rays but also to some other transitions. The strong intensities of L X-rays suggest the influence of internal
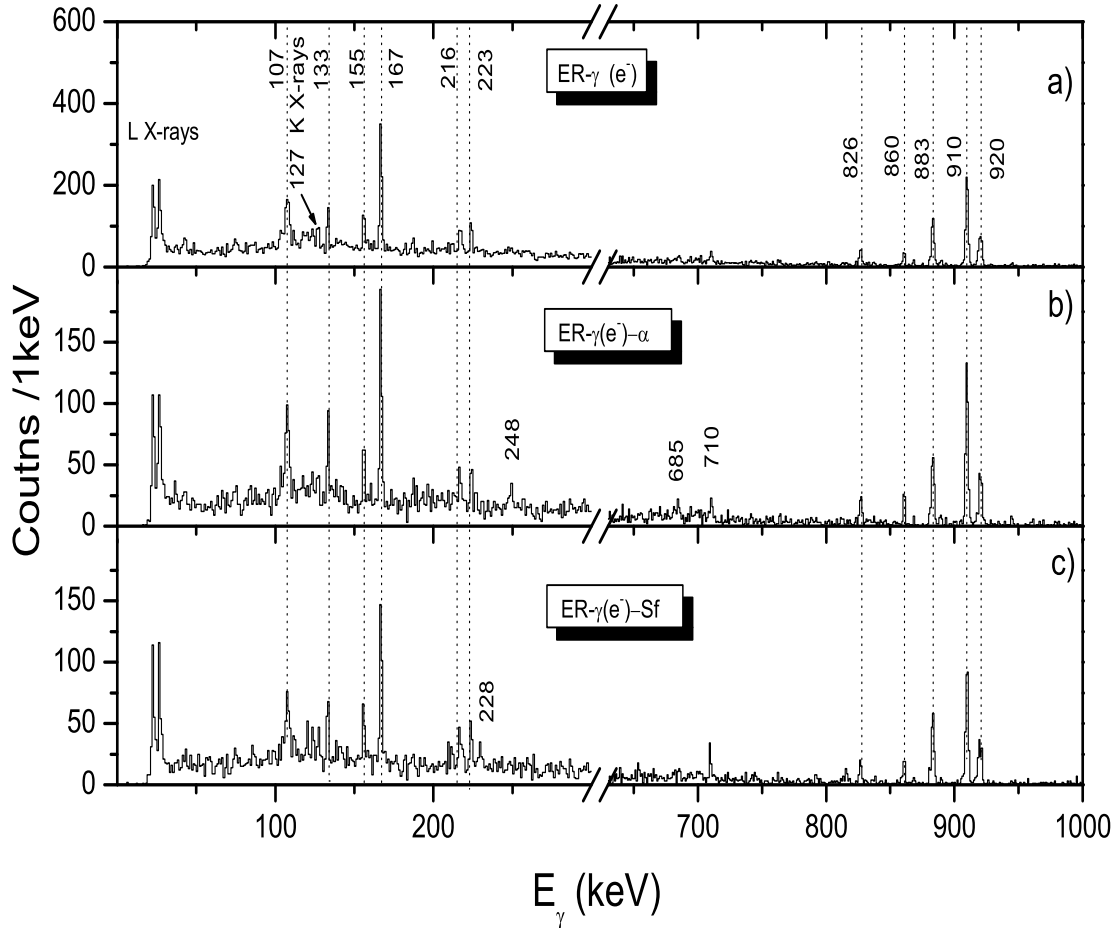
Figure 4.2: a) Gamma spectrum observed in prompt coincidence with conversion electrons ($E_{e^-} < 750$ keV) preceded by an evaporation residue (ΔT (ER-γ) < 1s). b) Gamma spectrum as a) but with the requirement of an α decay within 10 s after the implantation of the ER. c) Gamma spectrum as a) in delayed coincidences with sf within 10 s after the implantation.

conversion in the decay of ^{252m}No to the ground state. This consideration together with the observation of only a few X-ray events brings to the conclusion that the high energy transition decays mainly to the first excited levels of the ground state whose separation energy is much less then the K shell binding energy for element 102 which is 149.3 keV.

E_γ [keV]	$T_{1/2}[ms]$	N_{exp}
920	137 (12)	227
910	146 (8)	488
883	151 (7)	268
860	168 (39)	75
826	139 (18)	106
710	130 (14)	70
685	167 (23)	50
224	176 (19)	125
216	300 (19)	120
167	157 (10)	452
155	127 (11)	175
133	127 (11)	108
107	98 (10)	544

X-ray	E_{Theo} [keV]	i_{Theo} %	E_{Exp} [keV]	N_{Exp}
$K_{\alpha 1}$	127.3	44	127.5	69
$K_{\alpha 2}$	120.953	29	120.5	20
$K_{\beta 1}$	143.506	10		
$K_{\beta 2}$	147	4		
$\sum L_\beta$	22.78	19	22.5	240
$\sum L_\gamma$	27.2	3.8	26.5	297

Table 4.3: Upper part: summary of γ lines of the de-exciting levels with related half-lives and number of counts observed for each energy. Lower part: experimentally found K and L X-rays from ^{252m}No. Theoretical X ray energies and intensities are also listed for comparison. In the case of L_β and L_γ X-rays, the weighted arithmetic mean is used.

The Fig. 4.3 shows the time distribution of γ rays following recoil implantation; a correlation time of 1 s was selected. A half-life of (100 ± 3) ms (lifetime of (144 ± 5) ms) is determined for the isomer of this isotope. In addition, a short lived component was observed with a lifetime of (1.33 ± 0.17) ms which corresponds to a half-life of (900 ± 117) μs. The gamma spectrum observed in coincidence with the short lived component is shown in Fig. 4.4. These γ lines could be interpreted as de-excitation of the isomeric state in ^{253}No. Infect, ^{253}No could be produced as 2n evaporation channel from the contamination of ^{207}Pb in our ^{206}Pb target. Therefore, in table 4.4
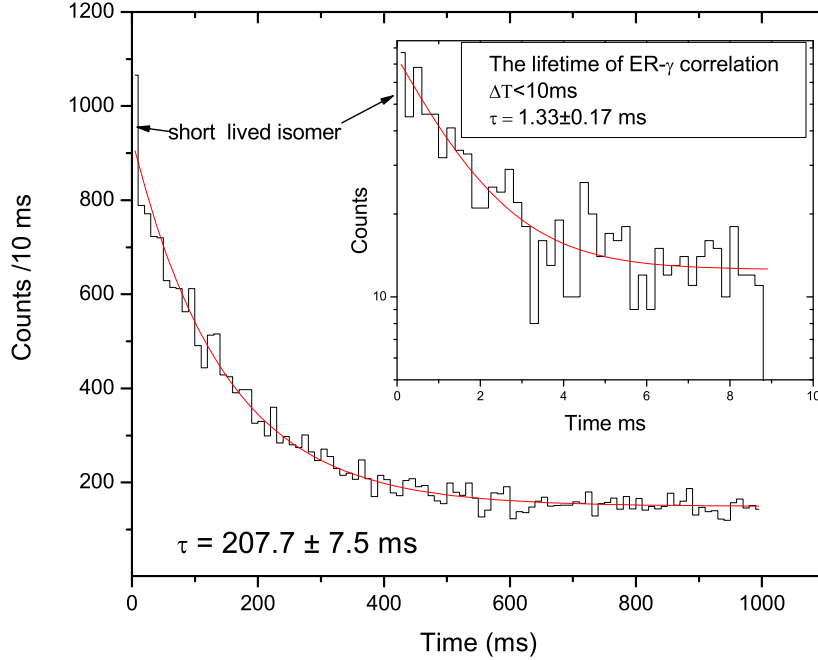
Figure 4.3: Time distribution of γ rays following ER implantations within 1 s. In the embedded figure the time distribution of the short lived isomer with $\Delta T(ER - \gamma) < 10$ ms is shown.

we compare the delayed γ rays found within 3 ms from the ER in the present data with γ lines observed in the ^{253}No experiment [40]. ^{253m}No was discovered in part 2 in an irradiation of 30 hours of ^{207}Pb with ^{48}Ca. This experiment was performed after the irradiation of ^{206}Pb using the identical set up to synthesize ^{252}No. The lines at 127 and 120 keV correspond to the K X-rays of No and the ratio of the relative intensities of 2.0 ± 0.7 agrees within the error bar with the theoretical value of 1.5. Although the energy of the γ transitions and the half-life (668 ± 24) μs agree quite well with the half life found in our case (921 ± 118) μs, some discrepancy could not be explained by the contamination of ^{253}No. For example, the transition at 714 keV that is very strong in ^{253m}No is not present in our spectra. Moreover, the intensity ratio between the lines at 210 keV and 802 keV is 0.3 in the case of the ^{253m}No experiment which is not inline with 1.3 found in this experiment. This could be a hint of the presence of an isomer with short half-life in ^{252}No.

E_γ kev	N_{counts} ^{252}No exp	N_{counts} ^{253}No exp
120 ($K_{\alpha2}$)	12	84
127 ($K_{\alpha1}$)	24	121
109	10	58
188	8	42
210	17	134
613	7	32
714		124
802	13	395

Table 4.4: Comparison of the energy and intensity of the delayed γ lines found in coincidence with ER within $\Delta T < 3$ ms in the present data together with the γ rays observed in the ^{253}No experiment [40].

4.3.2 Level assignment of ^{252m}No

The starting point for our understanding of the decay of ^{252m}No were the gamma-gamma coincidences. This method permits the identification of transitions belonging to the same cascade.

The high energy transitions at 910 keV, 920 keV and 883 keV, visible in the spectrum 4.2, were also observed at in beam studies by Leppänen et al. [41]. This indicates that those γ lines do not stem from the isomeric level itself, but from a level populated by the decay of the isomeric level. Thus, we can affirm that the isomer decays via an intermediate structure to the ground state rotational band.

The following level assignments have been made on the basis of the ground state rotational band level scheme measured by Herzberg et al. [7](see Fig. 4.5), $\gamma - \gamma$ coincidences and coincidences between γ rays and CE. The suggested level scheme is shown in Fig. 4.6.

The coincidence spectrum (4.7) reveals that the strong line at 910 keV is in coincidence with the 167 and 107 keV line. We observed the same decay pattern for the line at 826 keV, which is also coincident to the 167 and 107 keV line. Therefore, we conclude, that both, the 910 and the 826 keV transitions populate the 6^+ level of the ground state rotational band.

A further support for this assignment is the energy distribution of electrons coincident with the, e.g., 910 keV and 167 keV lines. In the coincidence spectrum
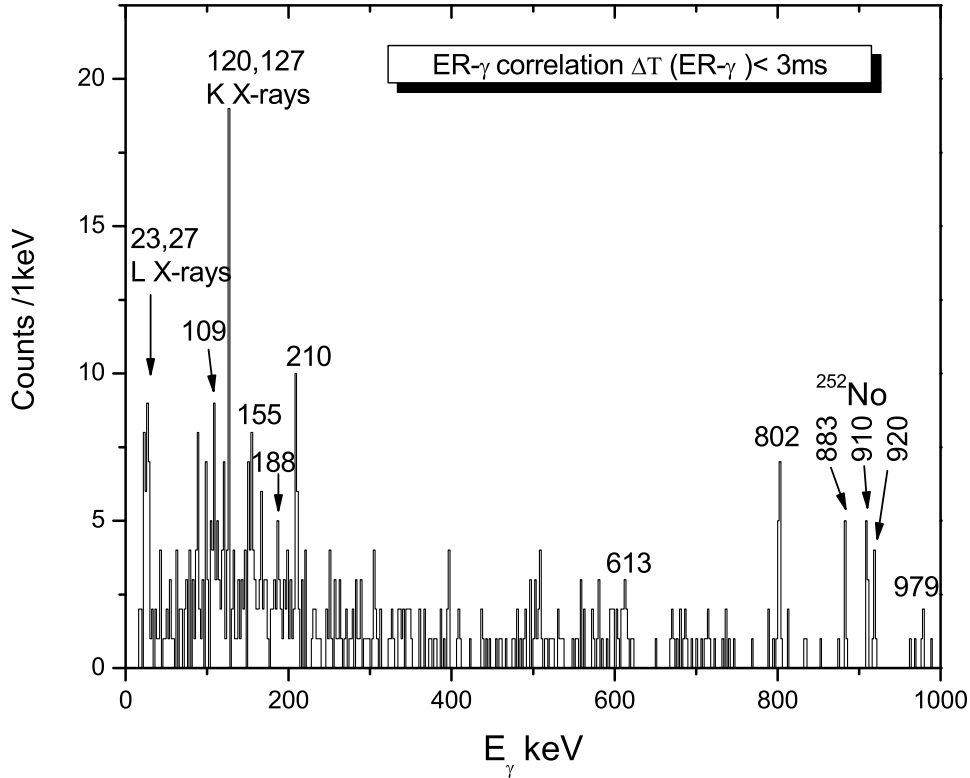
Figure 4.4: Gamma rays following ER implantation within 3 ms.

for the 910 keV line Fig. 4.8 two broad peaks at ∼120 and ∼270 keV can be distinguished.

They are attributed to the sum energy of CE from the de-excitation cascade within the ground state band. The peak at 270 keV is due to the L conversion of all transitions ($6^+ \rightarrow 4^+$, $4^+ \rightarrow 2^+$, $2^+ \rightarrow 0^+$) taking into account that the L binding energy for nobelium is ∼30 keV. The peak at 120 keV occurs if only CE from the $4^+ \rightarrow 2^+$ and $2^+ \rightarrow 0^+$ transitions are summed. The intensity ratio of the two peaks qualitatively can be explained by the different conversion coefficients for the 167 keV ($\alpha_{tot} \sim 3$) and the 107 keV ($\alpha_{tot} \sim 25$) transition and the probability of 50% for an electron to escape out of the detector. A similar electron energy distribution was observed in coincidence with the 167 keV line (Fig. 4.8). It contains only the contribution from the 107 and 46 keV transitions which give the peak at ∼120 keV.

The transition at 920 keV is only in coincidence with the 107 keV line and must therefore feed the 4+ level of the ground state band.
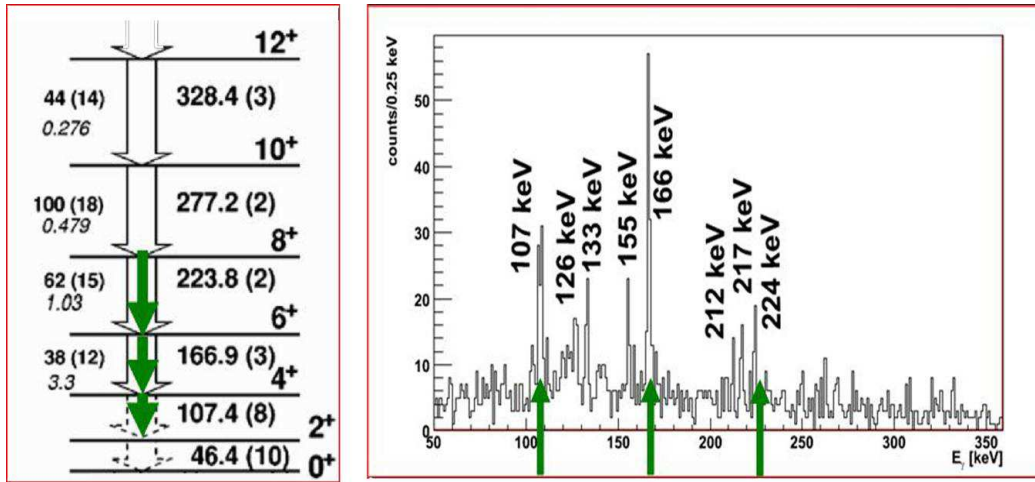
Figure 4.5: Left side: level scheme of the ^{252}No rotational band proposed by R.D.Herzberg [7]. The numbers on the left side of a transition indicate the relative intensity of the γ transition, the number in italics below gives the internal conversion coefficient. The green arrows represent the transitions observed also in our experiment. Right side: γ spectrum from $ER - \gamma$ correlations measured in the present work.

The weak line at 685 keV differs in energy by 224 keV from the 910 keV transition. Therefore it was attributed to the decay into the 8^+ level of the g.s. band, starting from the same level in the intermediate band as the 910 keV transition.

For the gamma lines at 883 and 862 keV, we found no coincident lines from the ground state band. From the missing $\gamma - \gamma$ coincidences with the strong 883 keV transition we conclude, that it leads either to the ground state (0^+) or to the 2^+ level from which no γ emission is observed since it is practically completely converted ($\alpha \approx 900$).

The assignment of spin and parity to the intermediate band levels was made by starting with the intense 910 keV line which leads to the 6^+ level of the g.s. band as discussed above (in our experiment it is not possible to *measure* spin and parity of the levels). We assigned multipolarity E1 to this transition. M1 character can be excluded since in this case, we would expect significant K conversion ($\alpha M1 = 0.2$ and $N_\gamma = 500$) and therefore a clear K X-ray peak at 127 keV in the gamma spectrum. Also E2 character can be excluded, because in this case, the starting level would require spin and parity 8^+ or 4^+. In the case of 8^+, the transition $8^+ \rightarrow 8^+$ (M1 character) should be stronger then the $8^+ \rightarrow 6^+$ E2 transition. The 685 keV line would then correspond to the $8^+ \rightarrow 8^+$ transition and should have
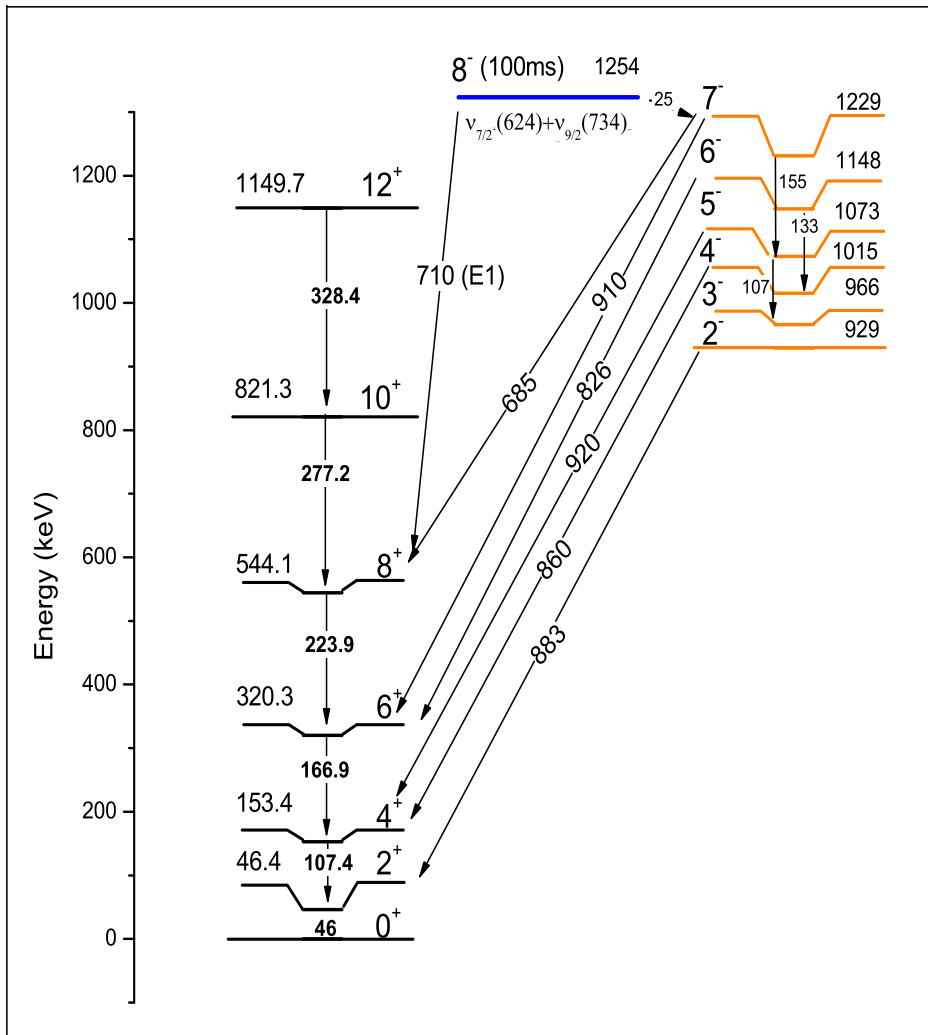
Figure 4.6: Level scheme suggested for ^{252}No.

higher intensity then the 910 keV line. If we assume 4^+ as starting level, we should observe an additional peak at $(910+167)$ keV= 1077 keV, which would correspond to the $4^+ \rightarrow 4^+$ M1 transition. So, most likely E1 is the multipolarity of this transition and spin and parity 7^- or 5^- could be assigned to the respective level of the intermediate band. 7^- is preferred because the transition from $7^- \rightarrow 8^+$ is more
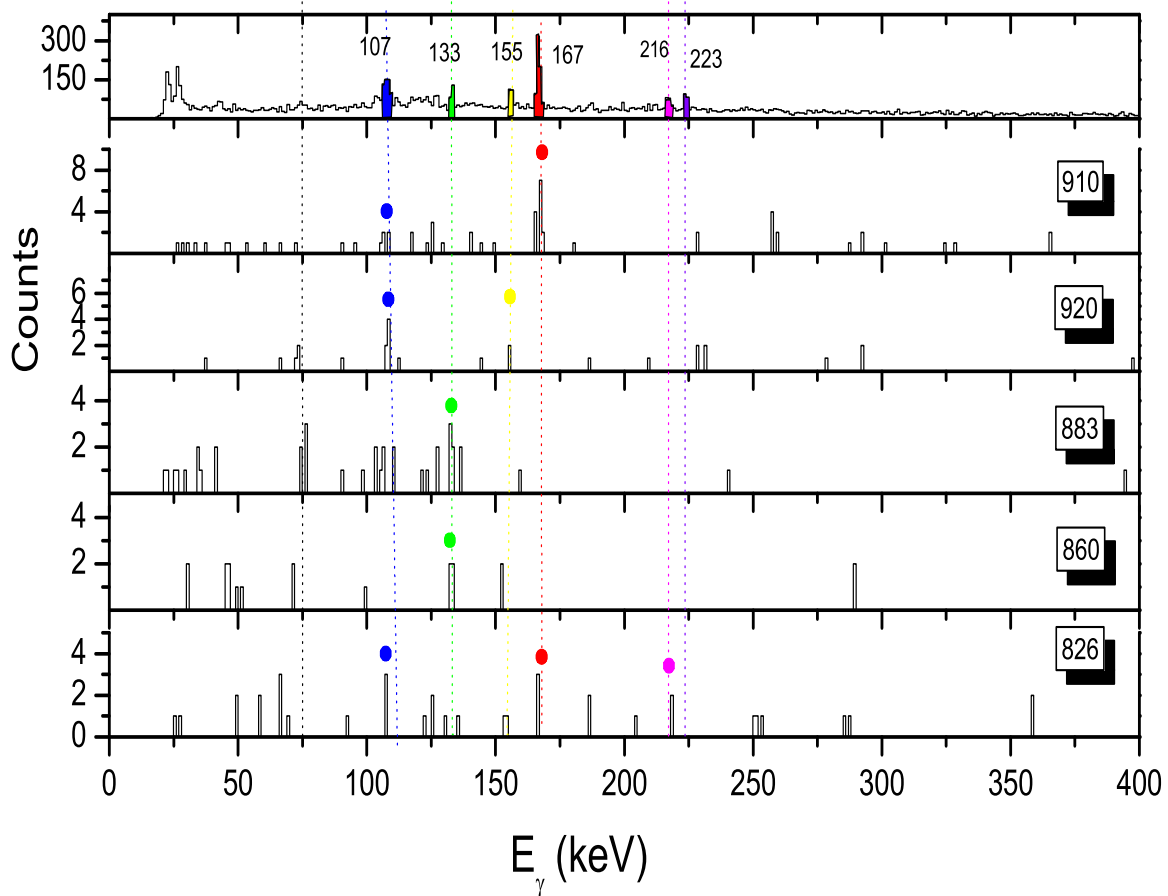
Figure 4.7: The upper figure shows the total γ spectrum taken from ER-γ correlation within 1s of searching time. Following spectra are $\gamma - \gamma$ coincidences with gates on the most intense lines 910, 920, 883, 860 and 826 keV.

likely than $5^- \to 8^+$.

Since the sum energy of the lines at 910 and 167 keV is equal to the sum energy of the lines at 920 and 155 keV, we attributed the 155 keV line (which doesn't belong to the g.s. band) to a 7^- to 5^- transition within the intermediate band.

Due to the identical energy sums (167+826) keV and (133+860) keV the lines at 826 keV and at 860 keV are assigned to decays into the 6^+ and 4^+ level, emitted from levels in the intermediate band that are 133 keV apart. Therefore the corresponding
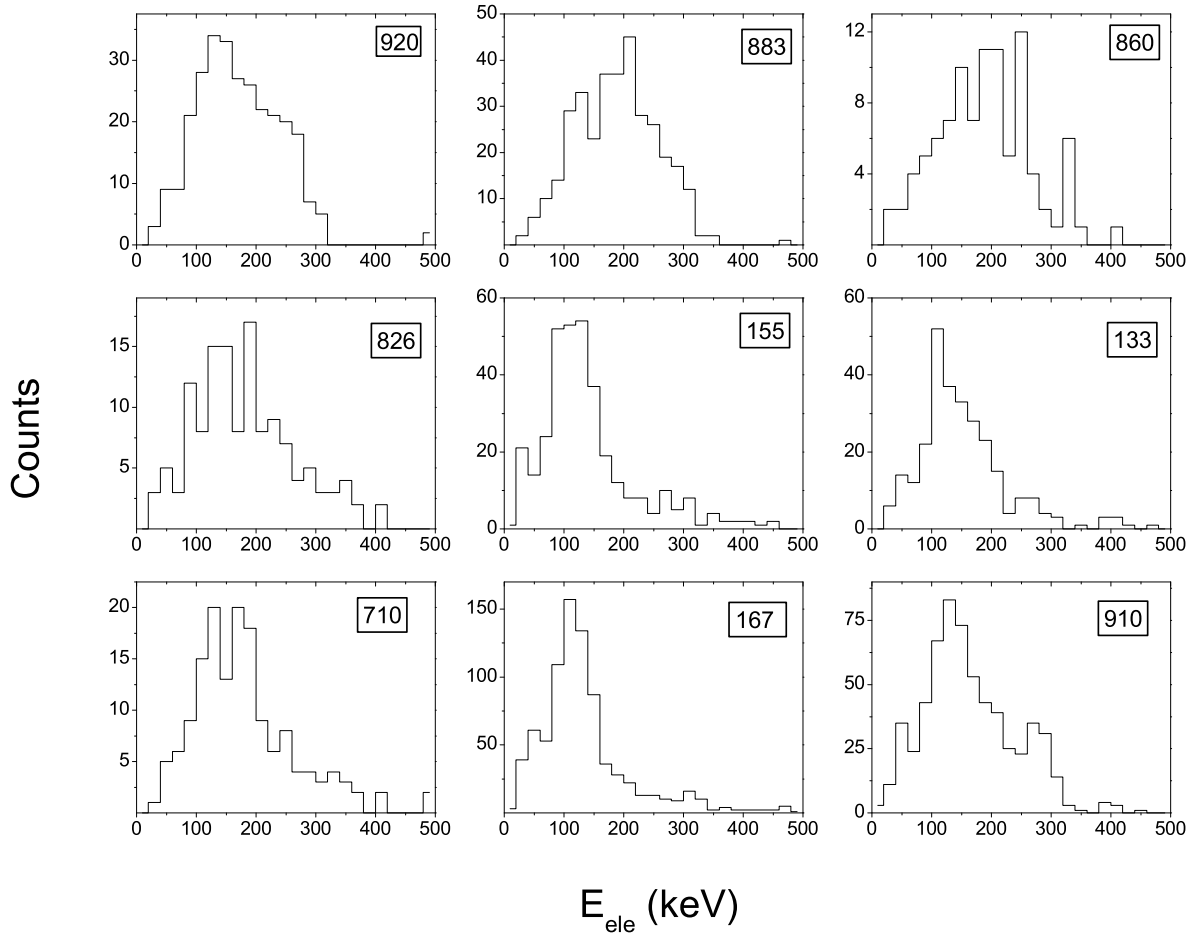
Figure 4.8: Conversion electrons in prompt coincidence with γ-rays.

γ-line (133 keV) is assigned as $6^- \rightarrow 4^-$.

The gamma line at 107 keV shows a slight broadening which indicates the presence of a second component besides the 4^+ to 2^+ 107 keV transition in the g.s. band. We assign this component to the 5^- to 3^- transition within the intermediate band. This energy also fits to the energy systematics, calculated for the rotational band.

As discussed above, the 883 keV transition must lead to some low lying level of the ground state band. However, the CE electron spectrum in coincidence with this line shows a maximum around 200 keV. This shape can be attributed to the sum of CE from several transitions (M1 and E2) within the intermediate band. Therefore we conclude, that the starting level for the 883 keV line is a low lying state in the

intermediate band. Tentatively it is attributed to the transition $2^- \to 2^+$, which is also in accordance with the energy balance within the intermediate band.

The band head we locate at 2^-. This was deduced from the energy level spacings between the successive members of the band using the Bohr Mottelson formula $E_{k+1} - E_k/E_{k+2} - E_k = K + 1/K + 2$ [42]. From the 2^- to 2^+ transition (883 keV) we estimated an excitation energy of the band head of 929 keV.

Similar to the case in the N=150 isotone ^{250}Fm, a direct decay branch leads from the isomeric state to the 8^+ state of the ground state band via the 710 keV transition [66]. This is supported by the shape of the electron spectrum. Another indirect argument is that the intensity of the 685 keV line is only about 25% of the 224 keV line what means that the 8^+ level must be fed also by another level.

From the sum energy of the 8^+ level and the 710 keV transition, we can locate the isomeric state at 1254 keV.

The main decay branch of the isomeric state leads to the 7^- level of the intermediate band with a transition energy of 25 keV, which corresponds to the energy difference between the 710 keV and 685 keV lines. This low decay energy to the intermediate band is consistent with the fact that we did not observe any gamma lines which could be attributed to such a decay.

The most probable spin and parity for the isomer is 8^-, as will be discuss in the following section, which decays to the 8^+ level of the rotational band with an E1 γ transition and to the 7^- state of the intermediate band via an M1 transition.

$J_i \to J_f$	Measured [keV]	Rotational formula [keV]
$3^- \to 2^-$	37.20(1)	37
$4^- \to 3^-$	42.48(15)	49.1
$5^- \to 4^-$	63.58(14)	61.4
$6^- \to 5^-$	74.88(13)	73
$7^- \to 6^-$	85.73(39)	86
$5^- \to 3^-$	107.0(1)	110
$7^- \to 5^-$	155.90(8)	159.7
$6^- \to 4^-$	133(1)	135

Table 4.5: List of transition energies observed for the intermediate band for ^{252}No in comparison with theoretical values calculated according to the rotational formula.

In table 4.5, we compare the transition energies of this band with the one esti-
mated by the formula for a rigid rotor. The static moment of inertia was deduced
experimentally by the energy difference between the band-head and the first ex-
cited level. In order to observe clearly the possible deviation of this band from an
ideal rotational band, we plotted in Fig. 4.9 the excitation energy of the levels vs
$I(I+1) - K^2$.

Level energy measured[keV]	Rotational formula [keV]
929(0.1)	929.198
966(0.1)	965.312
1013(0.1)	1013.464
1073(0.1)	1073.654
1145(0.1)	1145.882
1229(0.1)	1230.148
	1326
	1434,79
	1555
	1687.592

Table 4.6: List of level energies observed for the intermediate band for ^{252}No in comparison
with theoretical values calculated according rotational formula.

Over the years, some phenomenological models have been introduced to char-
acterize the properties of rotational bands and it was found that the spectra often
follow exactly the I(I+1) law along the Yrast line with the moment of inertia of a
rigid rotor. Our results indicate a linear dependence of the level energies on the
angular momenutm (Fig. 4.9). It means that the $K^\pi = 2^-$ band has the behavior
of a perfect rotor at low spin. To extrapolate the higher members of the band,
we performed a linear fit including the known members. We determined the linear
parameter as $B = 917.16$ and $A = 6.019$. Using those values we extrapolated the
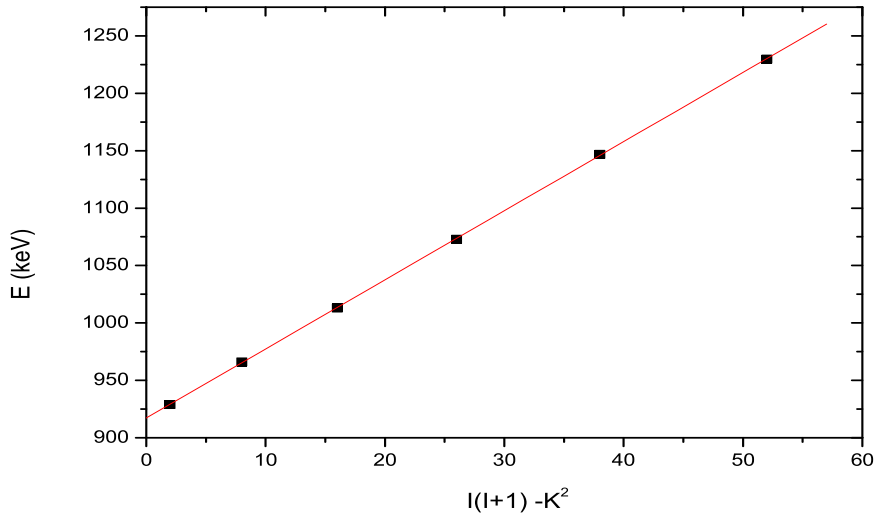unknown members of the band up to 11^-.

Figure 4.9: Energy vs angular momentum. The spectra show how at low spin our rotational band follows the behavior of an ideal rotational spectrum.

4.3.3 Discussion of the K isomer in ^{252}No

The existence of K-isomers in the transactinide region is explained by the breaking of pairs and raising one or 2 particles in orbitals above the Fermi surface. According to the calculations using the Gogny D1S force together with the constrained Hartree-Fock Bogolyubov mean fiel method, two gaps, one small gap of 1 MeV and a larger one of more than 2 MeV, are obtained (at $\beta_2 = 0.25$ deformation) for N=150 and N=152 respectively. For protons, a 1 MeV energy gap is seen for Z=100 at a deformation around $\beta = 0.25$, see Fig. 4.10. The strong presence of K isomers in the No region could be, therefore, explained by the excitation of nucleons to levels above these shell gaps. Two low lying quasi-particle levels around the Fermi surface are predicted to exist in many nuclei [38], [37], as two quasi proton 7^- and two quasi neutron 8^- states.

In Fig. 4.11, the first 2 quasi-particle (qp) excitations for proton and neutron configurations at low excitation energy are shown, from Th to No, without breaking time reversal symmetry. It is seen that the excitation energies for neutrons are at lower energy than for the proton two quasi-particle states.
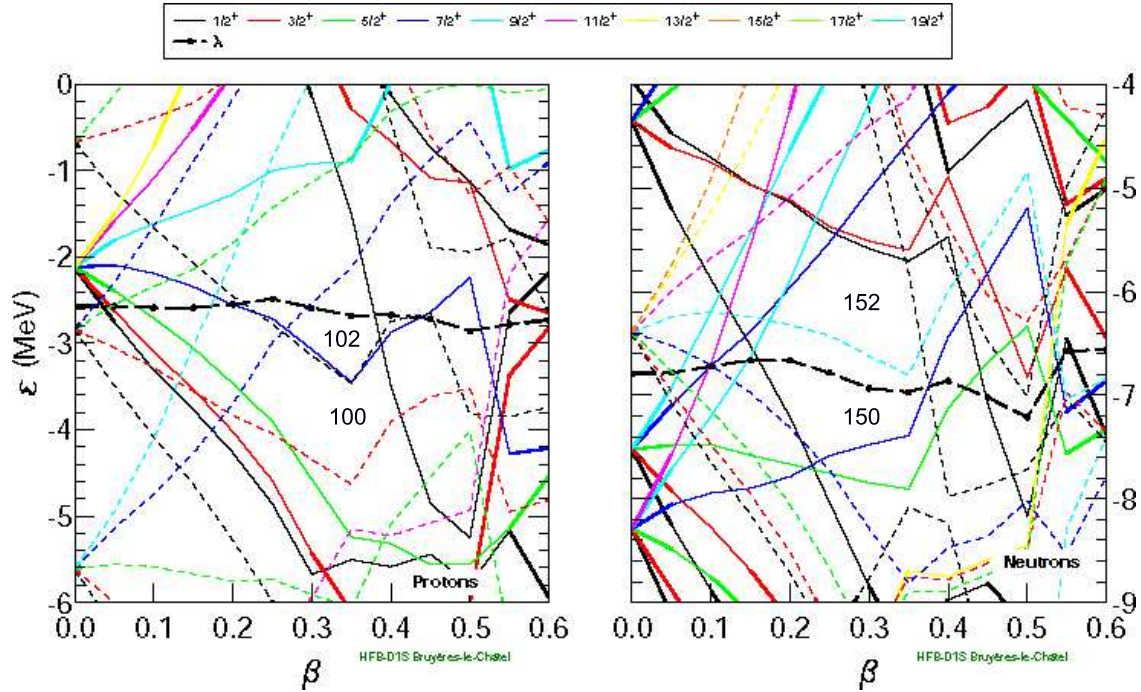
Figure 4.10: Single particle energies for neutrons and protons calculated along axial deformation of ^{252}No. Fermi energies are shown as thick line. Dashed and solid lines are for $\pi = -$ and $\pi = +$ levels, respectively [38].

From theoretical considerations and experimental results (see Fig. 4.12), one expects an 8^- two quasi-neutron configuration as the lowest quasi-particle configuration and thus, this configuration is attributed to ^{252m}No.

Another argument supporting this interpretation is the large hindrance factor of 5.37×10^{10} of the decay. The assumption that the isomer decays from an 8^- state via a M1 transition is in good agreement with the systematics of absolute transition probabilities of K-forbidden γ ray transitions proposed by Löbner et al [50]. This is based on the empirical rule $logF_W = 2(|\Delta K| - \lambda) = 2\nu$ (see Fig. 4.13) where the hindrance factor was calculated on the basis of the Weisskopf estimation.

Finally, we suggest that the high K band isomer in ^{252}No is formed by coupling together the $\nu 7/2^+$ [624] $\otimes$ $9/2^-$ [734] neutron orbital to give $K = \Omega 1 + \Omega 2 = 8$ and negative parity $(\pi_1 * \pi_2)$. Since this transition represents a change in the K quantum number of $\Delta K = 6$, it is strongly hindered which is proven by the long half-life of 100 ms.

Concerning the possible configurations for the intermediate band, we can only
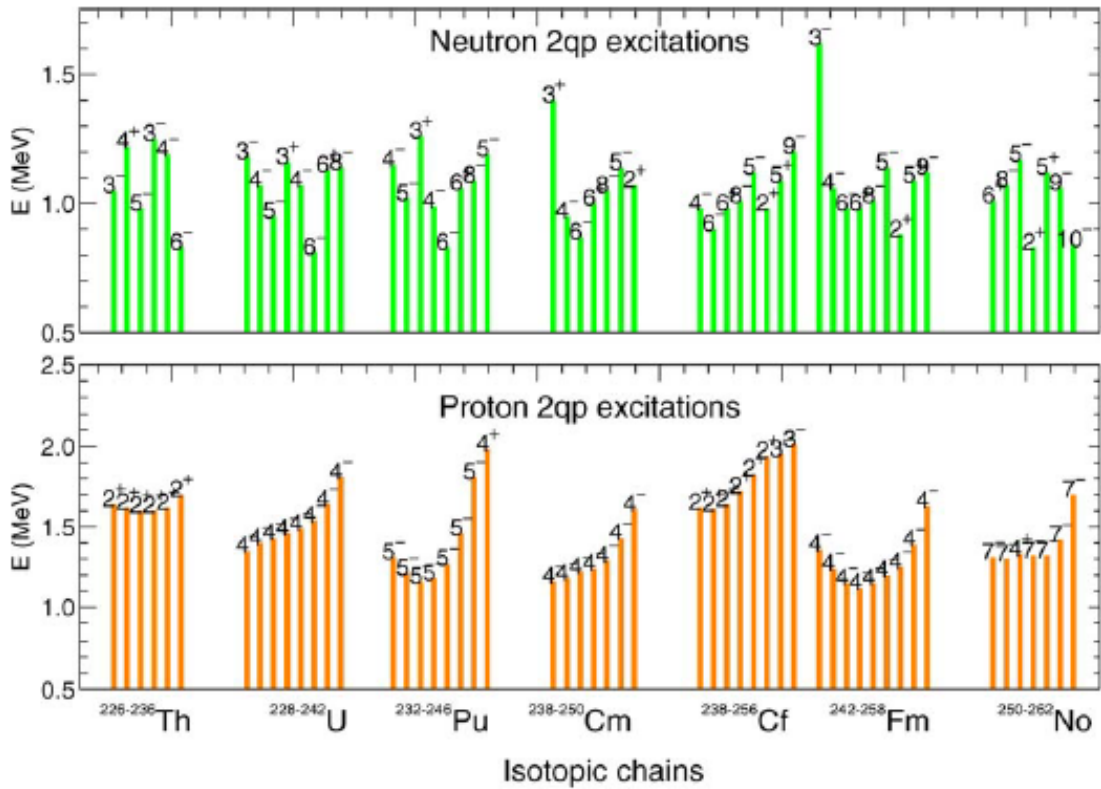
Figure 4.11: Lowest two-quasiparticle excitation energies for neutrons (top panel) and protons (bottom panel) at normal deformation in Th to No isotopes. Predictions are obtained without breaking time-reversal symmetry. States are labelled with parity and K quantum number for each isotope.[38]

rely on the few experimental data available in this region of the nuclear chart. All of them point to the existence of a $K^\pi = 0^-, 1^-, 2^-$ band interpreted as an octupole vibrational state. In the superfluid model of the nucleus, the vibrational states are seen as the superposition of several two quasi-particle states with the same K^π [51].

An octupole band with band-head $K = 2^-$ has been observed in the isotones ^{246}Cm, ^{248}Cf. By comparing the decay pattern of ^{252}No with the one of ^{246}Cm, several similarities have been observed. In both cases, for example, the 2^- state decays by an E1 transition to the 2^+ state. Moreover, the isomeric 8^- state decays to the octupole band via an M1 transition. The theoretical calculation [51] suggests for the octupole band in ^{246}Cm a two neutron state in the configurations
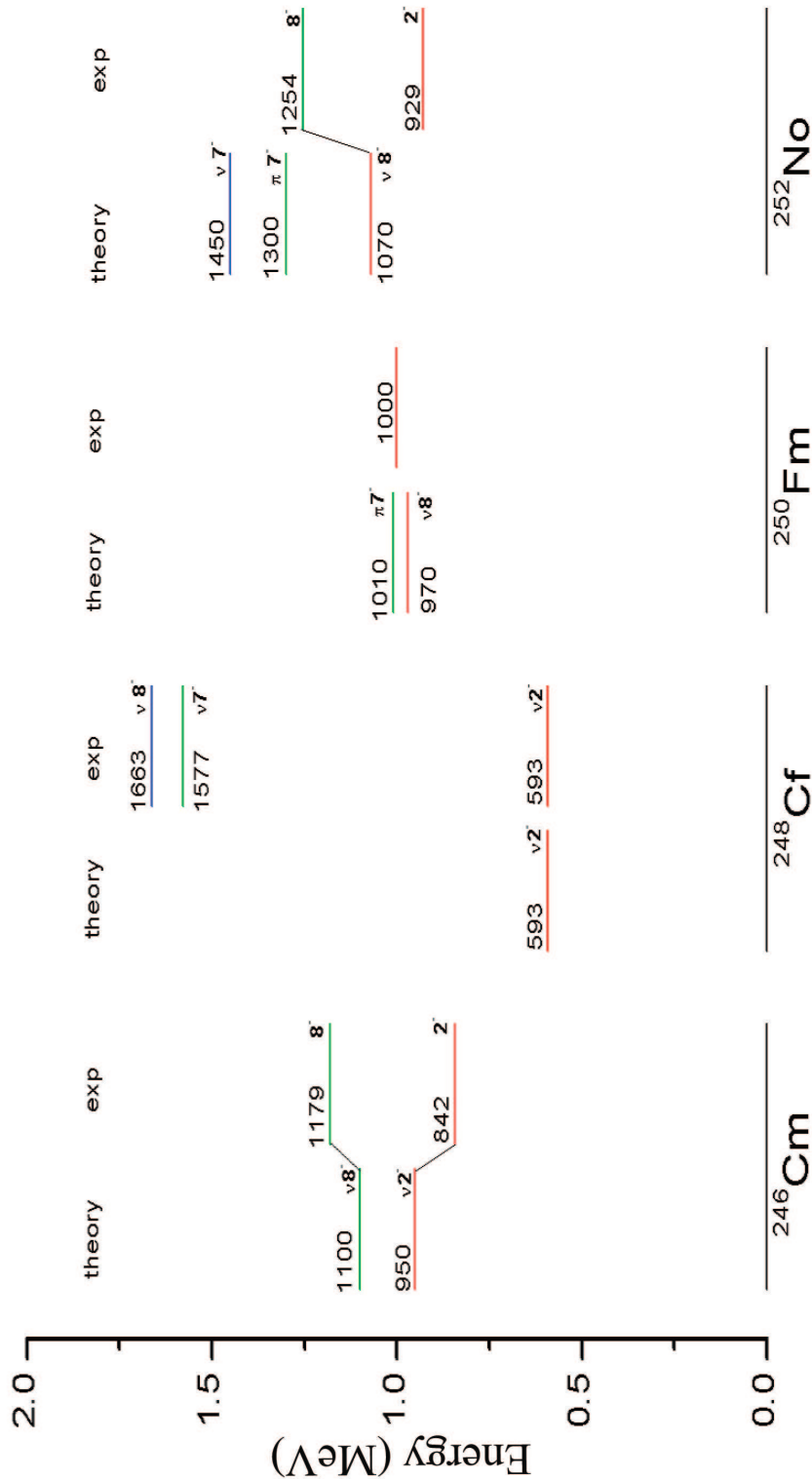
Figure 4.12: Comparison between experimental and theoretical calculations for the 8^- state and for the 2^- state in N=150 isotones. For ^{246}Cm, the experiment was performed by Yates [45] and the theoretical calculation for the 8^- state were done by Soloviev [46], and for the 2^- state by Komov [47] . For ^{248}Cf, the experiment was performed by Yates [48] and the calculation was based on the DWBA model. For ^{250}Fm, the experiment was performed by Ghiorso [2] and the calculation by Xu [1]. For ^{252}No, the experimental results are from the present work and calculations were done by H. Delaroche et al. [38] and F.R. Xu et al. [1].

Figure 4.13: Range of hindrance factors relative to the Weisskopf estimate F_W of electric γ ray transitions for different ΔK. The dashed line shows the dependence of F_w on ΔK for M1 transitions according to the empirical rule proposed by Rusinov [49]. The location in the diagram of ^{252}No is represented by the dot.[50]
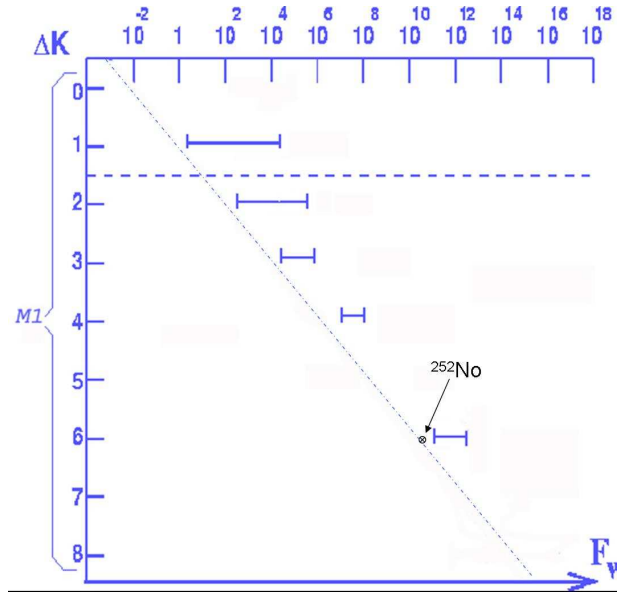
$\nu 5/2^+ [622] \otimes 9/2^- [734]$ (61 %) and $\pi 7/2^+ [633] \otimes 3/2^- [521]$ (31 %) as the principle two quasi-particle component in the K^π octupole vibrational state. Moreover this configuration is particulary favored since it involves the transition of a single neutron from the decay of the 8^- isomeric state to the 2^- state band.

Finally, we can tentatively assign a $K_\pi = 2^-$ state to the band-head in analogy to the situation in the isotone ^{246}Cm.

There are still a number of puzzling features which could not be completely explained in the frame of the discussion on the decay scheme of the isomer. Among others, it is the difficulty to assign the peak at 216 keV with an intensity very similar to the 224 keV line. Moreover, the half-life of the 216 keV line is 300 ms which is significantly higher than the half-life of 224 keV line, what would underline a different origin. It is also difficult to locate inside the level scheme the transitions of low statistics shown in the spectra of Fig. 4.14. A possible explanation could be the decay of the isomer via two different bands which lie close to each other in energy. In fact, in several nuclei, besides the occurrence of the even parity members
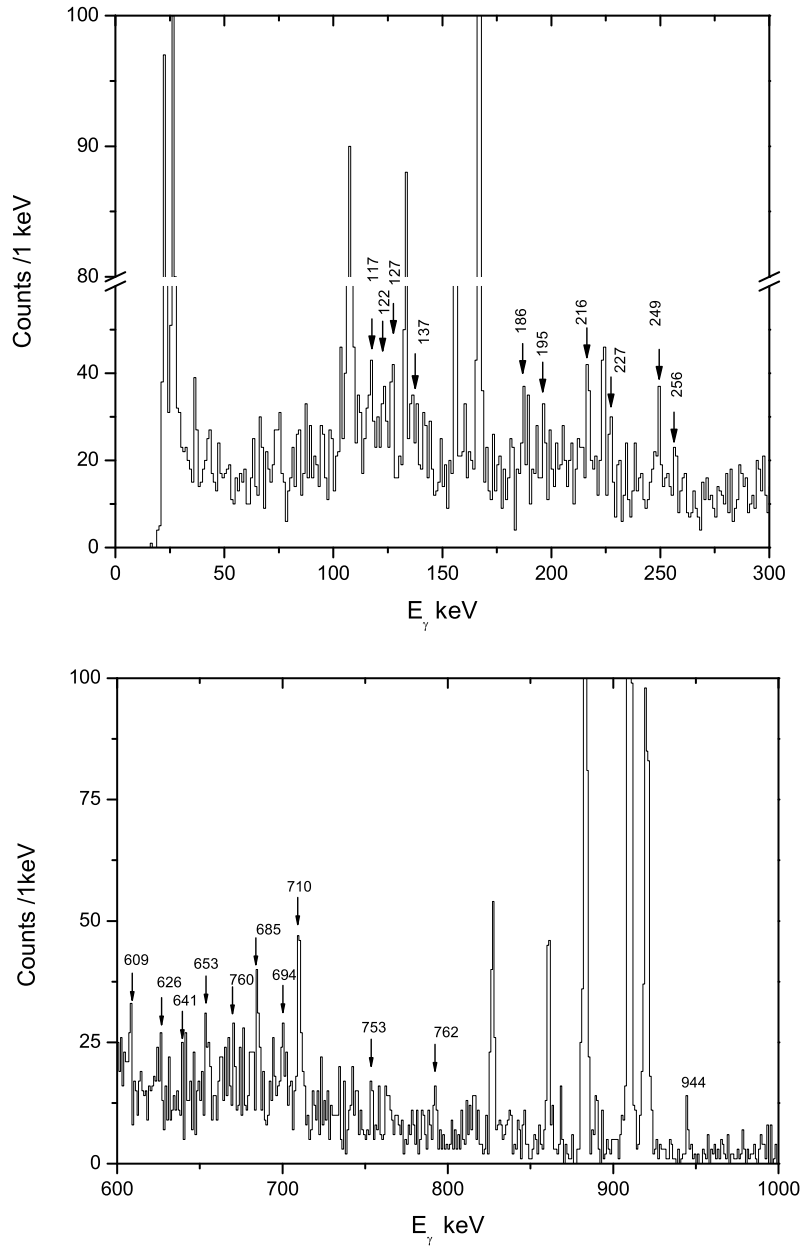
Figure 4.14: Gamma rays in coincidences with CE ($E < 700$ keV) under the condition that the coincident CE-γ pair is preceded by implantation of an ER-like nucleus within $\Delta T < 1s$ and followed by the α decay or Sf of ^{252}No within $\Delta T < 7s$. In the upper spectrum only the gammas from part2 are collected due to the strong contamination at low energy of Pu and Np X-rays present in the part1; in the lower part, both parts are summed up.

of the ground state rotational band, a low lying state of negative parity and spin 1 has been observed. These negative parity states, observed in many even even nuclei like ^{228,230}Th, ^{224,226}Ra, and ^{232}U, are shifted upwards with respect to the positive parity states. This effect is denoted as "parity splitting".

Figure 4.15: A_1, Z_1 denote the heavy cluster, A_2, Z_2 is the light cluster e.g. α particle. $\theta_0\phi_0$ is the orientation of the dinuclear system with respect to the space fixed system, $\theta 1$ $\phi 1$ is the orientation of the deformed fragment with respect to the space-fixed system.

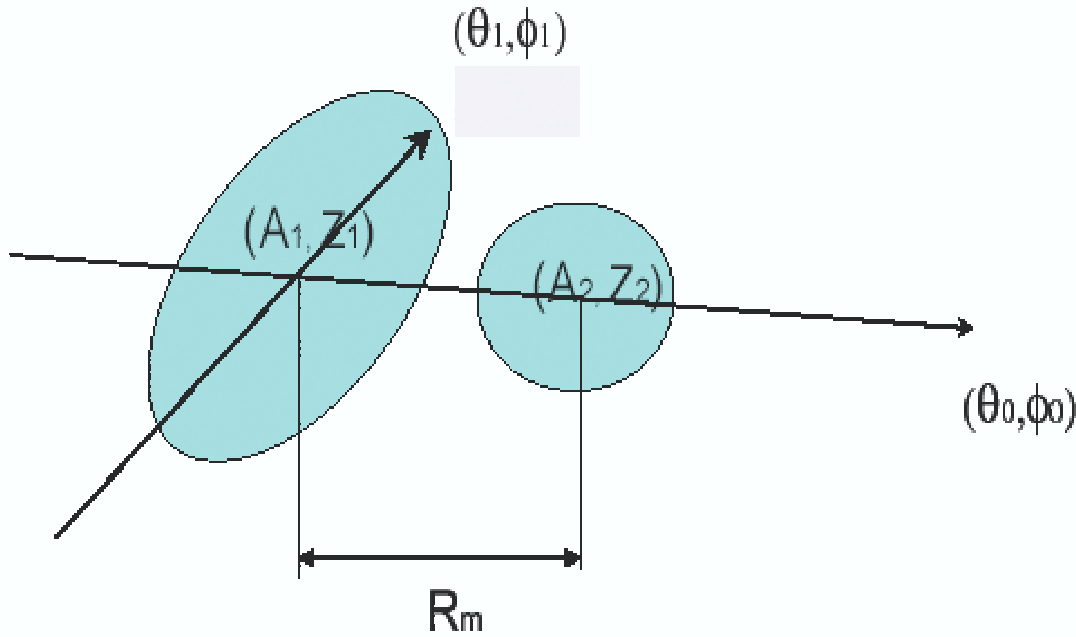The existence of the 1^- state is explained in terms of an octupole vibrational deformation when the spheroidal symmetry of the nucleus is broken. Extensive studies were carried out by T.M. Shneidman et al. [52] who predict for the first time in heaviest nuclei the existence of low lying states with parity opposite to the parity of the ground state band. The model is based on the idea that the total wave function of the nucleus can be assumed as a superposition of different dinuclear systems (DNS) and the mononucleus. The DNS or nuclear molecule is a system of a light cluster like α particle or Li and a heavy cluster assumed to be deformed and to rotate, see Fig. 4.15. In this frame, the source of the octupole deformation, responsible for the presence of the 0^- band, is attributed to the motion of the nuclear system in the mass asymmetry coordinate. According to this interpretation, one might expect to see a rotational band of levels $1^-, 3^-, 5^-$.. with a spacing following

the I(I+1) law and with a moment of inertia equal to a mean value between the moment of inertia of the mononucleus and that of the cluster configuration.

The result of these calculations for ^{252}No adjusted to the experimental data of the present work is shown in the Fig. 4.16. Thus, we can tentatively attribute the line at 216 keV to the transition $5^{-}_{K=1^{-}} \rightarrow 5^{-}_{K=0^{-}}$ which decays to the ground state 6^{+} level with a γ energy of 608 keV. As well the line at 227 keV could be seen as a $2^{-}_{K=1^{-}} \rightarrow 3^{-}_{K=0^{-}}$ transition. We should underline that this is only a tentative guess on the basis of weak statistics. New experimental data are needed to provide a clear signature of the existence of these negative parity-excited states.
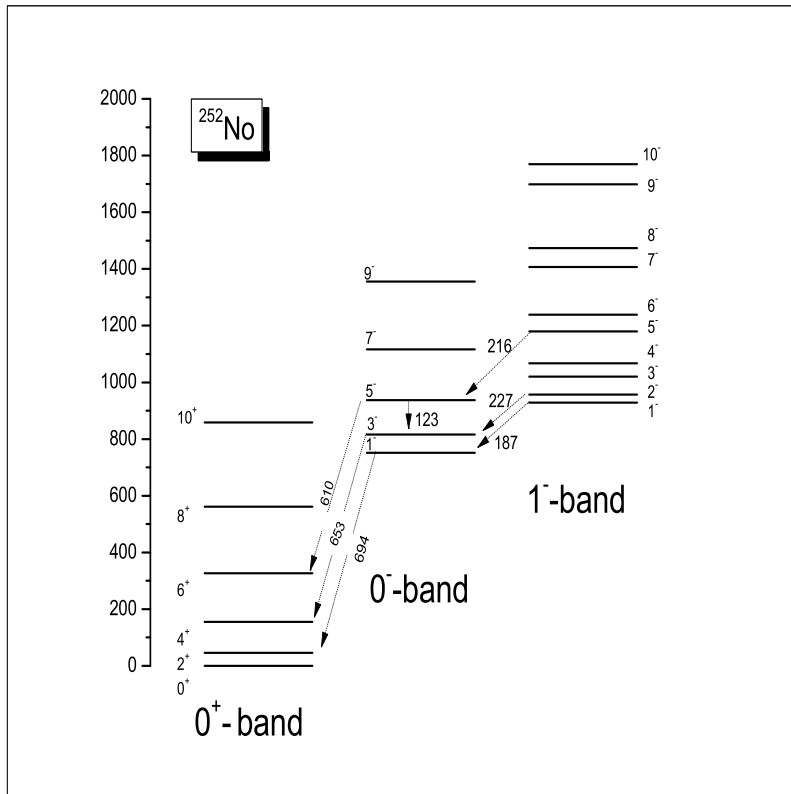

Figure 4.16: Calculated level scheme of ^{252}No from T.M.Shneidmann [53].

4.4   Alpha Decay Spectroscopy

The observed α decay of the implanted recoils can also be used to study decay properties of ^{252}No.
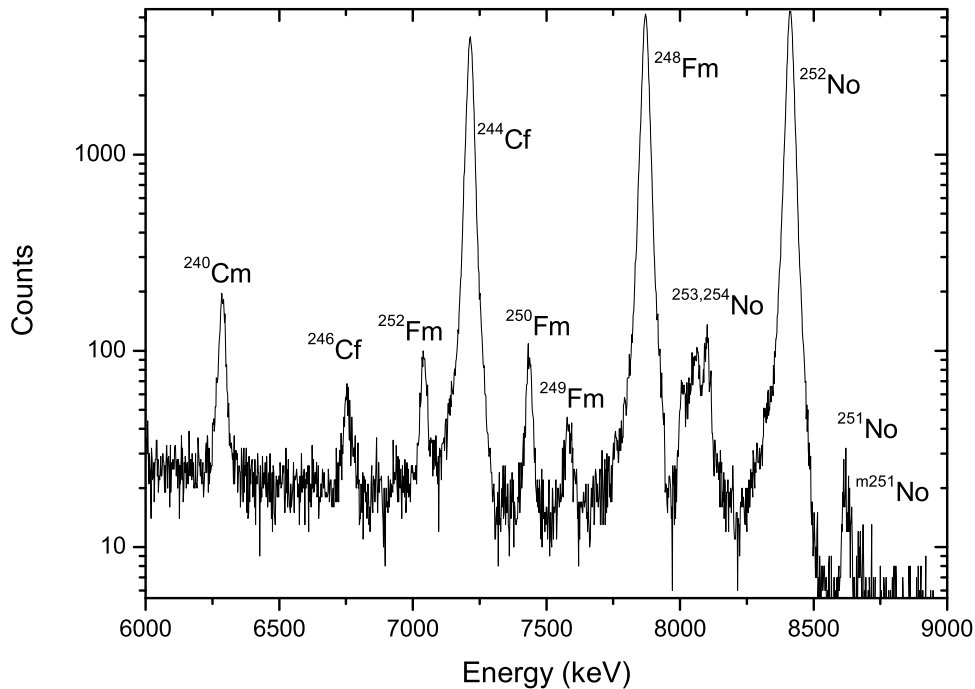
Figure 4.17: Total alpha decay spectrum in the silicon detector of the focal plane of SHIP in logarithmic scale, for details see the text.

The α particle energy spectrum is shown in Fig. 4.17, for a total of 10^5 α decays detected. The ground state of ^{252}No decays by α emission into the ground state of ^{248}Fm. Only about 10-20% of the ground state are expected to populate the first excited 2^+ level in ^{248}Fm at ≈ 44 keV. Since this transition is strongly converted, the energies of the α particle and the subsequent conversion electron are summed up in the silicon detector and only one α peak is visible. In the spectrum are also present ^{251,253,254}No. ^{251,253}No are produced by 1n and 3n evaporation, respectively. Moreover, a small impurity of ^{207}Pb may induce the production of ^{253}No as 2n evaporation channel. Small contaminations of ^{208}Pb in the target induce, the production of ^{254}No as 2n evaporation channel and its decay products ^{250}Fm and

^{246}Cf . Moreover, the peak at 7.034 MeV is attributed to ^{252}Fm produced via the EC decay of ^{252}No $\underline{EC}$ ^{252}Md $\underline{EC}$ ^{252}Fm. The production of ^{252}Fm via ^{256}No decay, we exclude with a high probability due to the negligible production cross section. From our experiment, we deduce the branching ratio for the different decay modes of ^{252}No as b_α=70 %, b_{sf} = 29 %,b_{EC,β^+}=0.8%.
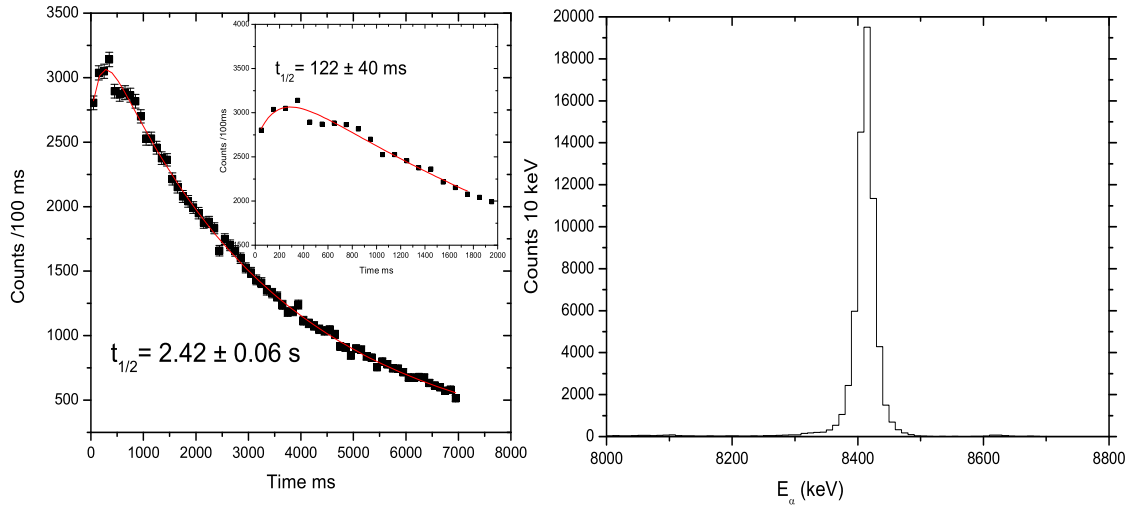
Figure 4.18: The lifetime curve for ^{252}No extracted by gating the ER-α and ER-sf correlated particle with a search time of 7s. The embedded figure shows the growing activity around 100 ms due to the decay of the isomeric state via γ to the ground state. ER-α correlated alpha particle energy spectrum of ^{252}No. The half-life is $T_{1/2} = (2.42\pm0.06)$ s.

The time distribution of ^{252}No is obtained from the sum distribution of ER-α and ER-sf correlations. The searching time for the ER in correlation with α and sf was 7 s, and by gating the α line between 8.3 MeV and 8.5 MeV. The corresponding time distribution is shown in Fig. 4.18. A half-life of (2.42±0.06) s was measured. This value is in good agreement with A. Ghiorso et al. [54], Oganessian et al. [55]. The inset in Fig. 4.18 shows an expansion of the curve in the range between 0 and 2s, which shows a growing activity in correspondence of the half life of the decay of ^{252m}No. The curve is fitted by the function

$$y = A1 * exp(-x/t1) + A2 * exp(-x/t2) + A3 * exp(-x/t1) + y0$$

where t2(t1) is the lifetime of the isomer(α decay of the ground state). Lifetimes of 3.44 s(ground state) and 177 ms were found for the isomer, which correspond to half-lives of $T_{1/2} = (2.41\pm0.04)$ s and $T_{1/2} = (122\pm40)$ ms, respectively.

Another information about the decay path of ^{252}No came from the presence of K-Xrays of ^{244}Cm in the spectrum in Fig. 4.19. The peaks at 104 and 108 keV correspond to the $K_{\alpha1,2}$ X-rays of ^{244}Cm as well as the lines between 122 and 127 keV (not clearly separated) can be attributed to K_{β} X-rays. Moreover, the clear lines at 217 and 889 keV have similar energy as the known γ rays characteristic for the de-excitation of ^{244}Cm populated via electron capture decay of ^{244}Bk [34].
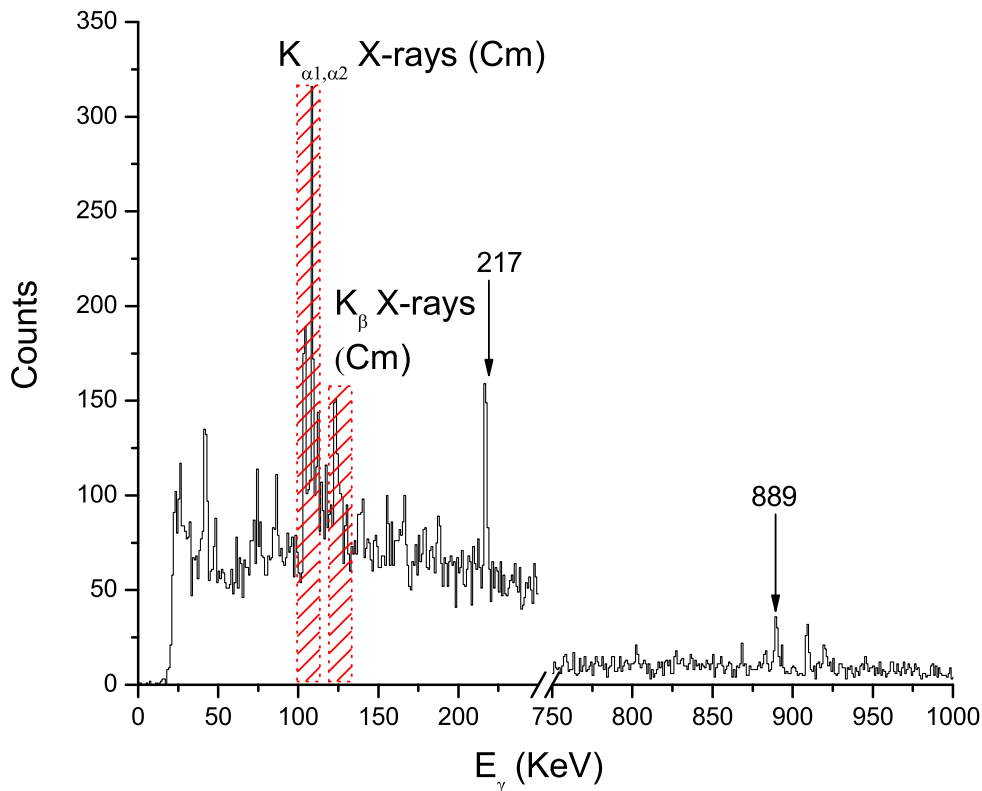
Figure 4.19: Gamma spectrum of ^{252}No in prompt coincidences with CE.

Finally, we can conclude that ^{244}Cf decays not only via α but also via EC decay ^{252}No $\xrightarrow{\alpha}$ ^{248}Fm $\xrightarrow{\alpha}$ ^{244}Cf $\xrightarrow{EC}$ ^{244}Bk $\xrightarrow{EC}$ ^{244}Cm with a branching ratio of 2.37$\pm$0.03 %. Thus, the ^{244}Cf EC-branching ratio was deduced by comparing the intensities of the ^{244}Cf in the ER-α spectrum with the intensities of the gamma transitions at

218 and 889 keV in the ER-γ spectrum (assigned to Bk) assuming that all ^{244}Bk nuclei produced decay via EC to ^{244}Cm. Finally, we can give an upper limit for the b_{EC} for EC-branch of ^{244}Cf of 2.37 ± 0.03 %. This interpretation could not be supported by the direct measurement of the α decay of ^{244}Cm with a half-life of 18 years. Therefore, this value must be taken as tentative on the basis of the gamma lines found in delayed coincidences.

Chapter 5

Experimental Results: ^{254}No

The discovery of a K isomer in ^{254}No has to be attributed to Ghiorso [56] who reported the presence of a 0.28 ± 0.04 s isomeric state in ^{254}No in 1973. Only in recent years, very exhaustive investigations were carried out at Jyväskylä and two isomeric states with half-lives of 266±2 ms and 184± 3 μs, respectively, were found [3].

Beam material	^{48}Ca^{+10}
Beam energy	219 [MeV]
Excitation energy	22.5 [MeV]
Average beam intensity	43 μA
Time beam on the target	$200 * 10^3 s$
Target material	^{208}Pb
Target thickness	C($38\mu g/cm^2$) PbS(438 $\mu g/cm^2$) C(10 $\mu g/cm^2$)
Number of recoil detected	$2 \cdot 10^5$

Table 5.1: Beam and target parameters related to the experiment on the production of ^{254}No.

At SHIP, we performed the same reaction, ^{48}Ca $+^{208}$Pb, with higher beam intensity and efficiency in order to get more information about the decay path of the isomeric states. Details about beam and target parameters are summarized in table 5.1.

The time distributions between implanted ^{254}No nuclei and delayed gammas in prompt coincidence with electrons give two components with different life times (Fig. 5.1 a,b). In Fig. 5.1 a) a time difference $\Delta T(ER - \gamma(e^-)) < 2s$ was set and a

half-life of 275 ± 7 ms was obtained.
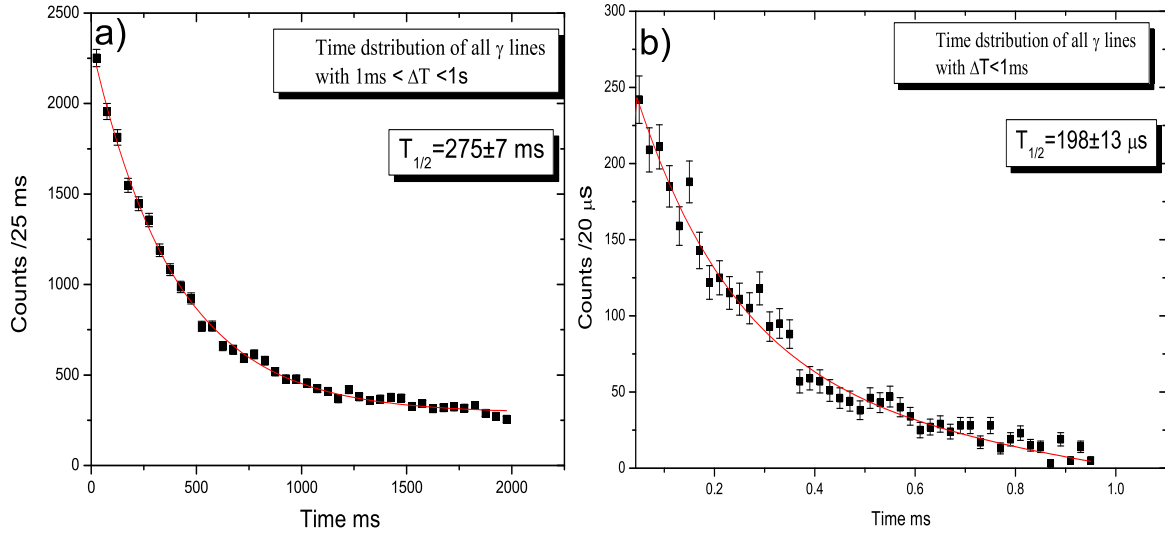
Figure 5.1: Time distribution of γ transitions in prompt coincidences with electrons following recoil implantation a) for the long-lived isomer and in b) for the short-lived isomer.

In Fig. 5.1 b) the time distribution between delayed gammas and ^{254}No recoils within 1 ms after the implantation is shown. A half-life of 198 ± 13 μs was found. Both results are in good agreement with the Jyväskylä data for the two isomeric states in ^{254}No.

The electron spectra in prompt coincidence with γ transitions from the short and long-lived isomer are shown in the Fig. 5.2. Both isomers have different electron energy distributions characteristic for their decay path.

5.1   Long lived isomer in ^{254}No

The γ spectrum resulting from the de-excitation of the long-living isomer followed by prompt electrons is shown in Fig. 5.3. The correlation time between ER and γ was set to 2s. The energies of the gamma rays and the mean energies of coincident electrons are listed in table 5.2.
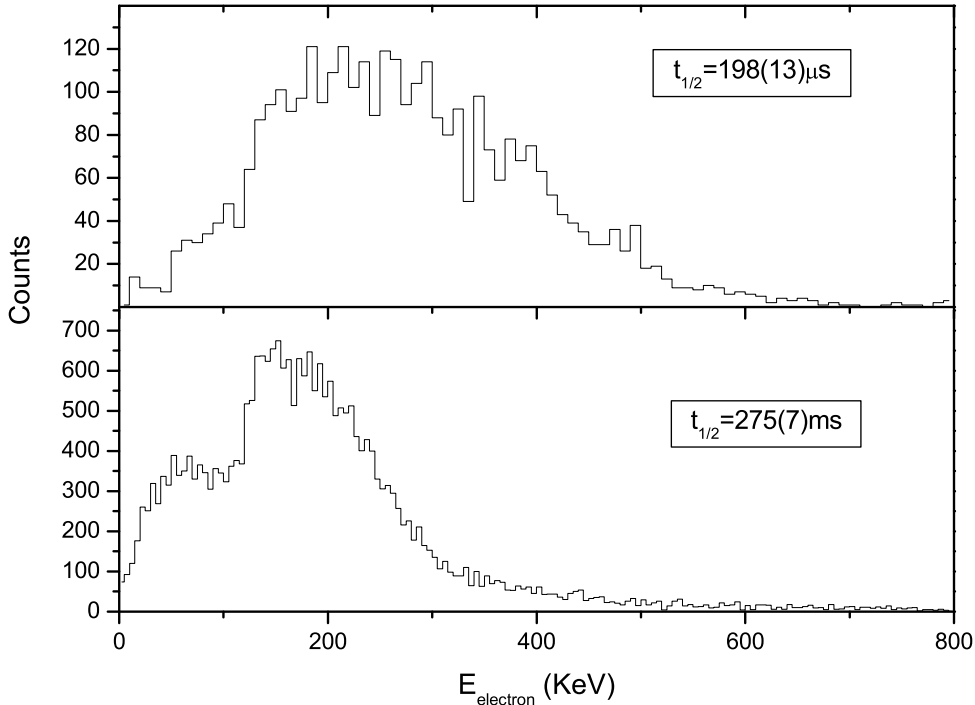
Figure 5.2: Energy distribution of electrons in prompt coincidence with gamma rays for the short (upper panel) and long-lived isomer (lower panel).

In the following, the results on the long-lived ^{254}No isomer obtained by R.-D. Herzberg [3] are summarized: All the high energy lines (embedded in Fig. 5.3) were also observed in an in-beam experiment [57]. Therefore, they concluded that these transitions do not originate from the isomeric level, but from some intermediate band which decays to the ground state band.

The level scheme and the transitions (black arrows) suggested by R.-D. Herzberg including modifications from this works (red arrows) are shown in Fig. 5.4.

Spin and parity of the band head of the intermediate band were assigned as $K^{\pi} = 3^+$. The parity was deduced from the M1 character of the 944 and 842 keV transitions and the positive parity of the ground state band. As well, the spin and parity of the long-lived isomer were assigned by Herzberg et al. [3] to be $K^{\pi} = 8^-$. This assignment was supported by a comparison to the decay patterns of neighbouring nuclei in this mass region. To summarize, it was found that the isomer decays to an intermediate band via a 53 keV E1 transition. This band de-excites to

E_γ	N_γ	E_{ele}/keV	comments
$53,0 \pm 1.2$	1096	171 ± 1	
58.9 ± 3.6	82		
70.0 ± 0.6	71		
81.8 ± 1.0	62	150 ± 2	
87.1 ± 0.4	54		
98.0 ± 2.9	81		
101.9 ± 1.3	82	150 ± 9	
104.2 ± 0.9	41		
115.1 ± 0.8	552	138 ± 8	$K_{\alpha 1}$ (Fm)
118.5 ± 3.9	399		$K_{\alpha 2}$ (Md)
121.0 ± 1.2	428	139 ± 4	$K_{\alpha 2}$ X-rays (No) and $K_{\alpha 1}$ (Fm)
124.1 ± 1.6	184	117 ± 14	$K_{\alpha 1}$ (Md)
127.4 ± 1.5	207	147 ± 6.7	$K_{\alpha 1}$ X-rays (No)
152.1 ± 1.8	174	129 ± 6	
159.1 ± 3.2	135	149 ± 10	
649.4 ± 1.4	27		
694.2 ± 1.4	32	156 ± 9	
778.1 ± 2.2	45	171 ± 5	
841.5 ± 2.5	233	228 ± 5	
856.4 ± 2.5	21		
887.8 ± 2.1	63	208 ± 9	
899.7 ± 3.9	26		
943.7 ± 2.2	770	181 ± 2	
962.1 ± 3.1	17		

Table 5.2: List of transition energies attributed to the decay of the long-lived isomer in ^{254}No.
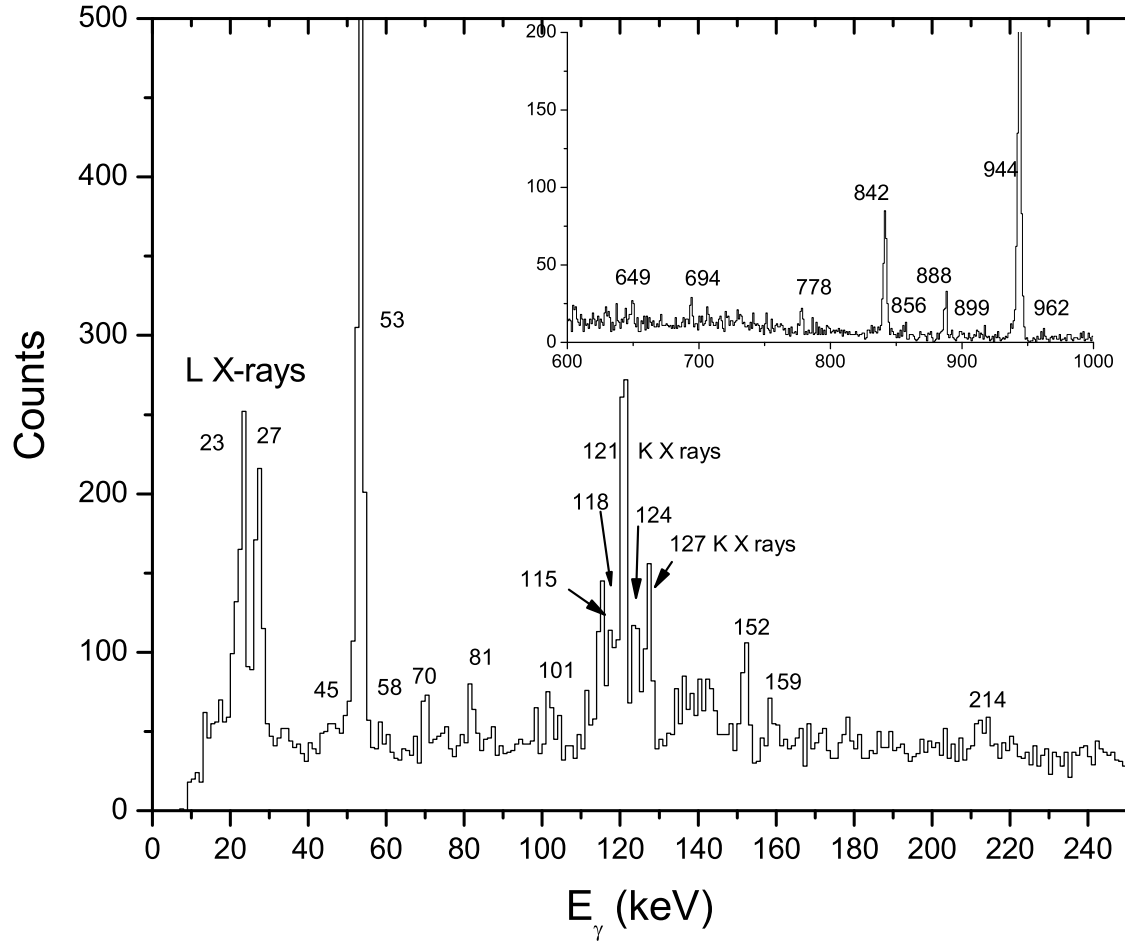
Figure 5.3: Gamma spectra in delayed coincidence $1ms < \Delta T < 2s$ with ER(^{254}No)in prompt coincidence with electrons detected in the stop detector. In the embedded figure expansion of the gamma spectra from 600 to 1000 keV is shown.

the ground state rotational band via 944, 888, and 842 keV transitions.

In our work, we could confirm the level scheme of R.-D. Herzberg. Moreover, due to the higher number of decays, four additional weak transitions were identified. The lines at 856, 778, 694 and 649, keV have not been reported previously.

The line at 856 keV has been assigned to the $6^+ \rightarrow 6^+$ transition between the

Figure 5.4: Level scheme of ^{254}No as proposed by R.-D. Herzberg matched with our experimental results (red arrows).

intermediate and ground state band, since the energy difference between the two levels is (1161-305) keV = 856 keV.

The 778 keV line is tentatively assigned to the direct decay of the isomeric 8$^-$

level into the 8^+ level of the ground state band, with a calculated branching ratio of $\approx 4\%$. The energy of 778 keV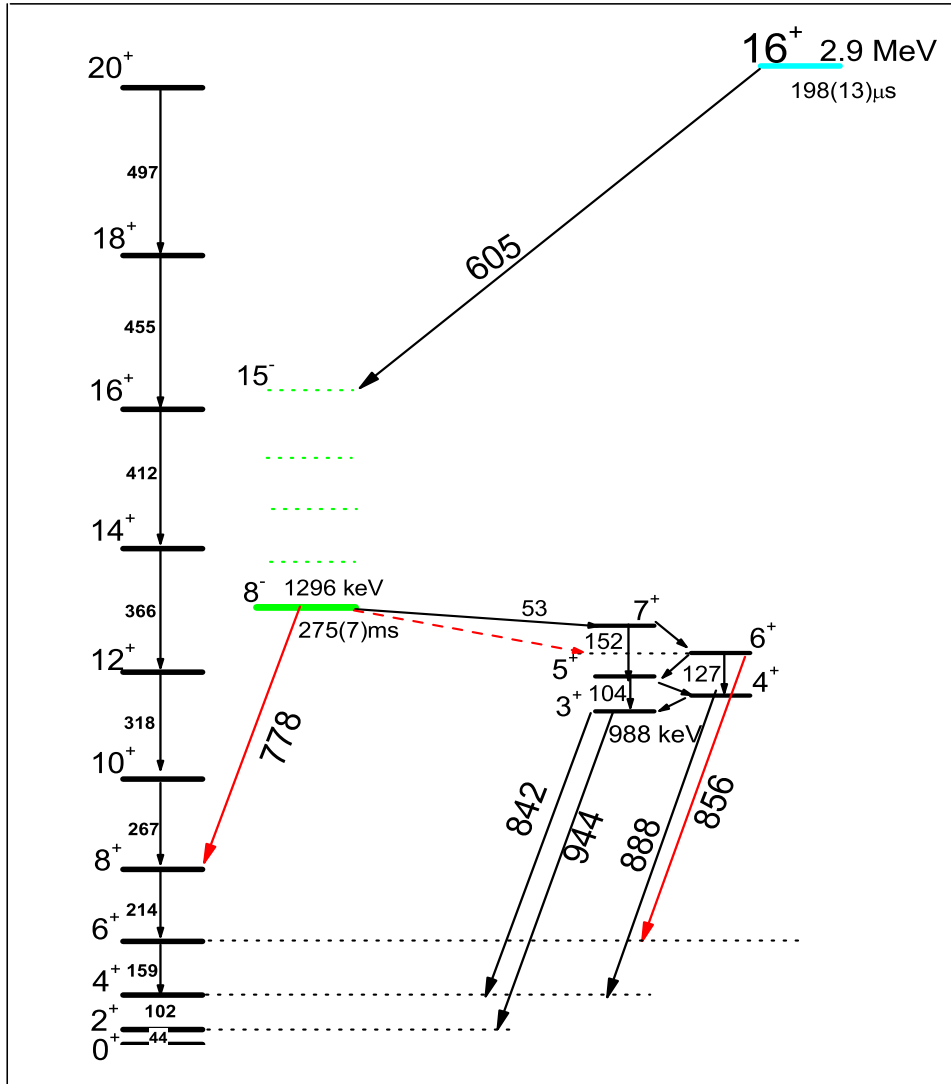 corresponds within 1 keV to the energy difference between the 8^- (1296 keV) and 8^+ (519 keV) level. A further supporting argument is, that the intensities of the 778 keV and the 214 keV lines are in agreement, taking into account detection efficiencies and conversion coefficients.

The two new transitions assigned in this work are represented by the red arrows in the level scheme in Fig. 5.4.

The weak lines at 115, 694, and 649 keV could not be attributed to the decays within the level scheme suggested above. The possible explanations are given in the following. The weak line at E=115 keV is close to the $K_{\alpha 2}$ energy of Fermium. The presence of Fermium K X-rays is supported by the intensity ratio of the lines at E=121 keV and E=127 keV. While the energies fit to those of the $K_{\alpha 2}$ (120.95 keV) and $K_{\alpha 1}$ (127.36 keV) of Nobelium, their intensity ratio is in disagreement with I($K_{\alpha 1}$(No))/I($K_{\alpha 2}$(No))=1.5. So the line at 121 keV may be interpreted as a not resolved doublet of $K_{\alpha 2}$ (No) and $K_{\alpha 1}$ (Fm)(E=121.06 keV). The fermium K X-rays are apparently randomly correlated with ^{254}No evaporation residue. This interpretation is also supported by CE-$\gamma - \gamma$ coincidences (without correlation to ^{254}No-ER). Here, weak coincidences between E=115, 121 keV X-rays and γ-rays of E=649 keV and E=694 keV were observed. Such γ-transitions have been observed in β^--decay studies of ^{254}Es and were attributed to the decay of a 2^+ level in ^{254}Fm at E^*=693.79 keV into the first 2^+ level and into the ground state, respectively. So we assume that this level is also populated by EC-decay of ^{254}Md via the decay path ^{254}No $\underrightarrow{EC}$ ^{254}Md $\underrightarrow{EC}$ ^{254}Fm. In Fig. 5.3 two more weak lines at E=118, 124 keV are indicated, which fit to the $K_{\alpha 2}$, $K_{\alpha 1}$ X-ray energies of Mendelevium of E($K_{\alpha 2}$) = 118.09 keV and E($K_{\alpha 1}$)=124.17 keV. However, no $\gamma - \gamma$ coincidences of these lines with γ transitions have been observed in our experiment.

5.2   Short lived isomer in ^{254}No

The existence of a short-lived isomer in ^{254}No was already reported by R.-D. Herzberg et al. [3]. It was expected by Herzberg et al. [60] and Tandel et al. [58], that the isomer decays to the rotational band based on the $K^\pi = 8^-$ state of the 275 ms isomer at 1293 keV, including a 605 keV line. The lower limit for the excitation energy of the isomeric level was established on the basis of the electron distributions.

Electron energies were found up to 610 keV. Therefore, the excitation energy of

the short-lived isomer was determined to be > 2420 keV. Spin and parity 16^+ has been assigned to this level, in analogy to the case of ^{178}Hf.
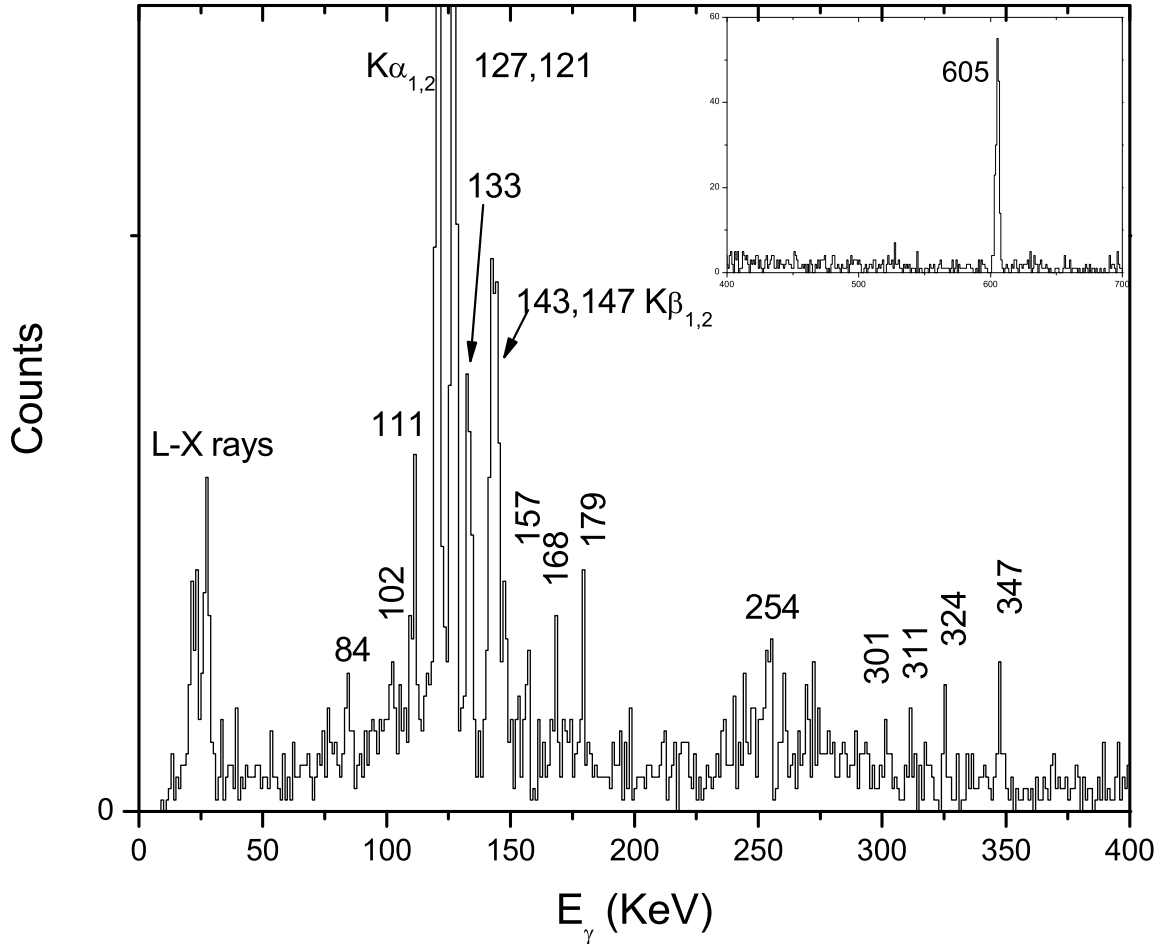
Figure 5.5: Gamma ray spectrum of the decay path of the short-lived isomer. The embedded figure shows an expansion of the gamma spectrum from 400 to 700 keV.

This result was supported by our data. Moreover, we found a rotational band on top of the long-lived 8^- isomer, supporting the suggested decay path of R.-D. Herzberg [59].

The γ spectrum resulting from ER-$\gamma(e^-)$ coincidences within 1ms after the implantation of the evaporation residue is shown in Fig. 5.5 and the respective γ energies in table 5.3.

E_γ	N_γ	comments
22.4 ± 0.3	112	$\sum L_\beta$ X-rays
27.7 ± 0.2	87	$\sum L_\gamma$ X-rays
111.4 ± 0.5	63	
120.74 ± 0.01	273	$K_{\alpha 2}$ X-rays
127.2 ± 0.02	341	$K_{\alpha 1}$ X-rays
133.27 ± 0.12	128	
143.3 ± 1.3	194	$K_{\beta 1}$ X-rays
146.3 ± 10	63	$K_{\beta 2}$ X-rays
157 ± 4	49	
168.1 ± 0.1	30	
179.4 ± 0.07	31	
254.1 ± 0.4	7	
301.3 ± 0.2	8	
311.4 ± 0.2	9	
325 ± 0.2	12	
347 ± 0.2	14	
605.4 ± 0.08	139	

Table 5.3: List of transition energies observed for the decay of the short isomer to the rotational band via an intermediate band to the ground state of ^{254}No.

The γ line at 605 keV is attributed to the decay of the isomeric 16^+ state to the 15^- state of the rotational band built on top of the 8^- long-lived isomer. The transition at 347 keV was attributed to the decay from the $15^- \rightarrow 13^-$ state. As a tool for interpreting the data, we used the rotational model to calculate the level energies according to $E_I = E_0 + AI(I + 1)$ where A is $\hbar^2/2\Im$. The rotational parameter calculated for the band ($\hbar^2/2\Im$) is 5.966 keV which is very close to the 5.81 observed for the 3^+ band. Therefore, the prominent transitions at 111, 133, 157, 168, and 179 keV are assigned to M1 transitions within the rotational band built on the top of the long-lived isomer. The 311, 325, and 347 keV lines are assigned to E2 transition. This assignment is also supported by the $\gamma - \gamma$ coincidence spectrum (Fig. 5.7) gated on the 133 keV line. In the spectrum, prompt coincidences between the 133 and 111, 168, and 605 keV lines are visible. In the spectrum gated on 605 keV line, we observed coincidences with K X rays and L X rays of No. The suggested level scheme is shown in Fig. 5.6.
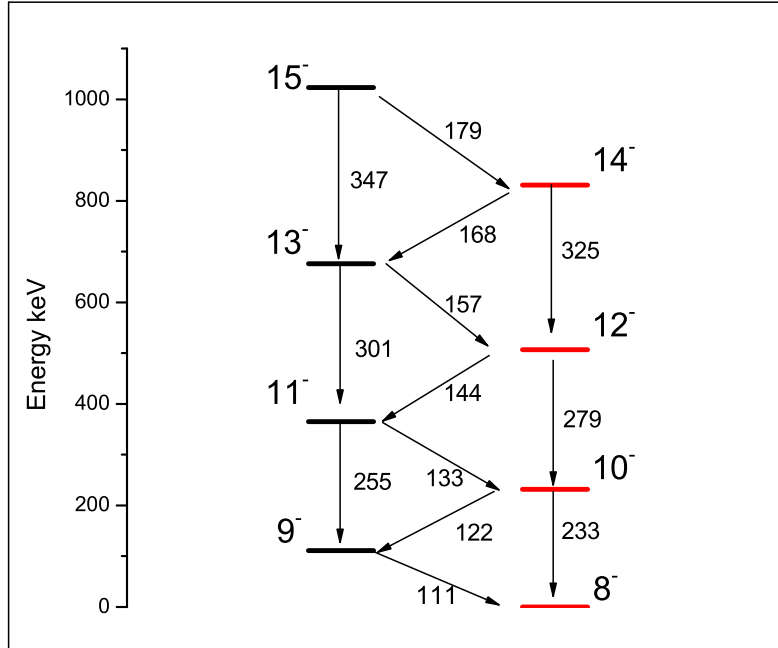
Figure 5.6: Proposed level scheme for the short-lived isomer which decays to the rotational band build on the top of the long living isomeric state.

The observed K X rays are mainly attributed to the conversion of the 179 and 168 keV transitions which are the only strong transitions above the K binding energy of 159 keV. On the basis of this level scheme the number of K X rays expected according to $N_x = \alpha_{(E2/M1)} \frac{N_\gamma}{\epsilon_\gamma} \cdot \epsilon_x$ is 611 compared with 620 counts observed. Since $I(347keV) + I(168keV) = I(301keV) + I_\gamma(157keV)$ we expect 28 counts from the 301 keV line which is still in agreement with the 19 events observed.

Several points are left unexplained. The obtained intensity of the 133 keV M1 transition is much higher than the intensity of the 605 keV line assuming E1 multipolarity. A possible explanation could be the existence of another $K^\pi = 8^-$ band at higher energy with moment of inertia similar to the band built on the long-lived isomer. This is for example the case for ^{178}Hf. In ^{178}Hf the 16^+ isomer at 2446 keV decays to the 12^- state of the $K_1^\pi = 8^-$ band located at 1147 keV via a M4 transition and to the 13^- state via an E3 transition. Moreover, in this isotope, another band with the band head $K_2^\pi = 8^-$ at 1479 keV exists which is populated by the

de-excitation of the band built on $K^\pi = 8^-$. The interband transitions of these two bands have very similar energies because of their similar moment of inertia ($\hbar^2/2\Im$ 12.05 keV and 12.10 keV, respectively). Assuming a similar situation also in the case of ^{254}No, it would be very difficult to assign each transition to the proper band. Precise information on the $K^\pi = 8^-$ band could only be obtained by $\gamma - \gamma$ angular correlation measurements carried out only with much higher statistics.
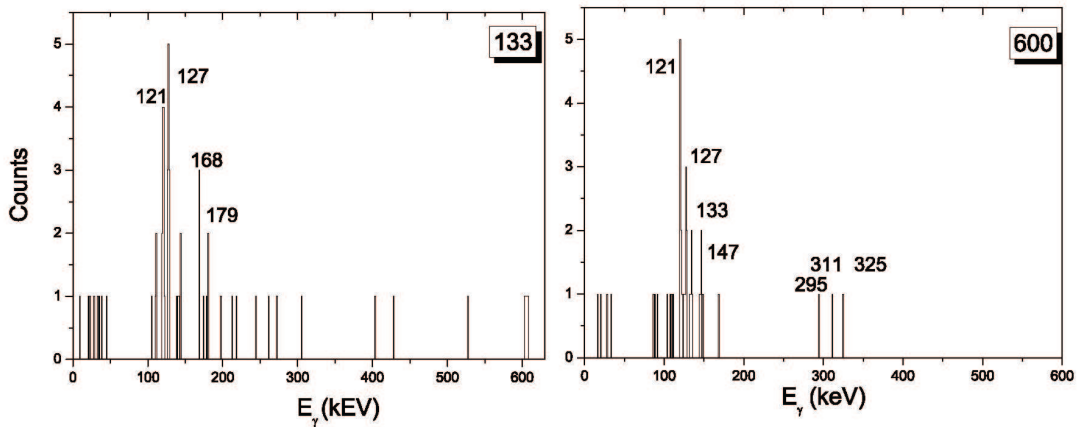

Figure 5.7: Gamma-gamma coincidences with gate on 133 keV and 605 keV lines.

From the observed decay pattern, the most likely spin and parity for the 2899 keV isomer is 16^+ since a lower spin of 14^+ as suggested by Tandel et al. [58] would have certainly caused a stronger feeding into levels with I<14. E.g. if E($14^+\rightarrow 15^-$)=605 keV we should have observed E($14^+\rightarrow 14^-$)=605+179 = 784 keV or E($14^+\rightarrow 13^-$)=605+167+179= 951 keV, not all present in the spectrum. Finally, since no two quasi-particle state with such high K is expected at this energy, we can conclude that this state is a 4 quasi particle state coupling a two quasi-proton state and a two quasi-neutron state.

5.3 Conclusion for the isomers in ^{254}No

The limited spectroscopic information leads to ambiguities in the spin and parity assignments. Many low lying high spin isomeric states have been found in the mass region of A=170-190, including the well known series of isomers in even N=106 isotones and even Hf isotopes. Many of these states have been interpreted as be-

ing $K^\pi = 8^-$ two-quasi particle states with the Nilsson configuration $7/2^+[514]\nu$, $9/2^+[624]\nu$ or $7/2^+[404]\pi$, $9/2^-[514]\pi$. There are single particle levels near the Fermi surface for both neutrons near N=150 and protons near Z=100 such that coupling of two neutron or two proton orbitals can give rise to high spin two quasi-particle states. According to the single-particle Nilsson level scheme, the 149st, the 151st, and the 153st neutron occupy $7/2^+[624]$, $9/2^-[734]$, $7/2^+[613]$ levels respectively. This order of single particle states is supported by the ground state assignments of nuclides with the mentioned neutron numbers, and in particular, by the study of single particle states in odd mass Cm isotopes. Possible two neutron configurations for isomeric states ion ^{250}Fm and in ^{254}No would thus be $K = 8^-$ two quasi particle states with the Nilsson configurations $7/2^+[624]$, $9/2^-[734]$ and $9/2^-[734]$, $7/2^+[613]$.

In the case of protons, the relevant 99th, 101st, and 103rd protons are in the orbitals $7/2^+[633]$, $7/2^-[514]$, and $9/2^+[624]$ in ^{254}No [2].

According to Ghiorso's interpretation of the isomeric state found in ^{254}No also Xu et al interpret it as $\nu_{7/2}^+[613] \otimes \nu_{9/2}^-[734]$ and $\pi_{7/2}^-[514] \otimes \pi_{9/2}^+[624]$ with excitation energy 1.12 MeV and 1.48 MeV, respectively. Moreover, low lying $\nu_{7/2}^+[613] \otimes \nu_{9/2}^-[734]$ states exist systematically in the N=152 isotones.

The interpretation of the short living isomeric state is still under investigation but, as already mentioned, we compared this isotope with ^{178}Hf and assign 16^+ as spin and parity as product of the two-proton and two-neutron configuration. The configuration suggested for the ^{178}Hf was a four quasiparticle state $\pi_{7/2}^-[514] \otimes \pi_{9/2}^+[624] \times \nu_{7/2}^+[624] \otimes \nu_{9/2}^-[734]$ calculated to lie at 2.75 MeV. The occurrence of this isomer in ^{254}No is due to the violation of the K selection rule like in the case of ^{252}No. Retardation due to K forbidness is given by $f_\nu = T_{1/2}^{exp}/T_{1/2}^{WU}$, where $T_{1/2}^{exp}$ and $T_{1/2}^{WU}$.

The γ- line of E=53 keV line assigned to the decay of the $K^\pi=8^-$ has $f_\nu = 804$, typical for the most retarded transitions in the Hf region.

Chapter 6

Conclusions

In this work, K-isomeric states in ^{260}Sg, ^{256}Rf, and ^{252,254}No were investigated.

Two isomeric states at low excitation energies are predicted in ^{260}Sg. At 0.97 MeV, a two quasi-proton state with the configuration $\{\pi\,[624]_{9/2+} \otimes \pi\,[512]_{5/2+}\}$ is expected and at 1.05 MeV, a two quasi-neutron state with the configuration $\{\nu\,[613]_{7/2+} \otimes \nu\,[725]_{11/2-}\}$. A third isomer should be located at 1.20 MeV with the configuration $\{\nu\,[725]_{11/2-} \otimes \nu\,[615]_{9/2+}\}$. Due to the similarity with ^{270m}Ds, ^{260m}Sg should decay notably via α emission to the ground state or an isomeric state of ^{256}Rf.

However, we did not observe a statistically significant component with different life time or α energy than that of the ^{260}Sg ground state with a lifetime ¿10 μs. From our data, we deduced an upper cross section limit of 10 pb for populating the isomeric state.

We discovered a new K isomer in ^{252}No with a half life of 100 ms. Spin and parity of this isomeric state are assigned to $K^\pi = 8^-$. It decays to the ground state band by γ rays via an intermediate band with an assigned band head $K^\pi = 2^-$. The isomer was interpreted as a two quasi-neutron configuration $7/2^+[624] \otimes 9/2^-[734]$ at 1254 keV. The theoretically predicted excitation energy 1070 keV [38] for this K isomer is in good agreement with our value.

Moreover, the properties of the isomeric states in ^{254}No were reinvestigated and new improved results resulted from our experiment. The 0.28 s isomer was confirmed at an excitation energy of 1296 keV. Spin and parity 8^- ([60]) are in line with our results on the basis of the γ decay data. A second isomer with an excitation energy of ~ 2.8 MeV and half life of 184 μs was remeasured. New γ transitions assigned to the decay of the short lived isomer could be identified in this work, allowing us to

draw conclusions on a more complete level scheme.

A summary, of the presently known K isomers in the region N=162, Z=108 and N=152, Z=100 are given in the table 6.1.

Nucleus	$t_{1/2}^m$	$t_{1/2}^g$	K_ν^π	E^* [MeV]	ref.
^{260}Ds	6.0 ms	1.0 ms	$9^-, 10^-$	1.3 MeV	[36]
^{266}Hs	0.35 ms	2.3 ms	$9^-, 10^-$	0.92 MeV	[36]
^{254}No	0.28 ms & 170 μs	51 s	$8^-, 16^+$	1.29 MeV, 2.5 MeV	[60] p.w.
^{252}No	100 ms	2.3 s	8^-	1.25 MeV	p.w.
^{250}No	43 μs	3.7 μs	6^+	1.05 MeV	[61]
^{256}Fm	70 ns	172 min	7^-	1.4 MeV	[62]
^{250}Fm	1.8 s	30 min	$(7^-, 9^-)$	keV	[56]
^{246}Cm	34 ms	4730 Y	8^-	1.17 MeV	
^{244}Cm	34 ms	18.1 Y	6^+	keV	[63]

Table 6.1: Summary of low lying K isomers for even even nuclei in the region N=162, Z=108 and N=152, Z=100.

To summarize, with this work, we sustain the existence of K isomerism in this region confirming the presence of high K deformed configurations in the vicinity of the Fermi surface. Moreover the investigation of nobelium isotopes delivered data in a region close to the domain of superheavy nuclei, where our knowledge of single-particle spectra and of pairing correlations is particularly limited.

Especially for superheavy nuclei with sufficiently short life times, the isomeric states may be longer lived than the corresponding ground state like it is the case in ^{270}Ds. Thus, isomeric states could not only be valuable objects for the study of nuclear structure at very high Z but could turn out to be of practical importance for the further exploration of the limits of stability at the upper end of the periodic table.

Bibliography

[1] F.R. Xu *et al.* Phys. Rev. Lett. **92**, 25 (2004)

[2] A. Ghiorso *et al.* Phys. Rev. C **17**, 5 (1973)

[3] R.-D. Herzberg *et al.* Nature **442**, 896-899 (2006)

[4] M. Goeppert-Mayer and J.H.D. Jensen. *Elementary theory of Nulcear Shell Structure.* New York. John Wiley and Sons (1955)

[5] S.G. Nilsson *et al. Binding States of Individual Nucleons in Strongly Deformed Nuclei.* Dan. Mat. -Fys. Medd. **24**, 16 (1955)

[6] V.M. Strutinsky *et al.* Nucl. Phys. A **95**, 420 (1967); V.M. Strutinsky *et al.* Nucl. Phys. A **122** (1968)

[7] R.-D. Herzberg *et al.* Phys. Rev. C **65**, 014303 (2001)

[8] URL: *http://wwwnsg.nuclear.lu.se/basics/background.asp*

[9] P. Ring and P. Schuck. *The Nuclear Many-Body problem.* Srping- Verlag, New York (1980)

[10] J. Bardeen *et al.* Phys. Rev. **108**, 1175 (1957)
A. Bohr *et al.* Phys. Rev. **110**, 936 (1958)

[11] W. Loveland, D.J.Morrisey and G.Seaborg. *Modern Nuclear Chemistry*, Wiley and Sons (2005)
G.T. Seaborg and W. D. Loveland, *The Elements Beyound Uranium.* J. Wiley & Sons, INNC., New-York, Chichester, Brisbane, Toronto, Singapore, (1990)

[12] J.O. Rasmussen et al. Phys. Rev. **113**, 1593 (1958)

[13] D.N. Poenaru *et al.* J. Phys. **41**, 589-590 (1980)

[14] E. Rurarz. Acta Physica Polonica B **14**, 917 (1983)

[15] A. Popeko, private communication.

[16] G. Alaga *et al.* Mat. Fys. Medd. **29**, 9 (1955)

[17] R.Geller *et al.* Rev. Sci. Instrum. **63**, 2795 (1992)

[18] B. Lommel *et al.* Nucl. Instr. Meth. A **480**, 16 (2002).

[19] R. Mann *et al.* Scientific Report GSI (2004)

[20] K. Shima *et al.* Nucl. Instrum. and Methods **200** 605-698 (1982)

[21] G. Münzenberg *et al.* Nucl. Instrum. Methods **161**, 65 (1979)

[22] M. Mazzocco *et al.* Eur. Phys. J. A (in press)

[23] F.P. Heßberger *et al.* Eur. Phys. J. A **22**, 417 (2004)

[24] T. Kibédi *et al.* BRICC Conversion Coecient Calculator, URL: *http://wwwrsphysse.anu.edu.au/ txk103/bricc/* (2005)

[25] S. Saro *et al.* Nucl. Instr. and Meth. in Phys. Res. A **381**, 520-526 (1996)

[26] S. Hofmann *et al.* Paper submitter to EPJ 17 April 2007

[27] J. Hoffmann, W. Ott. Development of new readout processor SAM3, GSI scientific report 2002.

    J. Hoffmann, N. Kurz, and W. Ott, Development of ADC multiplexer for SHIP, scientific report 2004.

[28] G. Münzenberg *et al.* Z. Phys. A -Atoms and Nuclei **322**, 227-235 (1985)

[29] B. Streicher. *Synthesis and spectroscopic properties of transfermium isotopes with Z = 105, 106 and 107*, Thesis work.

[30] W.D. Myers and W.J.Światecki. Nuc. Phys. A **601**, 141-167 (1996)

[31] J.F. Ziegler and J.P. Biersack, SRIM-2003, *Stopping and Range of Ions in Matter* URL: *http://www.srim.org*, (2003)

[32] F.P. Heßberger *et al.* Z. Phys. A **359**, 415-425 (1997)

[33] K.-H. Schmidt *et al.* Eur. Phys. J. A **8**, 141-145 (2000)

[34] R.B. Firestone *et al. Table of Isotopes.* John Wiley & Sons, Inc. New York. Chicester, Brisbane, Toronto, Singapore (1996)

[35] A. Sobiczewski *et al.* Phys. Rev. C **63**, 034306 (2001)

[36] S. Hofmann *et al.* Eur. Phys. J. A **10**, 5-10 (2001)

[37] S. Cwiok and S.Hofmann. Nucl. Phys. A **573**, 356-394 (1994)

[38] J.-P. Delaroche *et al.* Nucl. Phys. A B**771**, 103-168 (2006)

[39] R. Bass. Phys. Rev. Lett. **39**, 5 (1977)

[40] S. Antalic *et al*, in preparation (2007)

[41] A.-P. Leppänen *et al.* Eur. Phys. Jour.

[42] A. Bohr and B.R. Mottelson. K. Dan. Vidensk. Selsk. Mat.- Fys. Medd. **27** No.16 (1953)

[43] A. Bohr and B.R. Mottelson. *Nuclear structure*, vol II, Benjamin, New York, (1975)

[44] W. Reisdorf. *et al.* Z. Phys. A **300**, 227 (1981)

[45] S.W. Yates *et al.* Phys. Rev. C, **12** num 3 (1975) 795

[46] V.G. Soloviev *et al.* Nucl. Phys. **59**, 145-158 (1964)

[47] A.L. Komov *et al.* Izv. Akad. Nauk SSSR Ser. Fiz. **35**, 1550 (1971) [Bull. Acad. Sci. USSR Phys. Ser. 35, 1413 (1971)]

[48] S.W. Yates *et al.* Phys. Rev. C, **12**, Num 2 (1975) 442

[49] L.I. Rusinov *et al.* Soviet Phys. Usp. **4**, 282 (1961)

[50] K.E.G. Löbner. Phys. Lett. B **26**, 6 (1968)

[51] V.G. Soloviev *et al.* Yad. Fiz. **54**, 1232-1238 (1991)

[52] T.M. Shneidman *et al.* Phys. Rev. C **74**, 034316 (2006)

[53] T.M. Shneidman, private communication.

[54] A. Ghiorso *et al.* Phys. Rev. Lett. **18**, 11 (1967)

[55] Yu.Ts. Oganesian *et al.* Phys. Rev. C **64**, 054606 (2001)

[56] A. Ghiorso *et al.* Phys. Rev. C **7**, 2032 (1973)

[57] S. Eeckhaudt *et al.* EPJ **488**, 471 (2005)

[58] S.K. Tandel *et al.* Phys. Rev. Letters **97**, 082502 (2006)

[59] R.-D. Herzberg *et al.* Proposal 15.3.2007. *Spectroscopy of ^{254}No -Above the Isomers*

[60] R-D Herzberg *et al.* Phys. Scr. 73-77 (2006)

[61] D. Peterson *et al.* Phys. Rev. C **74**, 014316 (2006)

[62] H.L. Hall *et al.* Phys.Rev.C **39**, 1866 (1989)

[63] Y.A. Akovali *et al.* Nucl. Data Sheet **99**, 197 (2003)

[64] H. Geiger and J.M. Nuttall. Philos. Mag. **22**, 613 (1911)

[65] P.M. Walker and G.F. Dracoulis. Nature **399**, 35 (1999) P.M. Walker. Acta polonica B**36**, 1055 (2005) P.M. Walker et al. Phys. Lett. B**408**, 42 (1997)

[66] P. Greenlees, private communication

Curriculum vitae

Personal data:

Name:	Barbara Sulignano
Date of birth:	17.09.1974
Place of birth:	Napoli (Italy)
Nationality:	Italian
Italian Address:	Viale Nuova Stazione 22
	I-80055 Portici (Na)
German Address:	Klappacher Strasse 67
	D-64285 Darmstadt

Education and Qualification:

School	1979 - 1984 Primary School, Portici (Na)
	1984 - 1987 Middle School "O.Comes", Portici (Na)
	1988 - 1993 Scientific Gymnasium "F.Silvestri", Portici (Na)
University	1993 - 2002 Faculty of Physics, University of Naples "Federico II"
Laurea degree	10.07.2002 from the University of Naples
PhD study	from 08.2003 to 07.2007 at the University of Mainz